

REVIEW OF RESEARCH

Content

ISSN NO:- 2249-894X

Impact Factor : 5.7631(UIF)

Sr. No	Title and Name of The Author (S)	Page No
1	Low Temperature Stearic Acid Sol-Gel Synthesis Of Nano Crystalline MgO R. N. Wankhade ^a , G. V. Korpe ^b , N. S. Bajaj ^c , V. S. Hingwe ^a , S. K. Omanwar ^a	1
2	Study Of Antibacterial Activity Of pure And Al Doped ZnO Nanocrystalson <i>Bacillus Thuringiensis Ncim2130</i> And <i>Pseudomonas Cf. Montellii 9</i> Cultures R. S. Shaikh ¹ , R. B. Mahewar. ² and L. S Ravangave ³	5
3	A Mini Review On Synthesis method For Ferrite Nanoparticles R.V. Kotalkar and L.V.Thakre	12
4	Dielectric Response Of Iron Exchanged Fly Ash Zeolite A A. N. Kalyankar	15
5	Photovoltaic And Structural Properties Of Pth-Co-Pani-Sio ₂ Copolymer Composite Systems S. R. Takpire, K.R. Nemade, S.A. Waghuley*	18
6	Surface Electrical Study Of Graphene Synthesized By Electrolysis Method S. S. Gore ^{1*} and S. K. Devade ²	21
7	Study Of Useful And Important-Aspects Of The <i>Natural Resources</i> M. N. Waghmare and K. S. Junne	25
8	Synthesis And Characterization Of Electrodeposited Sb ₂ Se ₃ Thin films For Various Concentration P. M. Kulal	28
9	Visible Quantum Cutting & Down-Conversion In CaF ₂ : Gd ³⁺ , Eu ³⁺ Phosphor S. R. Jaiswal ¹ , P.A. Nagpure ² , V. B. Bhatkar ² , S. K. Omanwar ³	37
10	Structural And Optical Studies On In Doped Zinc Oxide Thin Films By Spray Pyrolysis Techniques L.H. Kathwate ^a , Nitin T. Gurude ^a , Dipak Kadam ^a , M. B. Awale, S. D. Lokhande ^a , P.M. Kulal ^b , V.D. Mote ^{a*}	42
11	Inhomogeneous Plane Symmetric Cosmological Models With Cosmological Constant ¹ A. R. Gupta and ² M. M. Sancheti	47
12	Cadmium Chloride An Effective Catalyst For Knoevenagel Reaction In Water K. F. Shelke, A. D. Badar and J. B. Devhade	54
13	Studies On Surface Plasmon Resonance In Chemically Synthesized Conducting Polythiophene N. S.Wadatkar* and S. A.Waghuley	58
14	Synthesis, Structural and Optical Properties Of Double- Perovskite SR ₂ FENIO ₆ NANO Composites A. A. Jadhao ¹ , V. G. Pahurkar ^{1a} , P. R. Padole ² , G. N. Chaudhari ^{2a*}	62

15	RECENT TRENDS IN NANOTECHNOLOGY AND ITS APPLICATION IN MEDICINE H. N. Khan , S. B. Pathan , S. T. Kalyankasture , S. S. More	66
16	Comparative Dielectric Study Of 2-Propanol-Water And Glycerol-Water Mixtures Using Tdr Nandkishor Bharose ^{*1} , Satyajit Chavan ^{#1} , Ashok Kumbharkhane ^{*2}	71
17	Effect Of Zr Content On The Structural Characteristics Of Lead Titanate PZT Ceramics Vijendra A. Chaudhari* and Govind K. Bichile	77
18	Cds And Cdzn Quantum Dots Thin Films Prepared By Low Cost Chemical Route Method For Solar Cell Applications Mr. Akash Raut ^a , Mr. Akash Sawate, ^a Mr. Dipak Tonpe ^a , Mr. Pawan More ^a , Mr. Makarand Sonawne ^a , Dr. Avinash Dive ^a , Dr. Ketan Gattu ^a , Dr. Sandip Mahajan ^a , Dr. Vinod Mokale ^a , Dr. Rajesh A. Joshi ^b , Ramphal Sharma ^{a*}	83
19	Structural And Surface Properties Of Pure And Fe Doped Tio ₂ Nanoparticles Prepared By Chemical Route Method Mr. Akash Sawate ^a , Mr. Akash Raut ^a , Mr. Dipak Tonpe ^a , Mr. Pawan More ^a , Mr. Makarand Sonawne ^a , Dr. Avinash Dive ^a , Dr. Ketan Gattu ^a , Dr. Sandip Mahajan ^a , Dr. Vinod Mokale ^a , Dr. Rajesh A. Joshi ^b , Prof. Ramphal Sharma ^{a*}	87
20	Optical Properties Of Copper Oxide And Bismuth Oxide Nanoparticles K. G. Kalmegh ^a and S. A. Waghuley ^{*b}	91
21	Study Of The Density Of Localized States In Zn _{1-x} Mn _x S Chalcogenide Semiconductor D. Age ^a , K. Rathod ^a , F. Khan ^a , M. T. Chakma ^a , A. S. Khune ^a , V. Khadelwal ^a , S. Thorat ^a , P. Khedkar ^a , S. Humbe ^b , A. S. Dive ^b , K. Gattu ^b and Ramphal Sharma ^{a, b*}	96
22	Effect Of Pb And Si Doping On The Electronic Structure Of Mgo: A Density Functional Theory Investigation F. Khan ^a , M. T. Chakma ^a , A. S. Khune ^a , V. Khadelwal ^a , D. Age ^a , K. Rathod ^a , S. Thorat ^a , P. Khedkar ^a , S. Humbe ^b , M. E. Sonawane ^b , A. S. Dive ^b , K. Gattu ^b and Ramphal Sharma ^{a, b*}	102
23	A Dft Study Of The Effects Of Cd Doping On Electronic Structure And Bandgap Energies Of ZnO S. Thorat ^a , P. Khedkar ^a , F. Khan ^a , M. T. Chakma ^a , A. S. Khune ^a , V. Khadelwal ^a , D. Age ^a , K. Rathod ^a , S. Humbe ^b , D. Tonpe ^b , A. S. Dive ^b , K. Gattu ^b and Ramphal Sharma ^{a, b*}	108
24	The Study Of Transference Number Measurements Of Poly (Vinyl Acetate) / Polyindole Composite Films D. J. Bhagat*	113
25	Evaluation Of Antibacterial Activity Of Some Traditionally Used Medicinal Plants (Aegle Marmelos, Pomegranate, Bryophyllum Pinnatum) Against E. Coli. Nivrutti W. Bagalkar*, Jayshree R Netkar* and Ankita R. Tathod	118



LOW TEMPERATURE STEARIC ACID Sol-Gel SYNTHESIS OF NANO CRYSTALLINE MgO

R. N. Wankhade^a, G. V. Korpe^b, N. S. Bajaj^c, V. S. Hingwe^a, S. K. Omanwar^a

^aDepartment of Physics, SGB Amravati University, Amravati (MH), India.

^bDepartment of Chemistry, Shri Shivaji Science College, Akola.

^cDepartment of Physics, Toshniwal ACS College, Sengaon, Dist. Hingoli, (MH), India.

ABSTRACT :

The paper presents the preliminary results on synthesis of biomaterial MgO using a low temperature steric acid sol-gel method. The as prepared sample is characterized through was characterized through x-ray diffraction (XRD), scanning electron microscope (SEM) and UV-VIS spectra for conformation of structure and nature of formed crystalline powder. The well agreement in the results obtained conform formation nano-crystalline powder of MgO. The observation also supports that low temperature synthesized MgO nano-crystalline material can be a promising material for antimicrobial application.

KEYWORDS : MgO, sol-gel synthesis, Inorganic Biomaterials, Metal Oxides .

INTRODUCTION:-

Nanoscience and technology have developed over the past decade as the leading area of science and technologies [1]. Nanotechnology plays a significant role in the industrial revolution. It is concerned with materials, having structures that exhibit significantly novel and improved physical, chemical and biological properties. The focus always made on inorganic materials such as metal and metal oxides due to their ability to withstand harsh process conditions [2]. oxide nanostructures of metal such as iron (Fe), Tin (Sn), Titanium (Ti), Zinc (Zn), Yttrium (Y), Europium (Eu), Zirconium (Zr), Copper (Cu), Manganese (Mn), Vanadium (V), Silicon (Si), Tantalum (Tc), Niobium (Nb), Tungsten (W), Molybdenum (Mo), indium (In), Aluminum (Al), chromium (Cr), Bismuth (Bi), Nickel (Ni), Magnesium (Mg), Antimony (Sb), Gallium (Ga), Cerium (Ce), Gadolinium (Gd), Rhenium (Re), have versatile applications such as Sensors like gas-, bio-, chemical, optical and pressure sensors[3-5]. Some of them have been used in preparation of lithium ion batteries, electrochemical performance for energy storage devices. Due to large electronic band gap and small size crystalline nature metal oxides have been used in dye-sensitized solar cells. [6] Moreover, these nano crystalline oxides have properties as catalytic and photo catalytic agents [7]. Additionally, environmental remediation, field emission non-volatile memory, tunneling devices [8-9], bio-ceramic coating and nano generators are few more application of metal oxides those attracted many scientist throughout the world [10].

Magnesium oxide MgO is an exciting basic oxide that has several applications in catalysis, adsorption and in the synthesis of refractory ceramics [11-14]. It has been evidenced that MgO is a unique solid having high ionic character, simple stoichiometry and crystal structure. Till date many reports were published on variation in method of preparation. Also it is noticed that variation in method affects the particle sizes and shapes that alters the properties of material. Moreover, it has been reported that the shape and size of nano crystalline MgO possesses high specific surface and reactivity, due to enhanced structural defects on their surface [15].

In this paper may be for the first, we have tried to prepare MgO nano crystalline powder by implementing modified low temperature sol-gel synthesis method. During the study the prepared powder sample was subjected to structural and morphological using XRD, SEM and UV-Vis.

EXPERIMENTAL

For current study, stearic acid sol-gel method is explored to synthesize MgO [16]. During the reaction high purity nitrate precursor were taken as a source of Magnesium. The precursor were taken in a china clay and dried in desiccators. The process is done to remove presence of unnecessary water molecules. In same instance the stearic acid was taken in china clay basin and heated slowly on hot plate, till the melt was formed. After formation of gel melt the dried precursor of magnesium nitrate were added to it. After few minutes the few drops of acetic acid added and were stirred continuously. This mixture was heated at around 70°C with continuous stirring till the formation of completely colorless solution. On further heating the color of solution changed from colorless to yellowish and from yellowish to brown. However at around 100°C, it becomes hot red. At this stage of reaction brown fumes were progressed from the solution. After then the solution was allowed to cool to get a pale yellow gel.

The dry gel is was then heated at around 200°C, at this stage the solution was burnt slowly with dull red flame and evolution of thin sized and light weighted carbon flakes. However, the residue was pyrolysed at ~ 400°C into black charcoal / resin which burnt at ~ 700°C yielding a white and spherical fine structured net of MgO. Because of combustion during the reaction the net were formed. The formed net was then gently pressed to get fine white powder.

As synthesized powder sample was then used for XRD (Rigakuminiflex X-ray diffractometer), SEM (Philips XL 30 SEM system) Photoluminescence Hitachi F-7000 spectrophotometer and Defused UV spectra.

RESULT AND DISCUSSION

X-ray diffraction pattern

XRD exhibits the formation of fine and crystalline MgO powder. The structural conformation was made by matching XRD pattern represented in figure 1 with standard data from ICDD file (00-004-0829). The peak to peak agreement in XRD pattern of MgO and ICDD date supports the formation of mono crystalline, single phase cubic structuredMgO. Also the symmetry allowed crystal structure properties for MgO are centro symmetric, and mineral classification halite (Group), oxide (Subgroup)

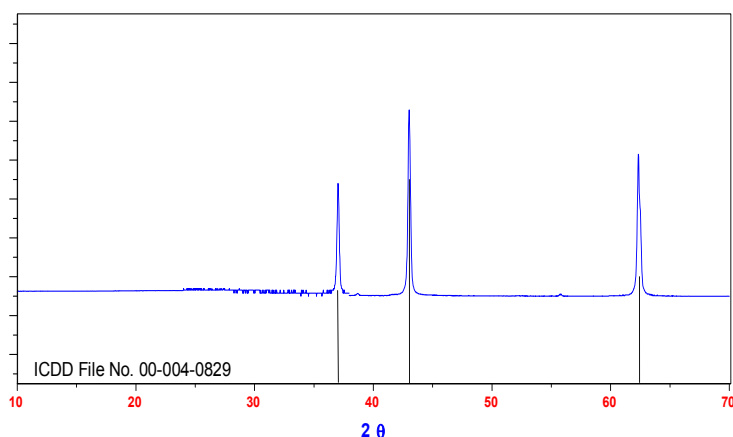


Figure 1 XRD pattern for low temperature annealed Cubic MgO

The Peak broadening supports the formation of Nanocrystalline form Cubic MgO. The average crystallite size was found to be 3.65 nm calculated from diffraction peaks using the Debye–Scherrer equation.

Surface analysis

The surface morphology and size of particles of MgO was examined through High Resolution SEM. Figure 2 represents the HR-SEM image of MgO. The SEM image reveals the consistent shape of crystal of as prepared material. However there are some agglomerations in the region of imaging. The average size of particles in SEM agrees with the size revealed by XRD pattern.

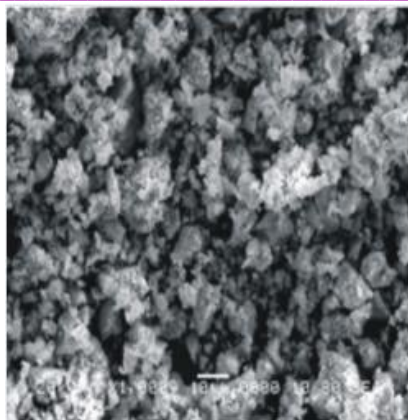
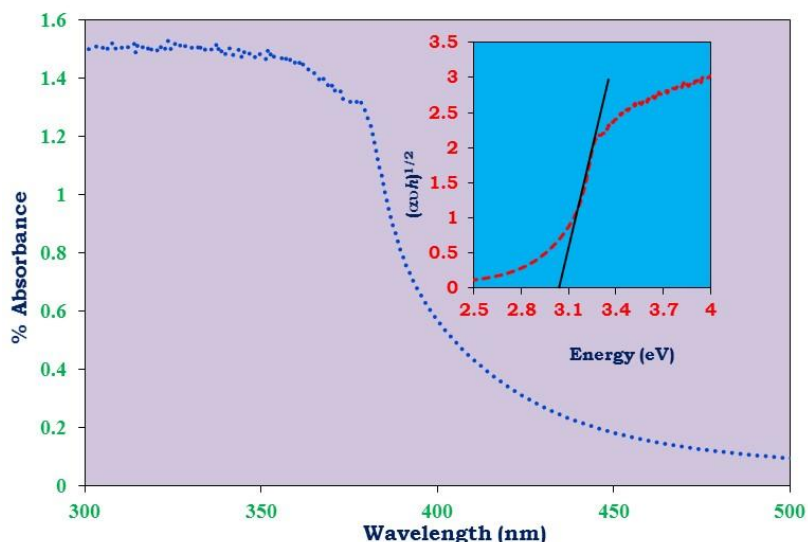


Figure 2 HR-SEM image of as-synthesized MgO

UV analysis

Figure 3 denotes UV visible absorption spectrum of MgO. It evidently confirms an intense band-to-band absorption in the ultra violet region. The UV visible spectra produced by the prepared MgO show complete agreement with the literature materials. Band gap value was determined by extrapolation of the linear portion of $(\alpha h\nu)^{1/2}$ curve versus the photon energy ($h\nu$) as 2.9 eV as shown in inset of figure 3.



**Figure 3 UV-VIS spectra for as synthesised MgO
(Inset: linear portion of $(\alpha h\nu)^{1/2}$ curve versus the photon energy ($h\nu$))**

The band gap at 2.9 eV clearly supports the blue shift in band gap which confirms the formation of smaller sized MgO Nano crystals and the presence of strong quantum confinement effect [16]. Additionally, the shift supports the reduction in the particle size. The radius of particles was estimated using the hyperbolic band model (HBM). The calculated value of radius was found in concurrence with the particle size calculated from XRD and HR-SEM.

CONCLUSION

The MgOnano-crystalline powder was successfully prepared by using a stearic acid sol-gel synthesis. The XRD pattern of as prepared powder sample agrees with ICDD file and supports the complete crystalline nature of prepared material. The HR-SEM shows some agglomeration in the sample; however the formed particles have confined size. The agreement in particle size estimated by XRD, SEM and UV-VIS confirms

the formation of nano crystalline material that can be used in variety of application due to confined band gap and modified surface morphology.

REFERENCES

1. R. Rajendran, C. Balakumar, S. Jayakumar, E. M. Rajesh, *Int. Jour. Engn. Sci. Tech.* 2, 202 (2010).
2. M. Sundrarajan, J. Suresh, R Rajiv Gandhi, *Dig. Jour. Nano. & Bio.* 7, 983 (2012).
3. I. Khan, K. Saeed, I. Khan, *Ara. Jour. Chem.* 1, 29, (2017).
4. *Metal Oxide Nanostructures and their Applications*, Edited by A. Umar, Y. B. Hahn Published by American Scientific Publishers, CA, USA, (2009).
5. Y. Sun, S. B. Liu, F. L. Meng, J. Y. Liu, Z. Jin, L. T. Kong, J. H. Liu, *Sensors*, 12, 2610 (2012).
6. A. P. Tomás, A. Mingorance, D. Tanenbaum, M. L. Cantú, *Metal Oxides in Photovoltaics: All-Oxide, Ferroic, and Perovskite Solar Cells, The Future of Semiconductor Oxides in Next-Generation Solar Cells.* (2001).
7. N. K. Elumalai, C. Vijila, R. Jose, A. Uddin, S. Ramakrishna, *Mater. Renew. Sustain. Energy* 4, 11, (2015).
8. S. E. Ahn, B. S. Kang, K. H. Kim, M. J. Lee, C. B. Lee, G. Stefanovich, C. J. Kim, Y. Park, *IEEE Ele. Device Lett.*, 30, 229 (2009).
9. J. C. Ranua´rez, M. J. Deen, C. H. Chen, *Micro. Elect. Relia.* 46 1939 (2006).
10. R. B. Heimann, *CMU. Journal* 1(1) 23 (2002).
11. B.Q. Xu, J.H. Wei, H.Y. Wang, K.Q. Sun, Q.M. Zhu, *Cat.Today*, 68, 217 (2001).
12. V.R. Choudhary, V.H.Rane, R.V. Gadre, *J. Catal.* 145, 300 (1994).
13. S. Utamapanya, K.J Klabunde, J.R Schlup, *Chem. Mater*, 3, 175 (1991).
14. S. Rajagopalan, S. Koper, S. Decker , K.J. Klabunde, *J.Eur.Chem*, 8, 2602 (2002).
15. K.J. Klabunde, J. Stark, O. Koper, C. Mohs, D.G. Park, S. Decker, Y. Jiang, I. Lagadic D. Zhang, *J. Phys. Chem.* 100, 12142 (1996).
16. N. S. Bajaj, S. K. Omanwar, *J Sol-Gel SciTechnol* 75 1, (2015).



STUDY OF ANTIBACTERIAL ACTIVITY OF PURE AND AL DOPED ZnO NANOCRYSTALS ON *BACILLUS THURINGIENSIS* NCIM2130 AND *PSEUDOMONAS CF. MONTEILII* 9 CULTURES

R. S. Shaikh¹, R. B. Mahewar.² and L. S Ravangave³

Physics research Laboratory, Department Of Physics SSGM College LohaDist :Nanded MS (India)

Email: ¹shaikhraju99@gmail.com, ³rameshbalojimahewar@gmail.com²lsravangave@gmail.com,

ABSTRACT :

Hexagonal wurtzenano crystalline powder of pure and Al doped ZnO nanostructure have been prepared from reagent grade zinc acetate and sodium hydroxide using Sol Gel chemical precipitation process. XRD pattern of pure and Al doped ZnO represent the wurtize hexagonal crystal structur. DopedZnO(Al) sample show decrease in grain size as compared to grain size of pure ZnO. Significant tuning of optical band gap and of particle size was observed on calcinations of ZnO(Al) samples. SEM images shows Varying Morphology of Al doped ZnO. The Varying morphology of hexagonal ZnO(Al) nanoclusters may be applicable as an antibacterial and antifungal agent. The antibacterial activity of pure and Al doped ZnO nanoparticles have been tested against *Bacillus thuringiensis* NCIM2130 and *Pseudomonas cf. monteilii* 9 cultures by using slightly modified Agar Well Diffusion method. The both the samples shows antibacterial activity against *Bacillus thuringiensis* but Al doped ZnO shows more effect as compared to pure ZnO.

KEYWORDS : ZnO NP's, Al doped ZnO nanostructure, Pl spectra, Antibacterial activity.

1. INTRODUCTION

Zinc Oxide is an important II-VI group wide energy band gap semiconductor with optical properties that permits stable emission at room temperature having immense application in sensors, field emission and photonic devices. It exhibits a wide variety of morphologies in the nano regime that can be grown by tuning the growth habit of the ZnO crystal[1]. Zinc oxide (ZnO) is an extensively studied nowadays, since it is a multifunctional direct wide band gap II-VI semiconductor (3.37 eV), which exhibits attractive properties such as large exciton binding energy (60 meV), The wide-band gap energy of ZnO semiconductor enables huge potential for electronic and optical applications. It has unique piezoelectric properties that are very essential to enhance the performance of electromechanical devices. It is a biodegradable material suitable for medical and biological applications. [2]. The multiple morphologies of Zinc Oxide such as belts, ribbons, cables, rods, tubes, rings, springs, helices, bows, tetra pods, spirals, needles and films was forms the basis of its versatile applications[3].

ZnO exhibits significant antimicrobial activities when particle size is reduced to the nanometer range, then nano-sized ZnO can interact with bacterial surface and/or with the bacterial core where it enters inside the cell, and subsequently exhibits distinct bactericidal mechanisms. The reduced particle size was leading to enhance surface reactivity. ZnO is a bio-safe material that possesses photo-oxidizing and photocatalysis impacts on chemical and biological species. ZnO Nanoparticle of size 20-25 nm were used against pathogenic bacteria *Staphylococcus aureus* (Gram positive) and *Salmonella typhimurium* (Gram negative) and also first time against two plant fungi *Aspergillus* strain of *flavus* and *fumigatus*. The growth analysis data indicated that the ZnO NPs have significant bactericidal effect on both the bacteria. [4-5].

Zinc Oxide (ZnO) in nanostructure has unique physical and optical properties which can be used in variety of application such as a oxide coating for solar cell, gas sensors, catalysts photo-electronic device,

optoelectronics, UV photo diode, photo chemical, electronics, photo detectors, schottky diode, LED device, because ZnO exhibit near-band-edge PL emission that originates from exciton transitions [6].

ZnO exhibit PL spectra under 325nm continuous excitation give significant UV emission band with a peak at 3.25 eV and a band width of 160 meV. PL spectra under 355-nm, 35-ps pulse excitation exhibited a spectrally narrowed emission band with a peak at 3.20 eV and a spectral width of 35 meV. The lasing phenomena is ascribed to the amplified spontaneous emission (ASE) by coupling of the micro cavity effect of ZnO nanorods and high intensity excitation, leads to be used in construction of laser [7].

Many of the workers across the world were doing research on this important ZnO nanostructure and their use in antibacterial activity

In this paper we report the synthesis of hexagonal symmetry pure ZnO Nano clusters and Aluminum doped ZnO nanostructures using Sol Gel chemical Precipitation method, the influence of their structural and morphological changes on Uv-Visible absorption, Photoluminescence emission properties on sintering has been reported.

The particle size of the ZnO grains is calculated by using well known Scherer's equation (1) [8]

$$D = \frac{0.94\lambda}{\beta \cos\theta} \text{----- (1)}$$

Where **D** is the crystalline size nanoparticles (nm), λ is the wavelength of incident x-ray (nm), β is the full width at half maxima and θ is the diffraction angle. The lattice constants a, b and c have been estimated by using relation (2) [9].

$$\frac{1}{d^2} = \frac{4}{3} \left\{ \frac{(h^2 + hk + k^2)}{a^2} \right\} + \left\{ \frac{l^2}{c^2} \right\} \text{----- (2)}$$

Estimation of energy band gap (E_g) from statistical analysis of optical spectra equation (3) have been used.

$$E_g = \frac{hc}{\lambda} \text{----- (3)}$$

Where h is planks constant 6.63×10^{-34} Jule-sec., C is velocity of light and λ is wavelength at near band edge.

2. MATERIALS AND METHODS

Economically cheap and simple Chemical precipitation called as Sol-gel preparation is used for synthesis of Al doped zinc oxide nanoparticles ZnO(Al). High purity zinc acetate and sodium hydroxide were used as starting materials.. Initially appropriate molarity (0.75M) solutions of Zinc acetate and sodium hydroxide were prepared. These solutions were individually stirred for two hours. In zinc acetate solution 5% of Al salt solution was added slowly. To this solution sodium hydroxide solution was added slowly drop wise in a molar ratio of 1:2 with stirring continuously at appropriate temperature (50 °C). The stirring was continuous for two hours maintaining temperature constant until formation of gel. The obtained gel is kept overnight at room temperature and centrifuged at 5000 rpm. The precipitate was washed thoroughly with distil water thrice. The white colored residue of Al doped ZnO was dried in oven at 100°C for two hours. The dried product was ground to fine powder using agate mortar and pestle. The samples were calcined at different temperatures (200, 400, 600°C). The as-prepared and sintered samples were characterized and results were discussed.

3. RESULTS AND DISCUSSION:

3.1 Structural Investigations:

The XRD spectra for pure ZnO was recorded in the range $2\theta = 20-80^\circ$ and presented in fig. 1. Pure ZnO sample show evidence of wurtzite hexagonal crystal structure. XRD pattern is well matched with standard JCPDS card number (36-1451). Sharp peaks at different diffracting angles (2θ) correspond to different

reflections from the planes (100), (002), (101), (102), (110), (103) and (200). Similar structure of hexagonal ZnO nano particles was investigated in the literature [10]. The high intensity and narrow line width indicate the good crystallites [11] of ZnO-NPs. The particle size nm estimated from XRD data by using relation (1) was 48 nm.

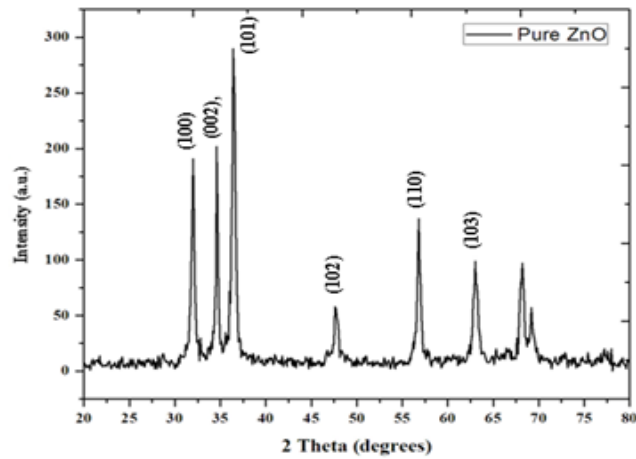


Figure 1 XRD of ZnO(AI) Nanostructure

XRD pattern of Al doped ZnO nanoparticles was shown in fig. 2. As-prepared and calcined ZnO(Al) exhibit wurtzite crystal symmetry similar to pure ZnO. The crystallinity was observed improved on increasing temperature of calcinations. XRD pattern assigned to wurtzite phase and no other common secondary crystalline phases such as Al_2O_3 aluminum oxide or graphite were noticeable.

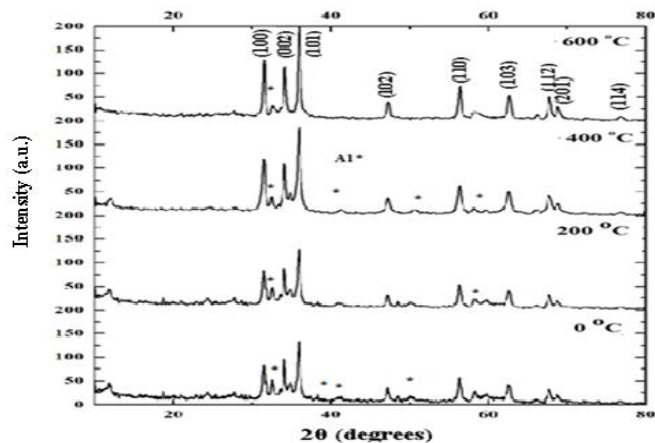


Figure 2. XRD Of ZnO(Al) Nanoparticles

On increasing the calcination temperature some peaks assigned to Al were noticed in the XRD spectra. This concluded that Al was substituted at the Zn site on replacing Zn. The average grain size of the samples was estimated with the help of equation (1) using the full width at half maxima of (100), (002), (101), (102), (110), (103), (200), (112), and (201) of the x-ray diffraction peaks and displayed in table 1. The average crystalline size was increased with increase in temperature of calcinations. The particle size estimated was found decreased as compared to particle size of pure ZnO samples. The lattice constants of pure and as-prepared and calcined ZnO(Al) was calculated by using equation (2) shown in table 1. The values of lattice constants a and b was found to decreased as calcination temperature increased.

Sr. No.	Samples	a (Å ^o)	c (Å ^o)	Grain Size D (nm)	Average Grain Size SEM (nm)
1	ZnO(Al)0 ^o c	3.2785	5.2639	36	60.48
2	ZnO(Al)200 ^o c	3.278	5.1429	38	76.71
3	ZnO(Al)400 ^o c	3.282	5.2568	44	76.78
4	ZnO(Al)600 ^o c	3.1806	5.2504	47	76.80

a. Surface Morphology Study:

The SEM images of Al doped ZnO-NPs were shown in fig.3 exhibits distinct, nonhomogeneous porous network with an average grain size 68 nm that was computerized and visualize in micrographs. The small crystalline agglomerated to form nano fused clusters that was seen in the surface morphology of ZnO(Al). The microstructure was observed changes to hexagonal nanorods at high temperature. The size of nanorods and nanograins were varying from 37 to 86 nm. The average grain size ranges from 68.48 to 76.80 nm was displayed in table 1 above. ZnO(Al) nanostructures exhibit significant varying morphology and may be used as antibacterial agent.

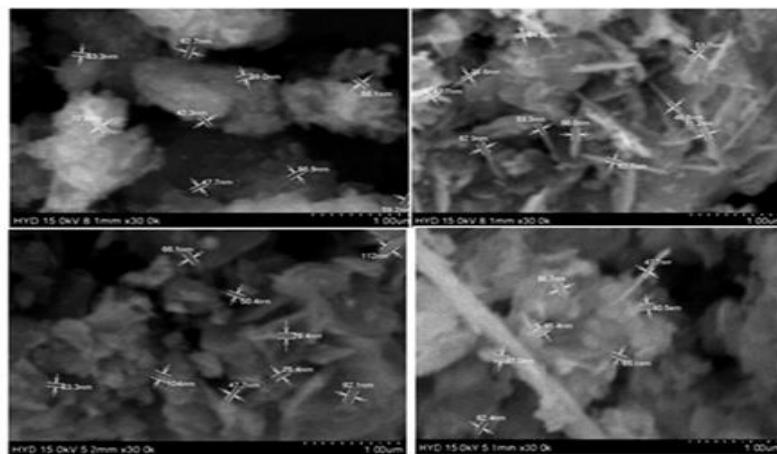


Figure 3 SEM Micrographs of ZnO(Al) Nanoparticles

b. UV-Visible Absorption Study:

The absorption spectrum of pure ZnO, and as prepared and calcined ZnO(Al) nanopowder is shown in fig.4. Pure ZnO sample exhibit a strong absorption peak at about 378 nm. The significant blue shift of 378 nm peak to 358 nm was observed for Al doped ZnO samples. This confirms the decrease in particle size on doping. The band gap was calculated using equation (3). The estimated band gap and near band edge wavelength is tabulated in table 4. On calcination at different temperatures effectively tuned the band gap. This is attributed to change in microstructure of ZnO(Al) and grain size.

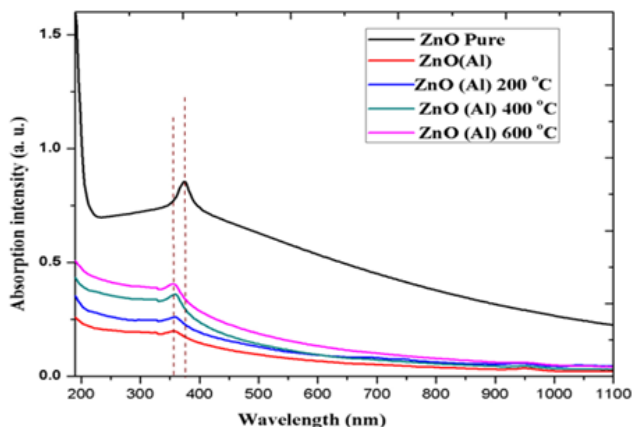


Figure 4 Uv-Visible Spectra of pure ZnO, as-prepared ZnO(Al) and sintered ZnO(Al) Nanoparticles

As prepared ZnO(Al) exhibit 3.47 eV significant band gap as compared to pure ZnO nanostructure (3.28 eV). The band gap was observed decreased on increasing temperatures of calcinations (200 to 600 °C). The decrease of band gap is attributed to increase in grain size on increasing temperature. The pure and Al-doped ZnO nanostructure exhibit higher band gap and lower particle size may be used in optoelectronics, photoelectrochemical cells, and for biological applications[2].

Sample	λ at near band edge (nm)	Energy band gap (eV)
ZnO (Al) °C	358	3.47
ZnO (Al) 200 °C	365	3.40
ZnO (Al) 400 °C	370	3.36
ZnO (Al) 600 °C	375	3.31
ZnO Pure	378	3.28

3.4 Antibacterial Activity of pure ZnO and doped ZnO

In order to study the antibacterial activity of doped ZnO nanoparticles against *Bacillus thuringiensis* NCIM2130 and *Pseudomonas cf. monteilii* 9 cultures slightly modified Agar Well Diffusion method was used. The pure ZnO and Al doped ZnO nanopowder were calcined at 600 °C and used for antibacterial study. The inhibition zone size was measured. Pure ZnO shows inhibition zone size of 16 mm while Al doped ZnO shows increase in zone size up to 26mm. The pure ZnO and Al doped ZnO never show antimicrobial activity against *Pseudomonas cf. monteilii* 9 and not presented in form of photoplate. While comparing inhibition zone of pure ZnO with respect to ZnO(Al) against *Bacillus thuringiensis* NCIM2130 and *Pseudomonas cf. monteilii* 9, Al doped compound is more active than pure ZnO. The photo plate of Al doped ZnO nanostructures calcined at 600 °C have been shown in figure 5.

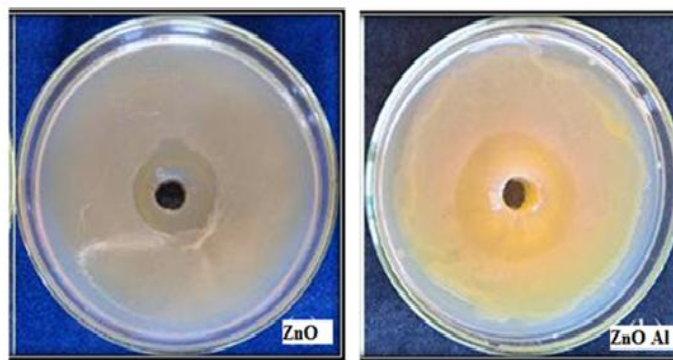


Figure 5 Photo Plate Inhibition of *Bacillus thuringiensis* NCIM2130 by ZnO Al in comparison with ZnO pure

4. CONCLUSION:

Pure and Al doped zinc oxide nanostructure exhibit hexagonal wurtzite crystal symmetry with different surface morphology (porous nano clusters to nanorods) were successfully prepared by Sol-Gel Precipitation Method. SEM images concluded that surface morphology effectively tuned on calcinations of ZnO(Al) powder from nanocluster to nanorods. XRD spectra exhibit single phase wurtzite nano crystalline structure of ZnO(Al). The band gap was increased by small doping % of Al from 3.28 to 3.47 eV. The calcination temperature significantly tuned the band gap of ZnO(Al). The pure and Al-doped ZnO nanostructure exhibiting higher band gap and lower particle size with modified surface morphology may be used in optoelectronics, devices and for biological applications. The antibacterial study concluded that Al doped ZnO calcined at 600 °C can be used as antibacterial agent against *Bacillus thuringiensis* NCIM2130.

Acknowledgement: Authors are acknowledges to Director, Physics Research Centre Shri Sant Gadge Maharaj College Loha, Dist. Nanded (MS) India.

REFERENCES

- [1]. George Varughese, K.T Usha, A.S.Kumar, "Characterization and Band gap Energy of Wurtzite ZnO:La, nanocrystallites, *International Journal of Latest Research in Science and Technology* 20143, (3), 133-136
- [2]. Basavaraj S. Devaramani, Ramaswamy Y.S., Babu A. Manjasetty and T.R. Gopalakrishnan Nair, *The Novelty of Syntheses & Varied Applications of ZnO nano systems, International Conference on Frontiers in Chemical Research (ICFCR)*, 2008, 206-213.
- [3]. Pan Z. W., Dai Z. R. and Wang Z. L., *Nanobelts of semiconducting oxides, Science*, 2001, 291, 1947-49.
- [4]. Amna Sirelkhathim, Shahrom Mahmud, Azman Seeni, Noor Haida Mohamad Kaus, Ling Chuo Ann, Siti Khadijah Mohd Bakhori, Habsah Hasan, Dasmawati Mohamad, *Review on Zinc Oxide Nanoparticles: Antibacterial Activity and Toxicity Mechanism, Nano-Micro Lett.*, 2015, 7(3):219-242.
- [5]. Navale Govinda R., Thripuranthaka M., Late Dattatray. J, and Shinde Sandip S, *Antimicrobial Activity of ZnO Nanoparticles against Pathogenic Bacteria and Fungi*, *JSM Nanotechnology & Nanomedicine*, 2015, 3(1):1033-39.
- [6]. Geon Joon Lee and Young Pak Lee, *Photoluminescence and Nonlinear Optical Properties of Semiconductor Nanocomposites Consisting of ZnO Nanorods and CdS Nanodots, Journal of the Korean Physical Society* 2011, 58,(5), 1290-1294.
- [7]. Geon Joon Lee and Young Pak Lee, *Photoluminescence and Lasing Properties of ZnO Nanorods, J. Korean Phy. Soc.*, 2011, 5, : 1624-1629.
- [8]. Cullity B. D. and Stock S.R., *Elements of X ray diffraction. Prentice Hall, New Jersey, 3 edition* 2001.
- [9]. Buerger M. J.. *X-ray Crystallography, John Wiley and Sons, New York, 3 edition*, 1962.
- [10]. Pal B. and Giri P. K., *Defect Mediated Magnetic Interaction and High Tc Ferromagnetism in Co Doped ZnO Nanoparticles, Journal of Nanoscience and Nanotechnology* 2011, 11, 1-8.
- [11]. Kaur J., Kumar P., Thangaiyah Stephen S. and Thangaraj R., *Structural, optical and fluorescence properties of wet chemically synthesized ZnO: Pd²⁺ nanocrystals, International Nano Letters*, 2013, 3(4), 3-7.

[12]. FakhroueianZ., HarsiniF., M., ChalabianF. , Katouzian F., ShafiekhaniA. , EsmailzadehP., *Influence of Modified ZnO Quantum Dots and Nanostructures as New Antibacterials*, *Advances in Nanoparticles*,2013, 2, 247-258 ()

A MINI REVIEW ON SYNTHESIS METHOD FOR FERRITE NANOPARTICLES

R.V. Kotalkar and L.V.Thakre

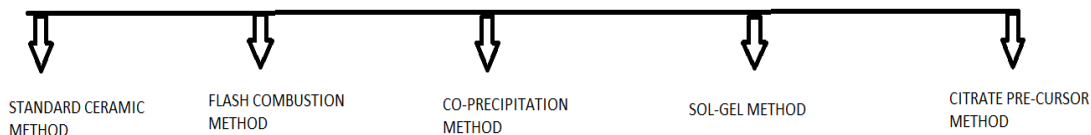
Department of physics and electronics, Dayanand Science College, Latur.

ABSTRACT :

This paper reports different synthesis methods of ferrite nanoparticles. Synthesis method plays a crucial role in cation distribution and particle size. Method of synthesis affect ferrite nanoparticles critically on both the magnetic moments of cation distribution. This paper depict different synthesis technique of ferrite nanoparticles such as ,standard ceramic technique, flash combustion method, co-precipitation method, sol-gel method, citrate precursor method. The structural and magnetic properties of ferrite nanoparticles can be studied by different methods of synthesis.

Methods of synthesis of ferrite nanoparticles

- 1] Standard ceramic method
- 2] flash combustion method
- 3] Co-precipitation method
- 4] Sol-gel method
- 5] Citrate precursor method



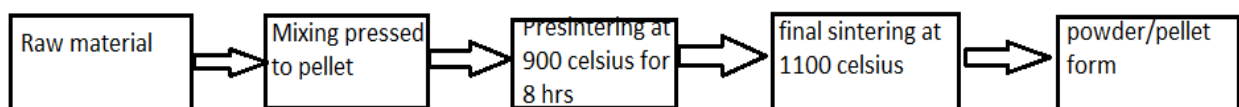
KEYWORDS : Ferrite nanoparticles, synthesis method, structural and magnetic properties.

INTRODUCTION:-

Ferrites have many important applications in industry, modern telecommunication and electronic devices [1-2]. Our modern telecommunication system would not be possible without ferrites. The large scale production of television in 1950's was main reason for expansion of ferrite industry[2-3]. Ferrite nanoparticles are very much sensitive to the chemical composition and method of preparation and also for industrial applications.

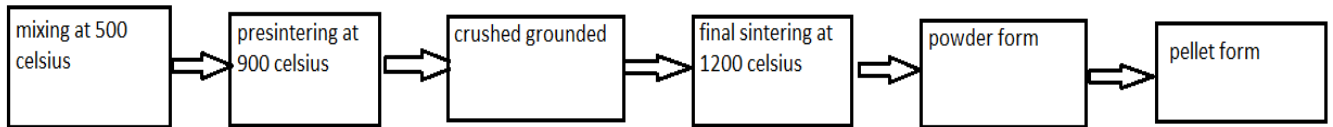
STANDARD CERAMIC TECHNIQUE

Consists of heating 2 non- volatile solids which react to form required products. The number of crystallites in contact may be increased by pelletising the powders by using hydraulic press. In this method sample purity is typically examined by powder X-ray diffraction.



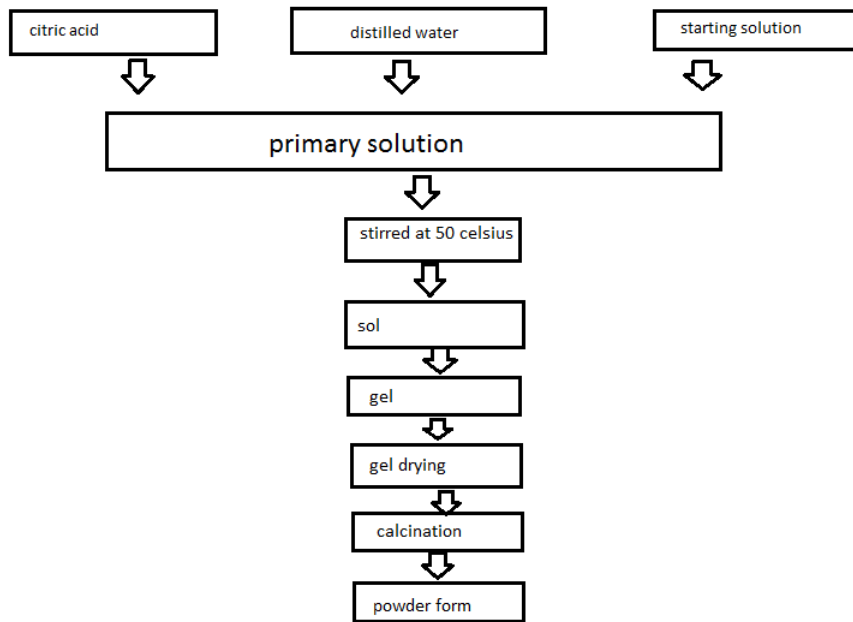
Flash Combustion Method:-[3-4]

In this method reactants are mixed together to form a pellet.



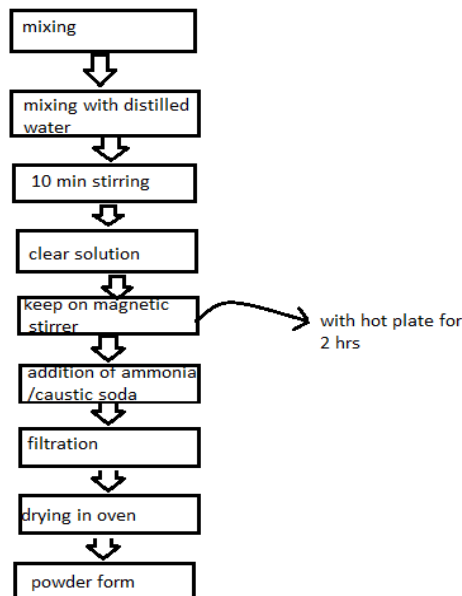
Sol-Gel Method:-

This method is well known for low temperature synthesis of glass material. A concentrated solution or colloidal solution of reactants, the sol is formed and then gel is formed5-6]



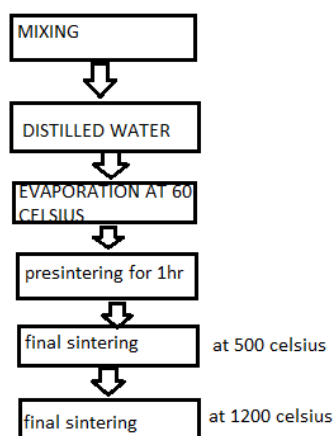
Co-Precipitation Methods:-

This method is very simple, cheap and easily available.[7-8]



The mixture is filtered, dried and then heated to give the final product in powder form. This method is economical, simple and eco-friendly.

Citrate Pre-Cursor:-[7]



REFERENCE:

- [1] J. Smit and H. P. J. Wijn Ferrites (Philips Technical Library, Eindhoven, 1959).
- [2] A.B. Gadkari, T.J. Shinde, P.N. Vasambekar, Mater. Chem. Phys. 114 (2009) 505
- [3] L. Gama, A.P. Diniz, A.C.F.M. Costa, S.M. Bezende, A. Azevedo, D.R. Cornejo, Physica B: Conden. Matter. 384(2006) 97.
- [4] S.E. Jcoba, S. Dukalde, H.R. bertorella, J. Magn. Magn. Mater. 2253(2004) 272
- [5] A.Verma, T. C. Goal. R. G. Mendiratta and M.I. Alam, Mater Sci. Eng. B. 60 (1999) 156.
- [6] A. M. Abdeen, J. Magn. Magn. Mater. 192 (1999) 121.
- [7] WORLDWIDESCIENCE.ORG
- [8] N. Guigue-Millot, S. Begin-Colin, Y. Champion, M. J. Hytch, G. Le Caer, P. Perriat, J. Solid StateChem. 170, 30 (2003).
- [9] B. Parvatheeswara Rao, K. H. Rao, K. Trinadh,
- [10] A. Goldman, Modern Ferrite Technology (vanNostrand Reinhold, New York, 1990) 157.



DIELECTRIC RESPONSE OF IRON EXCHANGED FLY ASH ZEOLITE A

A. N. Kalyankar

Bahirji Smarak Mahavidyalaya Basmath, Maharashtra, India-431512.

Corresponding Author:kalyankaranil@gmail.com

ABSTRACT :

Coal is the main source fuel for generation of electricity in India. Large amount of coal burning produces huge amount of coal fly ash. In this paper, the Zeolite type A synthesized using fly ash is modified to iron form Fe-A zeolite. The zeolite Fe-A is used for studying the dielectric properties at different temperatures and fixed frequency. In the present study the variation of dielectric parameter such as dielectric constant (ϵ') depends upon the concentration of metal ions loaded in the sample during ion exchange and the temperature. Dielectric response of zeolite is the tool to know utilization of this activated hazardous solid waste material fly ash to study necessary conditions for catalytic, sensor, electronic applications of zeolite.

KEYWORDS : Zeolite A, Fly ash, Dielectric.

1. INTRODUCTION:

Fly ash is obtained from coal burning in thermal power stations. In India three fourth of total generated power is achieved from coal burning in various thermal power stations [1]. Zeolites are aluminosilicates and their types are known by their three dimensional structural arrangement of SiO_4 and AlO_4 tetrahedra. The chemical composition is given by the formula $\text{M}_{x/n}(\text{AlO}_2)_x(\text{SiO}_2)_y \cdot z \text{H}_2\text{O}$ where M is the cation compensating the negatively charged framework. Zeolite applications in many disciplines are well known. Synthesis of zeolites using coal fly ash is a best alternative to utilize this hazardous solid waste. Since coal fly ash includes a large amount of silica and alumina, they are easily converted into zeolite by hydrothermal treatment in an alkaline solution [1, 2]. Many researchers have been synthesized zeolite A from fly ash [3]. The effect of temperature in dielectric study of zeolite is known well [4]. This paper reports the dielectric effects on zeolite Fe-A synthesized from coal fly ash.

2. MATERIALS & METHODS:

The starting material was fly ash obtained from thermal power station, Parali Vajinath, Maharashtra (India). The fly ash zeolite A synthesized using fly ash based on previous study [5] is used. The zeolite A thus formed is ion exchanged with 1 M solution of NH_4NO_3 at 80°C for 12 h. This process was repeated thrice so as to get proper ion exchange. The product was filtered, air dried at 60°C for 24 hr and then calcined at 450°C so that the zeolite $\text{NH}_4\text{-A}$ is decomposed into zeolite H- A i.e. protonic form then the zeolite which when ion exchanged with 0.1M, 0.2M and 0.3M solution of iron nitrate [$\text{Fe}(\text{NO}_3)_3 \cdot 9\text{H}_2\text{O}$], so as to obtain the $\text{Na}_{(1-x)}\text{Fe}_x\text{A}$ zeolite where $x = 0.1, 0.2, 0.3\text{M}$.

2.1. Characterisation:

The physical properties of coal fly ash and synthesized products were measured as follows. The chemical composition fly ash was determined by using a X-ray Fluorescence Spectroscopy. The chemical composition was analyzed using X-ray fluorescence analysis equipment (Phillips PW -2404). The sample phases were characterized by X-ray diffraction (XRD) using a (Phillips PW 3710) diffractometer with $\text{Cu-K}\alpha$ radiation (1.5496\AA).

2.2. Dielectric Measurement:

The samples of Na-A and Fe- A zeolite were compressed to form pellet of 10 mm diameter and 1 mm thickness. The pellets were heated to 300⁰C to obtain a hard solid sintered material. The pellets were polished with silver paste for good electrical contact. The dielectric constant (ϵ') was measured at the frequency range 1 KHz and 10 KHz at different temperature using LCR-meter (HP-4284A).

3. RESULTS AND DISCUSSION:

3.1. XRF

Table1. Chemical composition of fly ash

Oxides	% wt	Mol/100 g of fly ash
SiO ₂	70.23%	1.169
Al ₂ O ₃	23.27%	0.228

The elemental composition analysis by XRF in Table 1 indicated that coal fly ash contained large quantities of silica and alumina which are the two main components in zeolite. The chemical analysis of the fly ash used as the starting material in this work showed it to be a high-silica ash with the mole ratio of SiO₂: Al₂O₃ = 5.127: 1.

3.2. XRD

The X-ray diffraction pattern of fly ash based zeolite H-A and its exchanged form Fe-A is shown in fig.1. The d values are compared with the standard [6]. The peaks located in the region of 7° < 2θ < 34.1° are representative peaks of a typical H-A zeolite. As can be seen in Figure 1, the intensity of peaks corresponding to H-A zeolite decreased, whereas, the intensity of peaks corresponding to iron increased on increasing the iron loading on H-A zeolite.

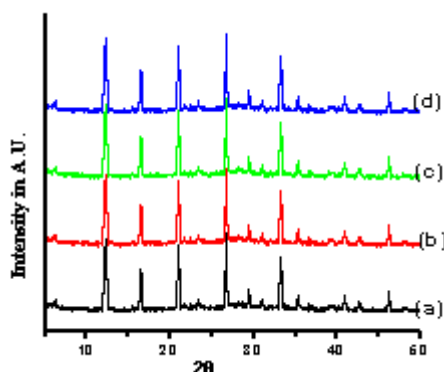
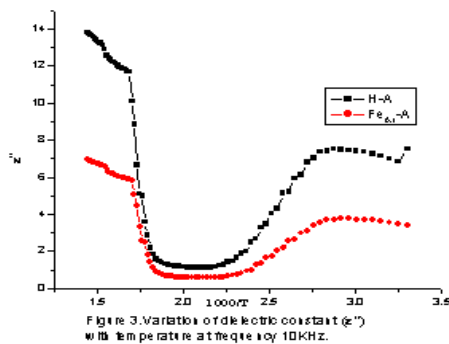
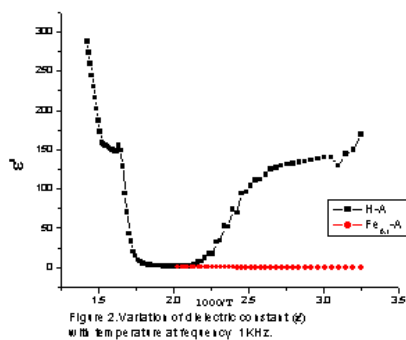


Figure1. XRD of (a) Na-A (b) Na_(1-0.1)Fe_{0.1}-A (c) Na_(1-0.2)Fe_{0.2}-A (d) Na_(1-0.3)Fe_{0.3}-A

The XRD for Fe-A were found to be similar to that of original H-A sample, indicating that there is no structural changes occur after ion exchange with iron nitrate [7].

3.3. Dielectric Measurement:

The variation of dielectric constant (ϵ') with temperature for H -A and Fe_{0.1}-A zeolites at fixed frequency 1KHz and 10KHz are shown in figure 2 and 3. In Figure 2, the permittivity (ϵ') of zeolite HA was found to decrease at low temperature with further increase in temperature the dielectric constant increases constantly. The lattice scattering of the charge carriers increases due to increase in thermal energy after the phase transition. This produces a decrease in the mobility, polarizability and permeability. It can be seen that (ϵ') decrease with increasing frequency, which is the general trend of dielectric materials.



4. CONCLUSION:

Zeolite Fe-A is successfully synthesized from solid waste material fly ash and it shows no structural change after modification with iron. The zeolite H- A and Fe-A shows good response for dielectric applications.

ACKNOWLEDGEMENT:

The author acknowledges Prof.A.L.Choudhari for contribution in experimental facility and discussion.

REFERENCES:

1. Electrical India Magazine, February 2019.
2. Hui Deng, Yan G ,RSC Adv., 2015,**5**, 9180-9188.
3. Subotic B, Ckrtic D, Smit I, Sekovanic L ,Journal of Crystal Growth,1980, **50**,498-508.
4. M.E. Franke and U. Simon, Solid State Ionics **118**, 1999,311-316 .
5. Kalyankar A. N., Joshi A.A., Choudhari A.L, Int. J. Basic & App. Res.**01**,(2011), 59-63.
6. D.W. Breck, Zeolites Molecular Sieves,Wiley,New York, 1971.
7. Hsiao-Lan Chang ,Wei-Heng Shih, Ind. Eng. Chem. Res., 2000, 39 (11), 4185–4191.



PHOTOVOLTAIC AND STRUCTURAL PROPERTIES OF PTh-co-PANi-SiO₂ COPOLYMER COMPOSITE SYSTEMS

S. R. Takpire , K.R. Nemade, S.A. Waghuley*

Department of Physics, Dr. B. N. college of Engg. and Tech., Yavatmal-445 001, India.

*Department of Physics, Sant Gadge Baba Amravati University, Amravati-444 602, India.

* Corresponding author e-mail: sandeepwaghuley@sgbau.ac.in (S.A. Waghuley)

ABSTRACT :

In this research work, polythiophene (PTh)-co-polyaniline (PANi)- silicon dioxide (SiO₂) copolymer composite was synthesized for complex optical study. The spotlight of the work was to calculate complex optical properties PTh-co-PANi-SiO₂ copolymer containing different types of monomer. The optical band gap was found to be 3.85 of as synthesize polythiophene (PTh)-co-polyaniline (PANi)-silicon (Si) copolymer composite polythiophene (PTh)-co-polyaniline (PANi)- silicon dioxide (SiO₂) copolymer composite. Analysis of as prepare photovoltaic material was done through FESEM and UV-vis characterization.

KEYWORDS : composite: Phtovoltaic property: UV-vis.

INTRODUCTION

In last decade recognized significant development in the propose, synthesis, and characterization copolymer base optical system but linger challenge to achieve well-organized [1,2]. Conjugated polymers and its composites have high optoelectronic properties, potential used in low-cost electronic and optical devices [3,4,5]. attention as promising solar cell absorber. For the p-n junction operation of solar cell, there is need of the buffer layer as n type material, the absorber layer as p type material Most of the PV cell has been base on the conjugated polymers such as PANi and PTh due to their exceptional electrical characteristic, thermal and environmental stability, solubility [6,7,8]. Cadmium sulfide QDS are easy to synthesize having direct band gap of 2.4 eV at room temperature making it efficient in the visible region The structure of conjugated polymers on side chains has played the important role of enhancement in absorption, photoconductivity and charge carrier motilities [9]. In this work, we planned to investigate the optical properties of PTh-co-PANi-SiO₂ composites.

EXPERIMENTAL

Thiophene, aniline and titanium chloride (TiCl₄) purchased and from SD fine, India. AR grade were used as opening chemicals, without further purification. The random copolymer of PTh-co-PANI was synthesized by taking ratio of 1:1 molar ratio of aniline, thiophene. Monomer solution and Silicon dioxide of was added in beaker under rigorous magnetic stirring. As soon as TiCl₄ in that solution, the polymerization reaction starts with the change in the colour of PTh and PANi solution instantly and therefore the solution became brown black and Drying for 24 hour.

RESULT AND DISCUSSION

FESEM Analysis

The topographical picture of samples were obtained by using FE-SEM. Figure 1 represents FE-SEM images of of PTh-co-PANi-SiO₂ composite. FE-SEM analysis reveals that the composite acquire pital and

spongy morphology with specific smooth boundaries. Overall, composites have smooth surface morphology. It can be observed from that Ti and graphene cluster is spreaded over the surface in morphological nature.

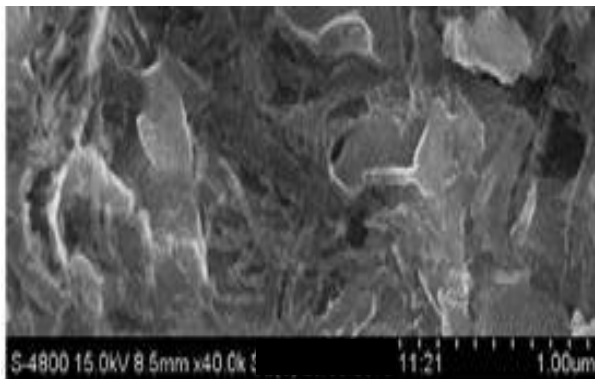


Figure FESEM image of PTh-co-PANi-SiO₂ copolymer

UV-Vis analysis

Figure 2 shows the UV-vis spectra of the as-prepared PTh-co-PANi-SiO₂ composite of in the range 190 nm to 2000 nm. PTh-co-PANi-SiO₂ composite was found intensive and broad absorption bands in the UV region, that indicating $\pi-\pi^*$ polymer backbone and SiO₂ matrix [10]. The absorption spectrums show a broad absorption over the wavelength ranging from 200-230 nm. Beyond 250 nm, constantly transmission smoothly up to 350 nm [11]. However, the absorption at 350 nm increases gradually with an increase in Ti and SiO₂ content present in polymer matrix [12].

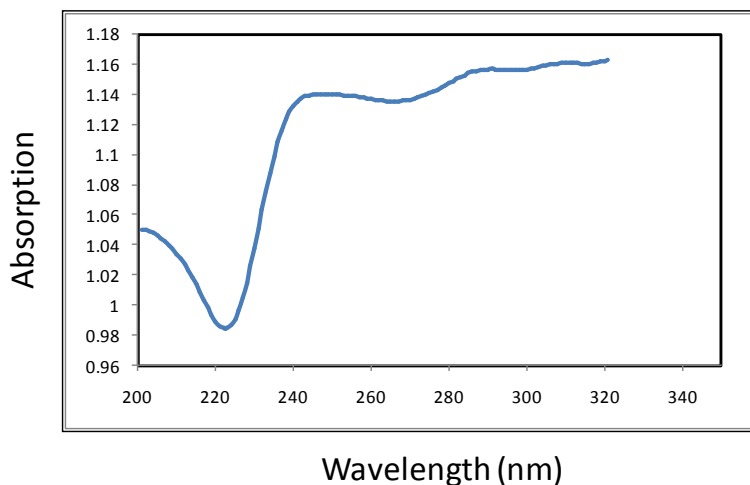


Figure 2. UV visible spectra of PTh-co-PANi-SiO₂ copolymer

Figure 3 shows the plot between $\alpha h\nu$ versus energy $h\nu$ for PTh-co-PANi-SiO₂ composite. By extrapolating the straightline to linear portion, the optical band gap value was found to be 3.85 eV (450 nm) calculated from The relation between absorption coefficient (α) and incident photon energy ($h\nu$) can be expressed as Eq. (1).. The optical band gap of sample lies in visible region, which is preferred for electronic application [9].

$$\alpha = A\left(\frac{h\nu - E_g}{h\nu}\right) \tag{1}$$

Where A is constant and E_g is the band gap of the material. The exponent 'n' depends on the type of the transition [10].

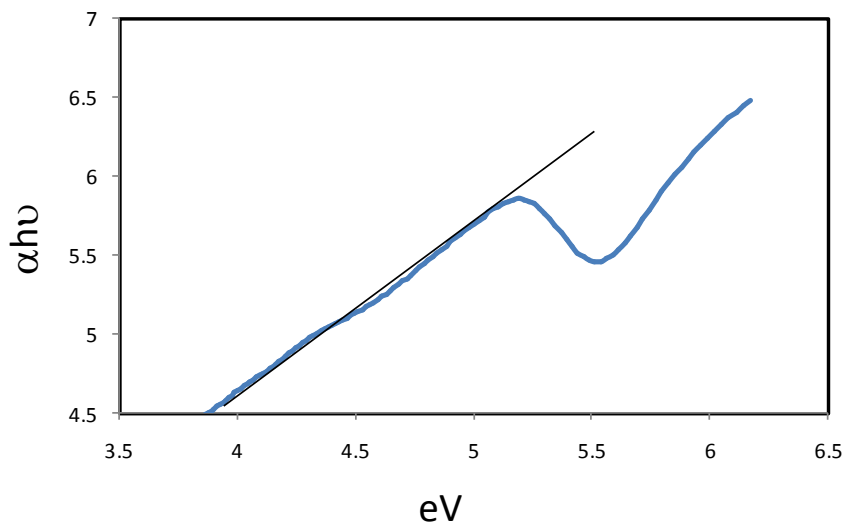


Figure 3 Band gap of PTh-co-PANi-SiO₂ copolymer composite

CONCLUSIONS

In the paper, we successfully synthesized copolymer composite of PTh, PANi and graphene. The optical band gap was found to be 3.85 eV of as synthesized PTh-co-PANi-SiO₂. The surface morphology of PTh-co-PANi-SiO₂ shows smooth and pital like structure.

REFERENCES

- [1] S.R. Takpire, S.A. Waghuley, *J. Electron. Mater.*, **44**, 1–6 (2015).
- [2] Y. Wang, X. Sua, S. Lua, *J. Mater. Chem.*, **22**, 1969–1976 (2012).
- [3] P. Xu, Q. Tang, H. Chen, B. He, *Electrochim. Acta*, **125**, 163–169 (2014).
- [4] S.R. Takpire a, S.A. Waghuley, 90 (2017) 44-50.
- [5] S.R. Takpire, K.R. Nemade, S.A. Waghuley, *Materials and Design* 101 (2016) 294–300
- [6] A. Haldar, S. Maity, N.B. Manik, *Ionics*, **14**, 427–435 (2008).
- [7] X. Lia, G. Wanga, X. Lib, D. Lu, *Appl. Surf. Sci.*, **229**, 395–401 (2004).
- [8] L. Zhang, M. Wan, *J. Phys. Chem. B*, **107**, 6748–6753 (2003).
- [9] M. Alama, A.A. Ansarib, M.R. Shaik, N.M. Alandis, *Arabian J. Chem.*, **6**, 341–345 (2013).
- [10] G. Wang, W. Xing, S. Zhuo, *Electrochim. Acta.*, **66**, 151–157 (2012).
- [11] Z. Han, J. Zhang, X. Yang, H. Zhua, W. Cao, *Sol. Energy Mater. Sol. Cells*, **94**, 755–60 (2010).
- [12] Sanjay R. Takpire, Sandeep A. Waghuley, *Optical and thermal properties of PTh-co-PANI-Ti St. Petersburg Polytechnical University Journal: Physics and Mathematics* 1 (2015) 417–423.



SURFACE ELECTRICAL STUDY OF GRAPHENE SYNTHESIZED BY ELECTROLYSIS METHOD

S. S. Gore^{1*} and S. K. Devade²

¹Department of Physics, R.A.College, Washim, Maharashtra 444505, India.

²Department of Physics, ShankarlalKhandelwal Arts, Science and Commerce College, Akola, Maharashtra, India

*Corresponding author email: sandipgore1@gmail.com.

ABSTRACT :

Presently, Graphene is a potential candidate in materials science, which found wide range of applications as flexible electric/photronics circuits, photovoltaic cell, supercapacitor, sensor etc. Therefore, through this paper we made an attempt to study surface electrical properties of materials. In the present work, Graphene was synthesized by simple electrolysis method. The as prepared Graphene was characterized X-Ray Diffraction (XRD) study. Similarly, the surface electrical study of Graphene executed using fore probe method.

KEYWORDS : Surface Electrical Study, Graphene, Electrolysis.

1. INTRODUCTION

Graphene is made up of pure carbon. It is a material in which the carbon atoms are arranged in a single layer like honeycomb pattern. Graphene was discovered in 2003 by Andre Geim and Kostya Novoselov at The University of Manchester, and results were published in 2004 [1, 2]. The structure of graphite was solved in 1916 by the related method of powder diffraction. It was studied in detail by V. Kohlschütter and P. Haenni in 1918, who also described the properties of graphite oxide paper. Its structure was determined from single-crystal diffraction in 1924 [3]. The graphite has a hexagonal layered arrangement of carbon atoms in the crystal structure. A 2D monolayer of sp² hybridised carbon atoms arranged in a honeycomb lattice structure has sparked global interest in many disciplines due to its exotic and superior physical properties that were not previously observed at the nanoscale [4, 5].

Graphene and Graphene oxide (GO) is great interest due to its low cost, easy access, and widespread ability to convert to graphene. Graphene offers extremely high carrier mobility, high carrier density, and has low intrinsic noise thereby providing a high signal-to-noise ratio for the better detection. Graphene is made up from oxidize graphite which is available in large amount. It has huge attention because of activities of GO [6]. The nanomaterials used in modified cement system can be classified according to their shapes in the space into zero-dimensional (0D) particles, one-dimensional (1D) fibres and two-dimensional (2D) sheets [7]. At present, a conventionally-modified Hummers method is the primary method for preparing GO. Graphite is commonly chosen as the starting material due to its availability and low cost. the expanded graphite is exfoliated into multi-layered or even single-layered sheets. GO structures is a critical factor in opening up band gaps comparable to those of silicon (1eV) for applications in electronics and photonics [8].

2. EXPERIMENTAL

There are many synthesis methods are available in which we use here electrolysis. Graphene is synthesized according to electrolysis method by using Graphite rod, Copper rod, dimmerstat for controlling voltage. First of all by taking 100 ml of distilled water in a beaker and then 5ml of HCL are added in it. Then

we got a solution. After that one copper rod and one graphite rod dipped well inside it. Now by using dimmerstat the negative end of the dimmerstat is attached to copper rod and positive end of the dimmerstat is attached to graphite rod by using diode. After this arrangement by switching on the dimmerstat we adjusted the voltage is at 10 V so that the constant voltage of 1 volt is providing to our arrangement. Now this process of electrolysis start. Now by observing the experiment it was shown to us that the small particles from graphite rod are remove and deposited at the bottom of beaker. This process is completed after two days. After two days the solution is completely disappearing and the graphene powder was formed into that beaker. Now this powder is washed by using filter paper. After that this powder is placed into the oven for 12 hours for drying.

2.1 Conductivity by Four probe experiment

Many conventional methods for measuring resistivity are unsatisfactory for semiconductors because metal –semiconductor contacts are usually rectifying in nature. Also, there is generally minority carrier injection by one of the currents carrying contacts. An excess concentration of minority carrier will affect the potential of other contacts and modulate the resistance of the material.

The method described here overcomes the difficulties mentioned above and also offers several other advantages. It permits measurements of resistivity in samples having a wide variety of shapes, including the resistivity of small volumes within bigger pieces of semiconductor. In this manner the resistivity of both side of p-n junction can be determined with good accuracy before the materials cut into bars for making devices.

Figure 1 shows the four-probe set-up used in this work for electrical study. In this setup, four sharp probes placed on a flat surface of the material to be measured, current is pass through the two outer electrodes, and the floating potential is measured across the inner pair. If the flat surface on which the probes rest is adequately large and the crystal is big the semiconductor may be considered to be a semi-infinite volume. To prevent minority carrier injection and make good contacts, the surface on which the probes rest, maybe mechanically lapped.



Figure 1. Four probe set-up.

3. RESULTS AND DISCUSSION

3.1 XRD analysis

Figure 2 show the XRD patterns of graphene. In XRD pattern of grapheme show one prominent and broad peaks (002) which is main characteristic peaks of graphene. All the peaks exactly match with JCPDS Data Card No. 41-1449 [9].

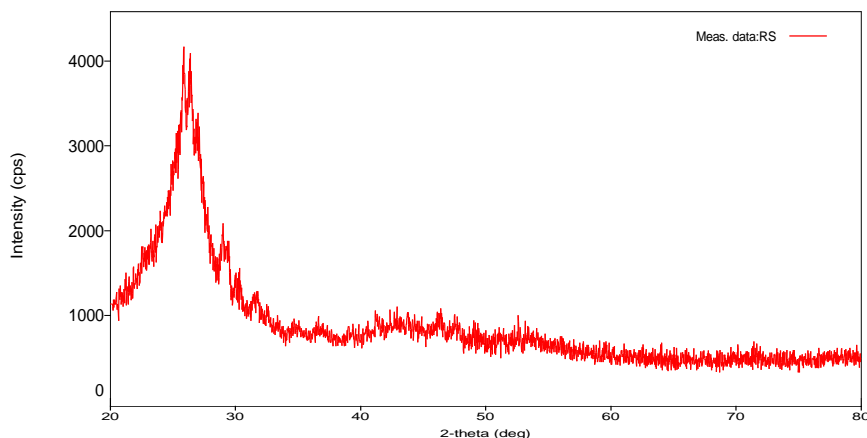


Figure 2. XRD pattern of Graphene.

3.2 Conductivity by Four Probe Method

The conductivity of material was measured on OMEGA four probe method instruments. By keeping constant current ($I=2\text{mA}$) and varying temperature, $S=0.2\text{cm}$ (Distance between two probes) and $W=0.75\text{cm}$ (Thickness of materials). Figure 3 depicts that the conductivity suddenly rises at 90°C .

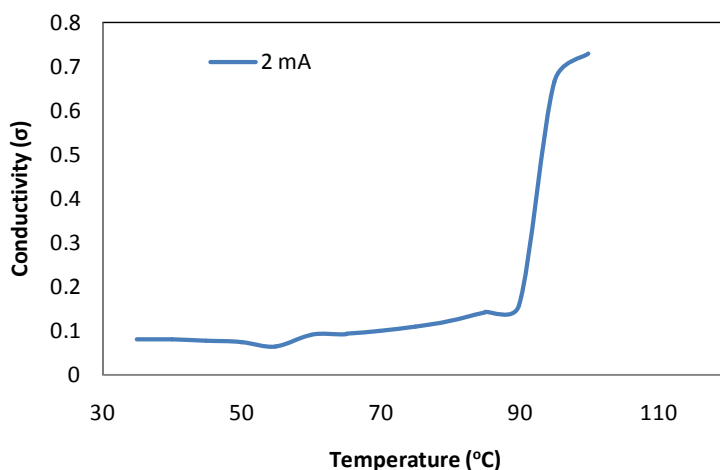


Figure 3. Conductivity plot of graphene as a function of temperature.

ACKNOWLEDGMENTS

Authors are very much thankful to Head, Department of Physics SantGadge Baba Amravati University, Amravati, India for providing necessary facilities

CONCLUSIONS

Present research has resulted in several novel and significant findings by getting knowledge of the graphene conductivity as well as materials literature. This report was mainly devoted on synthesis of graphene by electrolysis method. The synthesis of graphene is done by using electrolysis method. The obtained nanoparticles were used for characterizations and study the conductivity. The conductivity of graphene is high.

REFERENCES

- [1] S. J. Woltornist, A. J. Oyer, J. Y. Carrillo, A. V. Dobrynin, D. H. Adamson. American Chemical Society, 30 (2016)1-5.

-
- [2] H. C. Lee, W.Liu, S. Chai, A. R. Mohamed, A. A. Khe, N. M. S. Hidayaha, U. Hashim, RSC Adv., 7(2017) 15644-15693.
- [3] www.graphene.manchester.ac.uk. "The Story of Graphene". The University of Manchester. 10 September 2014. Retrieved 9 October 2014.
- [4] J. Zhao, H. Zeng ACS Omega 2 (2017) 171-180.
- [5] M. J. Allen, V. C. Tung, R. Kaner, Chemical Reviews, 110 (2009) 132-45.
- [6] P. T. Yin, T. Kim, J. C. Bum Lee, Chem. Phys., 15 (2013) 12785-12799.
- [7] V. V. Pokropivny, V. V. Skorokhod, Mater SciEng, C. 27 (2007) 990–993.
- [8] S. N. Alam, N. Sharma, L. Kumar, Graphene, 6 (2017) 1-18.
- [9] K.R. Nemade, S.A. Waghuley, Solid State Sciences 22 (2013) 27-32.



STUDY OF USEFUL AND IMPORTANT-ASPECTS OF THE NATURAL RESOURCES

M. N. Waghmare and K. S. Junne
Department of Physics, S.A.S. College Mukhed.
Email ID – prof.waghmaremn@gmail.com

ABSTRACT :

The present paper gives the study of all aspects of natural resources and all types of natural resources are systematically studied.

1) INTRODUCTION.

The environment provides us with a variety of goods and services necessary for our day-to-day life. These natural resources include air, water, soil and minerals, along with the climate and solar energy, which form the non-living or abiotic parts of nature. The biotic or living parts consist of plants and animals, including microbes. Plants and animals can only survive as communities of different organisms, all closely linked to each other in their own habitat, and requiring specific abiotic conditions. Thus, forests, grasslands, deserts, mountains, rivers, lakes and the marine environment all form habitats for specialised communities of plants and animals to live in. The interaction between the abiotic aspects of nature and specific living organisms together form ecosystems of various types. Many of these living organisms are used as food resources.

The natural resources refer to the things that exist freely in nature for human use and do not necessarily need the action of mankind for their generation or production. The key aspect of natural resources is that they support the survival of humans and other life forms on earth. These resources include land, rocks, forest (vegetation), water (Lakes, Seas and Rivers), fossil fuel, animals (fish, wild life, and domesticated animals), minerals, sunlight and air. The natural resources are useful raw materials that we get from the Earth. They occur naturally, which means that humans cannot make natural resources. Instead, we use and modify natural resources in ways that are beneficial to us. The materials used in human-made objects are natural resources. Some examples of natural resources and the ways we can use them.

2) RESULT AND DISCUSSION :

Types of Natural Resources

Renewable and non-renewable natural resources

Renewable natural resources:

Renewable resources are the ones that are consistently available regardless of their use. They can be fairly recovered or replaced after utilization. Examples include vegetation, water, and air. Animals can also be categorized as renewable resources because they can substitute the older animals.

Non-renewable natural resources :

Non-renewable resources are the ones that cannot simply be substituted or recovered once they have been utilized or destroyed. Examples of such natural resources include fossil fuels and minerals. Minerals are categorized as non-renewable because, even though they take shape naturally through the rock cycle, their formation periods take thousands of years.

Biotic and Abiotic Natural Resources

Biotic natural resources :

The Biotic natural resources are the ones that come from the organic and living materials. These include resources such as animals, forests (vegetation), and other materials obtainable from them. Fossil fuels such as petroleum, oil, and coal are also included in their grouping because they are generated from decayed organic matter.

Abiotic natural resources :

The abiotic natural resources are the ones that come from non-organic and non-living materials. Examples of abiotic natural resources are water, air and heavy metals like iron, copper, silver, gold etc.

Stock Natural Resources

Stock natural resources are those that are present in the environment but it the necessary expertise or technology to have them exploited. Hydrogen is an example of a stock natural resource.

Important Natural Resources in the World

Water:

The earth may be mostly water, only about 71% of it is fresh water. Of that 2.5% even less is considered to be potable. Potable water is water that is considered to be safe to drink and cook with. While many countries are working to build water treatment plants, the fact is that due to changes in the climate the amount of rain and ice melts from winter have dropped off and lowered the reserve supplies of freshwater to be treated. There are initiatives to educate and regulate the use of water in the world, as well as exploration into the technology of water farming in arid countries too.

Air :

Clean air is necessary for the existence of life on this planet. It is essential for the existence of plants, animals and wildlife. It is important to reduce air pollution as polluted air degrades the environment and can enter our body and can cause health related problems. There are number of ways to keep the air clean and reduce air pollution like riding bus instead of using your own vehicle, carpooling etc. Read here more about causes and effects of air pollution.

Coal :

Coal is estimated to be able to last less than 200 more years. One of the issues is that as countries such as China increase their demands on the coal supply it will dwindle faster Coal is also the major source of air pollutant in the world so there is much discussion about regulating its usage. The problem is it is one of the cheapest sources of fuel for industrial applications.

Oil :

The general estimate is that with the projected rate of consumption of oil supplies and known resources that there is enough to last for 30-40 more years. While many in the oil industry are pushing to be allowed to frack and drill in protected areas to look for undiscovered oil fields, little has been done to address the question of what will happen to the Earth's crust when the fields are empty and there are large empty cavities beneath the Earth . Even if new fields and methods of oil extraction are discovered, geologists project that it would be impossible for the Earth to have an unlimited supply of oil. It takes millions of years for oil to be created; there is no way of speeding up that process.

Natural gas:

Natural gas reserves are doing only slightly better than oil, it is estimated that there is enough to last for 60 years. Gas is a much cleaner fuel source than oil, which has led to an increased level of consumption of it as an alternative fuel. But it still stands to run out quickly.

Phosphorus :

Phosphorus comes from phosphate rock and is used to grow all of our food and crops. Unfortunately, phosphate rock is only found in three places on Earth –the US, China and Morocco. The projected lifespan of the current known resources is about a 100 years. There has not been significant research in developing new and safe fertilizers that can be effective replacements for phosphorus.

Minerals :

Mineral like gypsum, bauxite, phosphate, bentonite, mica, titanium, zirconium are found in sea beds along the coastal plains. Rare earth elements like scandium and terbium are two of the earth powerful minerals that are used in wind turbines and electronic circuits in smartphones. Coastal plains contains deposits of potassium carbonate and rare elements like cerium and neodymium.

Iron :

Iron is also in limited supply. It is made from elements such as silica which then have to be heated to create the pig iron that industrialization depends on. Iron was the most important natural resource on earth during ancient ages. It allowed people at that time to build stronger weapons, better transportation and taller buildings. Both iron and steel are still used in modern day industries.

Soil :

Another important natural resource is soil. Soil is composed of many different particles and nutrients in the soil helps plants grow. Apart from this, soil can also be used to provide shelter. A pile of garbage along with some soil when placed in worm compostbin, creates nutrient rich soil that helps in growth of plants and makes them healthy.

Forests and Timber :

As the world gets more modern and population grows, there is more of a demand for housing and construction projects. This reduces open green spaces. Forests are necessary to preserve the ecology of the world that supports all of the natural resources and life. Forests also play a critical role in providing clean air and the lumber that builds the homes.

CONCLUSION :

The discussed study of natural resources existing freely in nature, they are analysed and how they are useful to the survival of human being. All types of the natural resources how they are recovered and utilized in the present form. The resources like, coal, oil, natural gas and some minerals are studied.

REFERENCES :

- 1) Text book of Environmental Studies for undergraduate courses Second edition.
- Erach Bharucha, Pune 2013.
- 2) A Text book of Environmental Science and Technology – M. Anji Reddy.
- 3) Text book of Environmental Studies. – G.R. Chatwal, Harish Sharma.
- 4) What is Natural Resources, Definition and Meaning, Investorwords.com 2016-12-12.
- 5) Definition of Natural resources – Worldcentral.com.2016-12-12.
- 6) Earth's natural health : an audit, science.org.au may 23, 2007.
- 7) Natural resources – Oxford Dic. 2014-04-20.



SYNTHESIS AND CHARACTERIZATION OF ELECTRODEPOSITED Sb_2Se_3 THIN FILMS FOR VARIOUS CONCENTRATION**P. M. Kulal**

Department of Physics, Shivaji College Renapur (MH), India

* Corresponding author. E-mail address: pmkulal@gmail.com, Tel.: 7798032739

ABSTRACT :

In present investigation, we have successfully prepared polycrystalline Sb_2Se_3 thin films by single step electrochemical synthesis. Effect of concentrations of precursor solution on structural, morphological, optical and wettability properties by means of X-ray diffraction (XRD), scanning electron microscopy (SEM), optical absorption and contact angle measurement have been investigated. It is evident from XRD pattern that Sb_2Se_3 thin films are polycrystalline and has orthorhombic crystal structure. Also as precursor concentration increases the diffraction peak intensity also increases. Scanning electron micrographs reveals that the increase in precursor concentration causes the formation of soap foam like microstructure which is spread in the form of ellipsoids over whole substrate surface. The optical band gap increases from 1.97 to 2.03 eV and contact angle decreases from 40° to 13° i.e. the surface of Sb_2Se_3 thin films converts from hydrophilic to superhydrophilic nature due to increase in precursor concentration. In addition the holographic interferometric properties have been studied. The thickness, stress to substrate and deposited mass of the thin films is determined using Double Exposure Holographic Interferometry (DEHI) technique.

KEYWORDS: Single step electrosynthesis, Polycrystalline Sb_2Se_3 , Soap foam, Holograms.**1. INTRODUCTION**

In recent years considerable interest has been shown in the synthesis of thin semiconductor films by electrochemical and chemical deposition of colloidal semiconductor. Thin semiconducting films synthesized by electrochemical and chemical deposition methods are quite attractive for designing systems for electro-optics and photoelectrochemical (PEC) solar cells. These cells are simple in construction and have the advantages that they can be used for both photovoltaic and chemical energy conversions.

Recently considerable attention has been given to the preparation and characterization of thin metal chalcogenide films by various techniques Pulsed laser deposited [1], antimony Selenide via chemical bath deposition [2, 3], by electrodeposition method [4,5], by spray pyrolysis technique [6], by silar method [7] Among various Selenides, antimony triselenide finds some special applications as target material of lithium-ion batteries [1], photovoltaic cells [5, 6].

The double exposure holographic interferometry technique has been widely accepted as a viable tool for non-destructive testing of materials. This technique is sufficient to form a permanent record of relative surface displacement of object occurring after a fixed interval of time. As a result, the DEHI technique can be applied to many engineering problems, especially, continuous comparison of the surface displacement relative to an initial position [8]. The technique has been successfully employed to study the surface deformation of stainless steel with Ti–Ba–Ca–Cu thin film deposition [9].

In present work, we report on single step electrosynthesis of polycrystalline Sb_2Se_3 thin films. Effect of concentrations of precursor solution on structural, morphological, optical and wettability properties have

been investigated. In addition the holographic interferometric properties have been studied. The thickness and stress of the films have been determined by DEHI technique for various concentrations.

2. EXPERIMENTAL

2.1 Preparation of Sb_2Se_3 thin film

The electrodeposition of Sb_2Se_3 thin films was carried out from an electrolyte bath consisting of potassium antimony tartarate and selenium dioxide aqueous solutions. All solutions were prepared immediately prior to each experiment by dissolving the requisite amounts of analytical reagent grade salts in double distilled water. The concentration of the antimony precursor solution was varied from 0.05 to 0.1 M at an interval of 0.025 M by changing the amount of potassium antimony tertarate dissolved in double distilled water. The pH of the bath was maintained to ~ 3 . The metal substrates were mirror polished with zero grade polish paper, cleaned with detergent and finally cleaned ultrasonically. A graphite plate was used as a counter electrode. All the potentials were measured with respect to SCE. The cathode to anode distance was 0.5 cm. The bath was kept unstirred. Electrodeposition was carried out potentiostatically using a constant voltage source. The deposition conditions were optimized to get good quality Sb_2Se_3 films of maximum thickness. The prepared Sb_2Se_3 films were found to be well adherent uniform and grayish in color.

The Sb_2Se_3 thin films were analyzed by X-ray diffraction within the range $10-100^\circ$ on computer controlled Philips PW-3710 using CrK_α radiations ($\lambda=2.2897 \text{ \AA}$) to determine the film structures. Microstructural study was carried out using scanning electron microscopy (SEM-JEOL 6360). The optical absorption study was carried out over the wavelength range 350-850 nm using Systronics spectrophotometer-119, with FTO substrate as a reference. In order to study interaction between water and Sb_2Se_3 film surface contact angle measurement was carried out by Rame-hart USA equipment with CCD camera.

2.2. Double exposure holographic interferometry (DEHI) technique

Holograms are recorded using double exposure holographic interferometry technique. The holograms were recorded by conventional two beam off-axis technique using 10 mW He-Ne laser having wavelength $\lambda= 6328 \text{ \AA}$. The holograms were recorded on the holographic film (Kodak 8E 75 HD) before and after the deposition of Bi_2Se_3 thin films. The reconstructed image of substrate was observed with the reference beam which shows the localized fringes.

2.3. Measurement of thickness of the thin films and stress to the substrate

The simple non-destructive technique, for the quantitative measurement of stress in thin films by the use of DEHI technique is reported by [10]. While recording the hologram, if the object is illuminated with a beam of light making an angle θ_1 with the normal and is viewed at an angle θ_2 during reconstruction, the reconstructed image has a superimposed fringe pattern corresponding to a displacement of the surface. The displacement in the normal direction is given by

1

$$d = \frac{n\lambda}{\cos \theta_1 + \cos \theta_2}$$

Where n is the number of fringes and λ is the wavelength of light. In general θ_1 and θ_2 are sufficiently small, so that

$$d = \frac{n\lambda}{2}$$

The stress to the stainless substrate is given by the formula [11].

$$s = \frac{t_s^2 Y_s \Delta}{3l^2 t_f}$$

Where, S is stress in dyne/cm², t_s is substrate thickness, t_f is film thickness, Δ is deflection of the substrate equal to $4\lambda/2$, Y_s is Young's modulus, l is length of the substrate on which the film is deposited. The mass of the deposited film was calculated using the relation

Mass = density x volume

3. RESULTS AND DISCUSSION

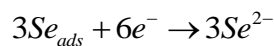
3.1 Film formation and reaction mechanism

Electrodeposition of Sb_2Se_3 was carried out from aqueous acidic bath. The Sb_2Se_3 films were cathodically deposited from an aqueous solution containing antimony and selenium ions. The electrodeposition of Sb_2Se_3 had been carried out from an aqueous acidic solution containing antimony and selenium ions.

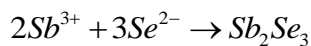


Se^{2+} is converted into Se_{ads} .

The electron reacts with Se_{ads} .



A complex of Sb^{3+} reacts with Se^{2-} to give



3.2 Structural studies

Fig. 1 (a-c) shows the XRD patterns of Sb_2Se_3 thin films deposited for three different concentrations 0.05, 0.075 and 0.1 M respectively. With increasing the concentration of precursor solution, increase in film thickness was observed. This may be due to sufficient reaction time period available for the formation of oriented growth of Sb_2Se_3 thin films along specific plane. It is evident from XRD pattern that Sb_2Se_3 thin films are polycrystalline and has orthorhombic crystal structure. Similar type of results has been reported elsewhere [5, 12]. The XRD pattern indicates the presence of (130), (520), (440), (212), (351), (061) and (370) planes of Sb_2Se_3 materials which is in good agreement with JCPDS cards no. 01-075-1462. It should be noted that the relative peak intensity of the diffraction arising from all the peaks increases with increase in concentration of precursor solution. The average grain size was estimated using Scherrer's formula

$$D = \frac{0.9\lambda}{\beta \cos\theta} \quad (4)$$

where, β is the broadening of diffraction line measured at half maximum intensity (radians) and $\lambda = 2.2897 \text{ \AA}$ is the wavelength of the Cr $K\alpha$ X-ray. The average grain size was found to be 24 nm. The diffraction peaks marked by * are due to selenium.

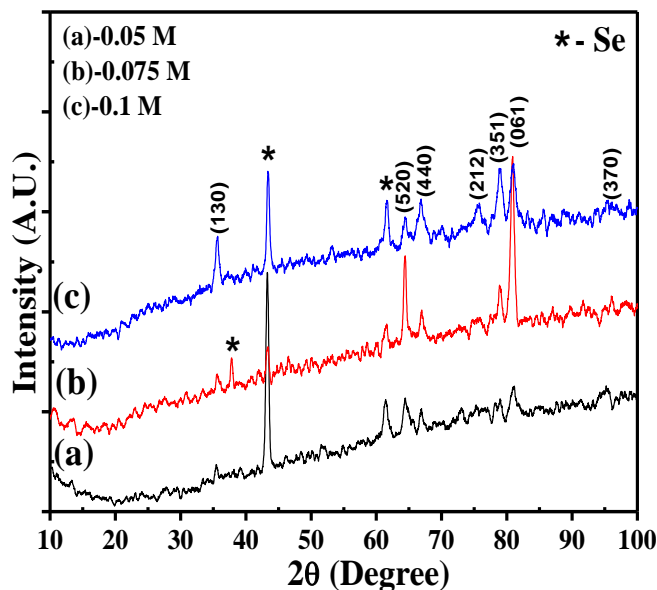


Fig.1 The X-ray diffraction patterns of Sb_2Se_3 thin films for three different precursor concentrations: (a) 0.05 M, (b) 0.075 M and (c) 0.1 M.

3.3 Surface morphological studies

The surface morphologies of the Sb_2Se_3 thin films for different concentrations of precursor solution were shown in Fig. 2 (a-c) at $\times 10,000$ magnification. Appeared surface morphology for 0.05 M concentration suggest a uniform growth of first few layers of Sb_2Se_3 nanocrystallites and as the growth proceeds agglomeration of grains took place, giving non-uniformity in grain size on surface of the thin film (Fig. 2 a). However, the increase in precursor concentration to 0.075 M governs vertical growth of Sb_2Se_3 so as to form vertically patterned arrays of Sb_2Se_3 nanocrystallites (Fig. 2 b). In this case the surface of Sb_2Se_3 thin films rougher, porous and nanocrystallites are uniformly spread over the whole surface. Further, increase in precursor concentration to 0.1 M completely destroys the previously developed surface morphologies. Now the surface of Sb_2Se_3 thin films looks like soap foam which is spread in the form of ellipsoids over whole substrate surface as seen from Fig. 2 c. This morphological change is attributed may be due to the presence of excess antimony in atomic percentage [13].

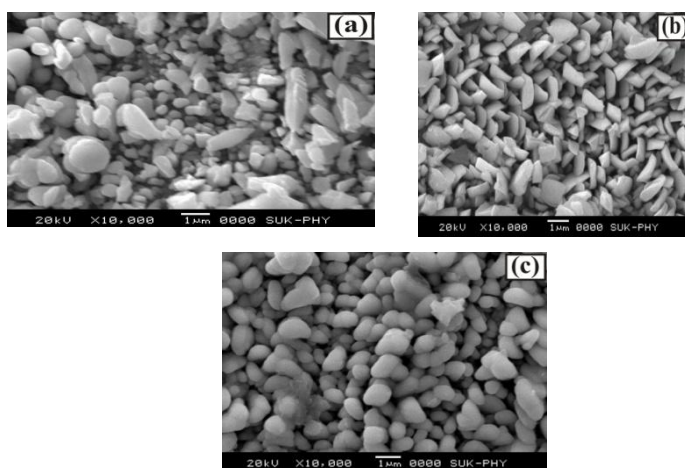


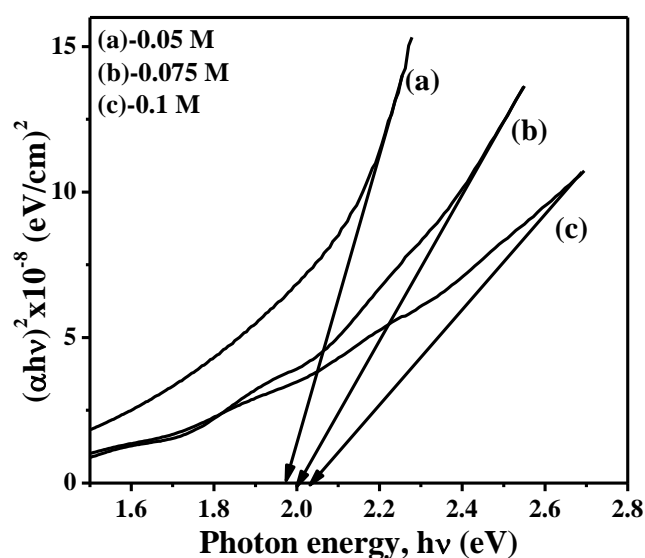
Fig.3 The variation of $(\alpha hu)^2$ with photon energy (hu) of Sb_2Se_3 thin films for three different precursor concentrations: (a) 0.05 M, (b) 0.075 M and (c) 0.1 M.

3.4 Optical studies

The variation of optical band gap of Sb_2Se_3 films for three different precursor concentrations is shown in inset of Fig. 3. This data was further used for analyzing optical direct band gap energy using following classical relation for near edge optical absorption in semiconductor. The theory of optical absorption gives the relationship between the absorption coefficient α and the photon energy ' $h\nu$ ' can be written as,

$$\alpha = \frac{A(E_g - h\nu)^n}{h\nu} \quad (5)$$

where, ' α ' is the absorption coefficient, ' A_0 ' is a constant, ' E_g ' is the band gap, and ' n ' is equal to 1/2 for a direct and 2 for indirect transition. Fig. 3 shows the plots of $(\alpha h\nu)^2$ versus $h\nu$ plotted for estimating the values of direct band gap energy of Sb_2Se_3 films by extrapolating curves to zero absorption coefficient. The band gap energy (E_g) values are found to be 1.97, 2.0 and 2.03 eV for 0.05, 0.075 and 0.1 M precursor concentrations, respectively, which is comparable to reported earlier [5]. The increase in direct band gap energy (1.98–2.1 eV) with increase in film thickness is confirmed. Similar type of results has been reported by Kale et al and Pathan et al for CdTe and MnS by using SILAR method respectively [14,15].



3.5 Wettability Test

Wettability test is carried out in order to investigate the interaction between liquid and Sb_2Se_3 thin films. If the wettability is high, contact angle (θ), will be small and the surface is hydrophilic. On the contrary, if the wettability is low, θ will be large and the surface is hydrophobic. A contact angle of 0° means complete wetting and a contact angle of 180° corresponds to complete non-wetting. Both super-hydrophilic and super-hydrophobic surfaces are important for practical applications [16]. From Fig. 4 we observed that, the Sb_2Se_3 thin films are hydrophilic as water contact angle is 40° (less than 90°) means high wettability. As the concentration of precursor solution increases the water contact angle decreases. The contact angles for 0.075 and 0.1 M concentration was found to be 25° and 13° . This may be due to the strong cohesive force between the water droplet and hydroxide present in the Sb_2Se_3 compound. Similar type of behavior has been reported by More et al [17] for chemically deposited TiO_2 thin films. Thus as concentrations of precursor solution increases the surface of Sb_2Se_3 thin films converts from hydrophilic to superhydrophilic nature. This specific property is attributed to nanocrystalline nature that is expected to possess very high surface energy. Due to which the water is attracted rather repelled by the Sb_2Se_3 film. This specific property

is useful for making intimate contact of aqueous electrolyte with electrode surface in photoelectrochemical cell.

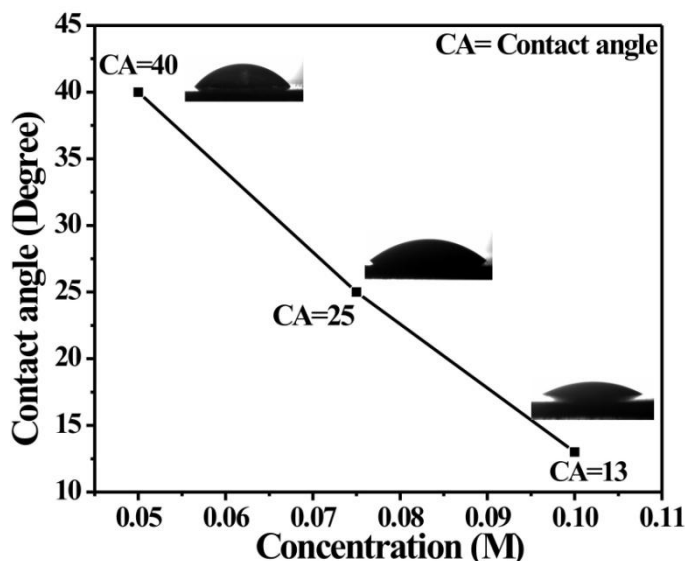


Fig.4 Contact angles of Sb_2Se_3 thin films for three different precursor concentrations: (a) 0.05 M, (b) 0.075 M and (c) 0.1 M.

3.6. Double exposure holographic interferometry

The actual experimental of double exposure holographic interferometry technique is shown in fig. 5. The recorded holograms of Bi_2Se_3 thin films deposited onto stainless steel substrate at different deposition times are shown in Fig.6 from the hologram study, From the fig 7, it is observed that as the bath concentration increases, the number of fringes localized on the surface of stainless steel substrate goes on increasing [18]. From the Fig.8, Fig.9 and Fig. 10 it is observed that thickness increases, deposited mass increases and stress to the substrate decreases with increasing bath concentration respectively as shown in Table 1. Janseen et al reported that decrease in CrN thin film stress with thickness [19]. This may be due to scattering or interference of incident light.

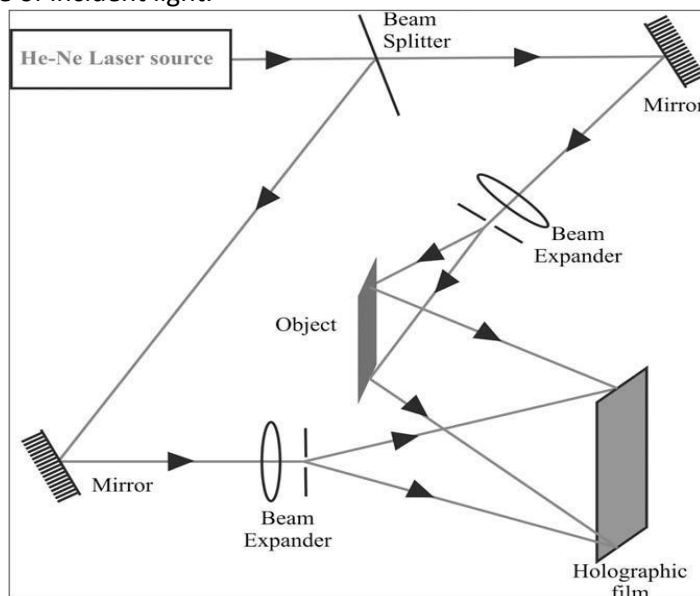


Fig.5 Actual experimental set up of the double exposure holographic interferometry technique

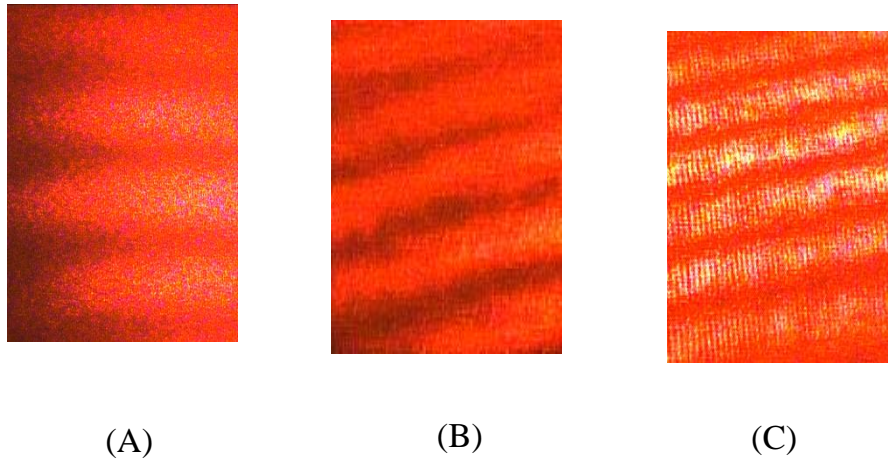


Fig. 6 Recorded holograms of Sb_2Se_3 thin films at different concentration (a) 0.05 M, (b) 0.075 M and (c) 0.1 M.

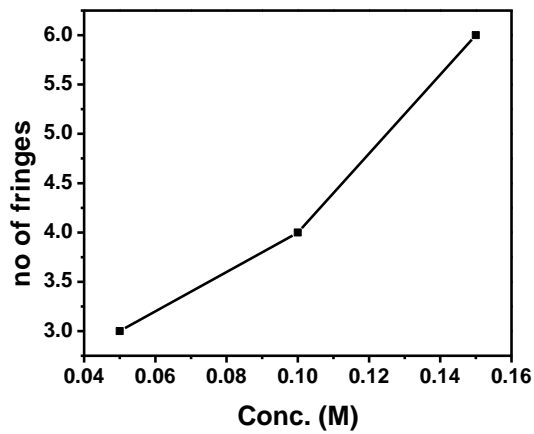


Fig.7 No. of fringes with at different concentration (a) 0.05 M, (b) 0.075 M and (c) 0.1 M

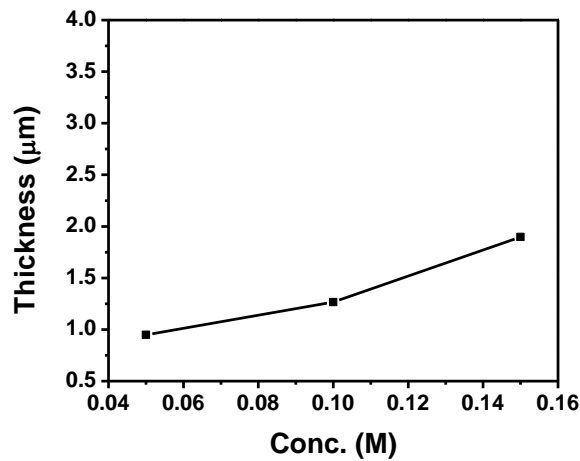


Fig.8 The variation of Sb_2Se_3 film thickness with at different concentration (a) 0.05 M, (b) 0.075 M and (c) 0.1 M

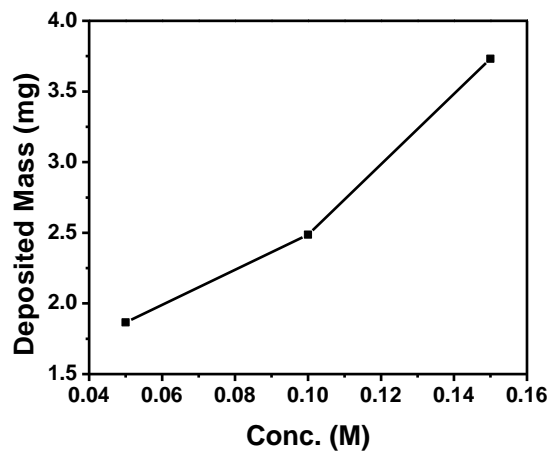


Fig. 9 The variation of Sb_2Se_3 film deposited mass at different concentration (a) 0.05 M, (b) 0.075 M and (c) 0.1 M.

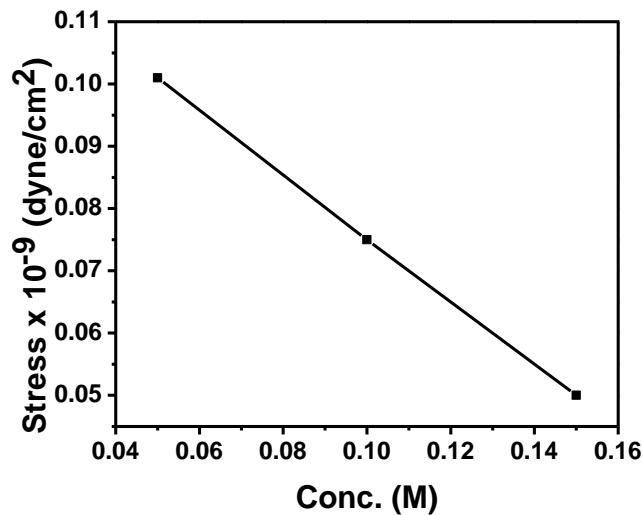


Fig.10 The variation of Sb_2Se_3 film stress to substrate with at different concentration (a) 0.05 M, (b) 0.075 M and (c) 0.1 M.

Table 1 The observed number of fringes, thickness, stress to the substrate and mass deposited for various bath concentration

Conclusion

Bath conc. (M)	Deposition time(h)	Fringe numbers	Thickness of film (μm)	Mass deposited (mg)	Stress $\times 10^9$ (dyne/cm ²)
A= 0.05M	1	3	0.949	1.865	0.101
B= 0.075M	1	4	1.265	2.487	0.075
C= 0.1M	1	6	1.898	3.731	0.050

XRD pattern revealed that the Sb_2Se_3 films are polycrystalline and has orthorhombic crystal structure. Scanning electron micrograph of Sb_2Se_3 films clearly shows the formation bunch of cabbages at high magnification. The Sb_2Se_3 thin film shows direct band gap with energy 2.03 eV. Wettability test of Sb_2Se_3 thin films reveals hydrophilic nature with water contact angle 25° . The determination of thickness and stress of the Sb_2Se_3 thin film was carried out by Double Exposure Holographic Interferometry (DEHI) technique

REFERENCES

- [1] Ming-Zhe Xue, Zheng-Wen Fu, *Journal of Alloys and Compounds* 458 (2008) 351
- [2] Y. Rodríguez-Lazcano, Yolanda Pen˜a, M.T.S. Nair , P.K. Nair, *Thin Solid Films* 493 (2005) 77
- [3] C.D. Lokhandea, B.R. Sankapal, S.D. Saratale, H.M. Pathan, M. Giersig, V. Ganesan, *Applied Surface Science* 193 (2002) 1
- [4] A. P. Torane. C. H. Bhosale, *journal of physics and chemistry of solids*, 63 (2002) 1849
- [5] A. M. Fernandez, M.G. Merino, *Thin Solid Films* 366 (2000) 202
- [6] K. Y. Rajpure, C.H. Bhosale, *Materials Chemistry and Physics* 73 (2002) 6
- [7] C. D. Lokhande, B.R. Sankapal, R.S. Mane, H.M. Pathan, M. Muller, M. Giersig, V. Ganesan, *Applied Surface Science* 182 (2001) 413
- [8] M.B. Dongare, V.J. Fulari, R.N. Thokale, H.R. Kulkarni, *Asian Chem. Lett.* 3 (1999) 52.
- [9] R.N. Thokale, P.S. Patil, M.B. Dongare, *Mater. Chem. Phys.* 74 (2002) 143.
- [10] P.J. Magill, T. Young, *J. Vac. Sci. Technol.* 4 (1967) 47.
- [11] S.J. Pawar, P.P. Chikode, V.J. Fulari, M.B. Dongare, *Mater. Sci. Eng. B* 137 (2007) 23
- [12] C. D. Lokhande, B. R. Sankapal, R. S. Mane, H. M. Pathan, M. Muller, M. Giersig, V. Ganesan, *Appl. Surf. Sci.* 193 (2002) 1.
- [13] M. Ristic, S. Popovic, S. Music, *Mater. Lett.* 58 (2004) 2494.
- [14] S. S. Kale, R. S. Mane, H. M. Pathan, A. V. Shaikh, O. S. Joo, S. H. Han, *Appl. Surf. Sci.* 253 (2007) 4335.
- [15] H. M. Pathan, S. S. Kale, C. D. Lokhande, S. H. Han, O. S. Joo, *Mater. Res. Bull.* 42 (2007) 1565.
- [16] R. D. Sun, A. Nakajima, A. Fujushima, T. Watanabe, K. Hashimoto, *J. Phys. Chem. B* 105 (2001) 1984.
- [17] A. M. More, J. L. Gunjkar, C. D. Lokhande, R. S. Mane, S. H. Han, *Micron* 38 (2007) 500.
- [18] V. J. Fulari, V. P. Malekar, and S. A. Gangawane, *Progress In Electromagnetics Research C*,12 (2010) 53
- [19] G.C.A.M. Janseen, F.D. Tichelaar, C.C.G. Visser, *J. Appl. Phys.* 100 (2006) 093512



VISIBLE QUANTUM CUTTING & DOWN-CONVERSION IN $\text{CaF}_2:\text{Gd}^{3+}, \text{Eu}^{3+}$ PHOSPHOR

S. R. Jaiswal¹, P.A. Nagpure², V. B. Bhatkar², S. K. Omanwar³

¹Department of Physics, Shri R. L. T. College of Science, Akola. 444606(INDIA)

²Department of Physics, Shri Shivaji Science College, Amravati. 444601 (INDIA)

³Department of Physics, SantGadge Baba Amravati University, Amravati. 444602 (INDIA)

(Corresponding author: srjaiswal07@gmail.com)

ABSTRACT :

The conversion of vacuum ultraviolet (VUV) radiation to visible (VIS) light is described which makes it possible to obtain two VIS photons for each vacuum ultraviolet (VUV) photon absorbed. Often it is termed as Quantum Cutting (QC). The phenomenon also called as down conversion (DC), is demonstrated by $\text{CaF}_2:\text{Gd}^{3+}, \text{Eu}^{3+}$. We prepared $\text{CaF}_2:\text{Gd}^{3+}, \text{Eu}^{3+}$ phosphor synthesis via reactive atmosphere process. Powder X-ray diffraction analysis shows structural purity of as-synthesized phosphor. The emission and excitation spectra of $\text{CaF}_2:\text{Gd}^{3+}, \text{Eu}^{3+}$ were investigated using the VUV beam line of the Beijing Synchrotron Radiation Facility (BSRF), China. The energy transfer (ET) in calcium fluoride compound from the Gd^{3+} ions to Eu^{3+} through cross relaxation occurs. On the basis of the calculations from the emission spectra in the visible region obtained, we have obtained optimal quantum efficiency as high as 117% for red-emitting $\text{CaF}_2:\text{Gd}^{3+}, \text{Eu}^{3+}$ phosphor under excitation of 203 nm in reactive atmosphere process (RAP).

KEYWORDS: Reactive Atmosphere Process (RAP), Quantum cutting, VUV spectroscopy, Energy transfer, CaF_2 .

1. INTRODUCTION

For the development of mercury free fluorescent lamps and plasma display panels (PDPs), we require phosphor having quantum efficiency is greater than unity under VUV excitation. The phosphors having quantum efficiency is greater than unity are called quantum cutting phosphors. Quantum cutting provides a means to obtain two or more low energy photons for each high energy absorbed photon. Therefore it serves as a down converting (DC) mechanism with quantum efficiency greater than unity and it offers the prospect of providing enhanced energy effectiveness in lighting devices [1]. In order to obtain quantum-cutting phosphors with quantum efficiencies exceeding unity, the lanthanide ions are obvious candidates for this purpose due to their energy level structures that afford metastable levels from which quantum-splitting processes are capable. The inorganic calcium fluoride is one of the most important host with certain weird characteristics like wide band gap greater than 11 eV. Calcium fluoride with rare earth doped phosphor has conventional attention for numerous research works [3]. B. Herdenet *et al.* reported photon cascade emission in Pr^{3+} -doped fluorides with CaF_2 structure [4]. W. Binder *et al.* reported $\text{CaF}_2:\text{Sm}^{3+}$ Phosphor was used for the application of solid state laser materials [5]. A. Lucas discussed $\text{CaF}_2:\text{Dy}$ and $\text{CaF}_2:\text{Tm}$ phosphors are used for the application of dosimetry [6]. In our experiments we use gadolinium and europium lanthanides as a dopant in the host of CaF_2 for the application of quantum cutting. The process energy transfer and quantum cutting in $\text{CaF}_2:\text{Gd}^{3+}, \text{Eu}^{3+}$ can occur by the dopant combination of Gd^{3+} and Eu^{3+} , in which Gd^{3+} (acts as a sensitizer) and absorbing high energy VUV photon is cut into two visible photons emitted by two Eu^{3+} ions (acts as an activator).

2. EXPERIMENTAL

$\text{CaF}_2: \text{Gd}^{3+}, \text{Eu}^{3+}$ phosphor was synthesis via reactive atmospheric process. In this method we used metal carbonate like CaCO_3 (99.99% A.R.) as a precursor. The inorganic calcium carbonate was taken in Teflon beaker. A little amount of double distilled water was added in beaker and stirred it, then hydrofluoric acid (HF) added in it to get slurry. The slurry was dried by blowing air or heating on hot plate (80°C). A freshly prepared CaF_2 host was obtained. Gd_2O_3 (AR 99.9%) and Eu_2O_3 (AR 99.9%) were boiled in HNO_3 and evaporated to dryness, so as to convert them into relevant nitrates. The aqueous solution of these nitrates were use as a dopants. The 1 mol% of gadolinium nitrate and 1mol% of europium nitrate were assorted in the host material and dehydrated completely.

The dried powder was transferred to a glass tube and about 1.0 wt. % RAP agent was added. In this process we used ammonium fluoride as a RAP agent. The tube was closed with a tight stopper and slowly heated to 500°C for 2 h. The stopper was removed and the powders were transferred to a graphite crucible pre-heated to a suitable temperature. After heating in the graphite crucible for 1 h the resulting phosphor was rapidly quenched to room temperature. Belsare *et al.* well discussed about RAP in their literature [7]. The complete process involved in the reaction was represented as a flow chart in Fig. 1.

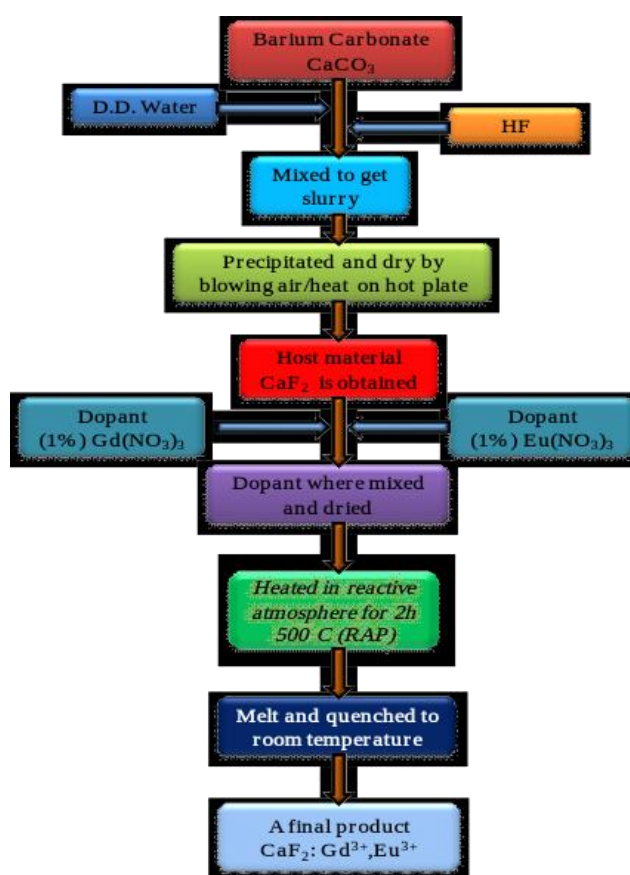


Fig.1. Flow chart of $\text{CaF}_2: \text{Gd}^{3+}, \text{Eu}^{3+}$ prepared via RAP.

3. RESULTS AND DISCUSSION

3.1 XRD Analysis

The formation of the $\text{CaF}_2: \text{Gd}^{3+}, \text{Eu}^{3+}$ sample in the crystalline phase synthesized by RAP was confirmed by XRD pattern as shown in Fig.2. The XRD pattern for $\text{CaF}_2: \text{Gd}^{3+}, \text{Eu}^{3+}$ agreed well with the standard data from ICDD file (00-004-0864). Also the XRD pattern show that CaF_2 lattice possesses cubic structure with a space group $Fm-3m$ (225) with lattice parameters $a = b = c = 5.2646 \text{ \AA}$ and interfacial angles $\alpha = \beta = \gamma = 90^\circ$. XRD pattern of $\text{CaF}_2: \text{Gd}^{3+}, \text{Eu}^{3+}$ phosphor as shown in fig.2.

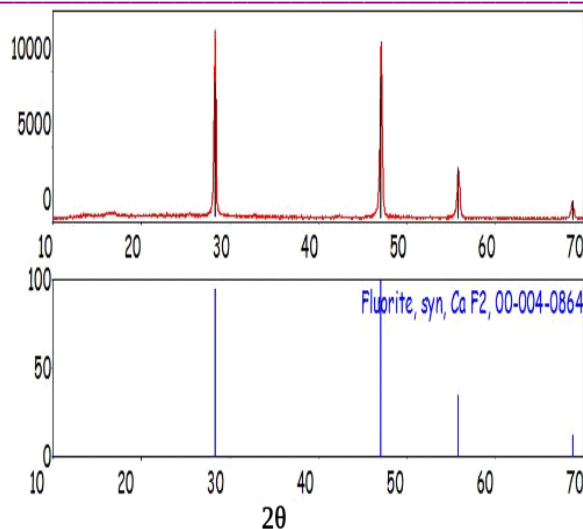


Fig.2.XRD patterns of $\text{CaF}_2: \text{Gd}^{3+}, \text{Eu}^{3+}$ synthesized by RAP.

3.2 VUV-UV PL Analysis

The emission spectra under excitation 274 and 203 nm are shown in Fig 4. The emission lines of Eu^{3+} peaked at about 593, 613, 650 and 700nm correspond to $^5\text{D}_0 \rightarrow ^7\text{F}_J$ ($J=1, 2, 3, 4$) transitions respectively and the $^5\text{D}_J$ ($J=0, 1, 2, 3$) $\rightarrow ^7\text{F}_J$ transition peaks of Eu^{3+} are much weaker than those of $^5\text{D}_0 \rightarrow ^7\text{F}_J$ transition. There are broad excitations lines spectra peaking optimum at about 203, 227 and 274 nm responsible for $^8\text{S}_{7/2} \rightarrow ^6\text{G}_J, ^6\text{D}_J, ^6\text{I}_J$ respectively[8] as shown in Fig 3.

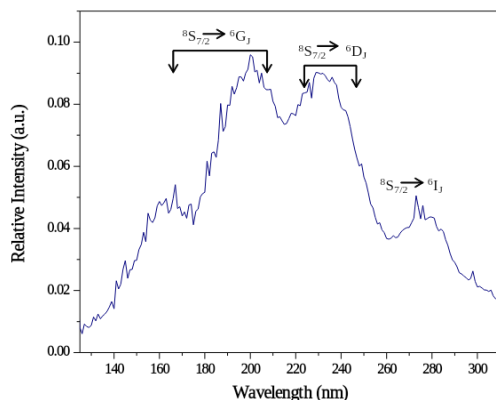


Fig.3.Excitation spectrum of $\text{CaF}_2: \text{Gd}^{3+}, \text{Eu}^{3+}$ monitored at 593 nm.

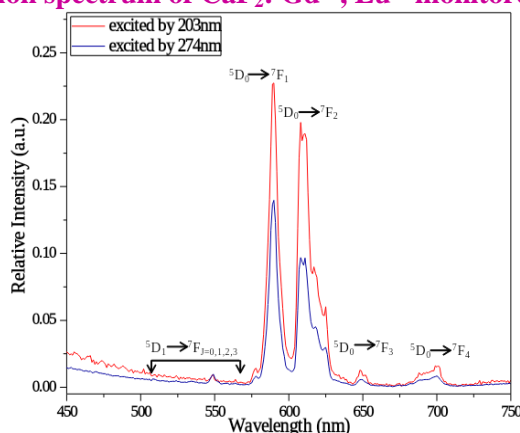


Fig.4.emission spectra of $\text{CaF}_2: \text{Gd}^{3+}, \text{Eu}^{3+}$ at excitation wavelength 203 and 274 nm.

The process transfer of energy and quantum splitting can happen by the combination of Gd³⁺ and Eu³⁺ in which Gd³⁺ and absorbing a VUV photon corresponding to ⁸S_{7/2}→⁶G_J. The incident high energy photon is cut into two visible photons emitted by Eu³⁺ ions. The energy of transitions ⁶G_J→⁶P_J on Gd³⁺ matches the ⁷F_J→⁵D₀ excitation energy on Eu³⁺. Upon excitation in the ⁶G_J levels of Gd³⁺ as the first step, energy is transferred by cross-relaxation between Gd³⁺ and Eu³⁺ which make Gd³⁺ fall into the ⁶P_J state and Eu³⁺ is excited into the ⁵D₀ state. The excited Eu³⁺ is responsible for the first visible photon. The first step is called as booming energy migration. In the second step the remaining excitation energy of Gd³⁺ in the ⁶P_J state is transferred to another nearing Eu³⁺ ion, i.e. Eu³⁺ ion exciting into a high state. Then a fast relaxation from a high excited state to ⁵D_J states will occur. After the first step, because the Eu³⁺ ion only excited into ⁵D₀ state, only the emissions of ⁵D₀→⁷F_J transitions are expected. However after the second step, all levels of ⁵D_{3,2,1,0} of Eu³⁺ are probably engaged, so the emission wavelength consists of all of the ⁵D_J (J=0,1,2,3) →⁷F_J transitions [9].

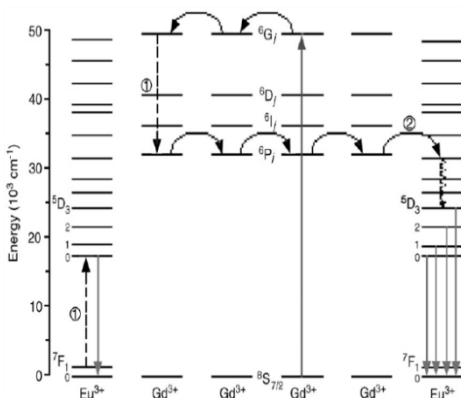


Fig.5. Energy level diagrams of Eu³⁺ and Gd³⁺ showing the cross-relaxation energy transfer process that leads to quantum splitting [9, 10]

Consecutively to calculate quantum efficiency, some assumption must be projected. The incident vacuum ultraviolet photon absorption efficiency cannot be taken into consideration. Some nonradiative losses at defects and impurities are disregarded. In the CaF₂:Gd³⁺, Eu³⁺ sample, different excitations are adopted including the excitation of Gd³⁺→⁶G_J with 203 nm and the excitation of Gd³⁺→⁶I_J with 273 nm. Upon excitation in ⁶I_J level with 273 nm, the quantum cutting never occurs because no cross-relaxation exists, so the ⁵D_J→⁷F_J transitions emission of Eu³⁺ has a normal branching ratio between ⁵D₀ and ⁵D_{1, 2, 3}. Upon 203 nm excitation in ⁶G_J level with, the quantum cutting can occur via two-step energy transfer. In the second step, the emission of Eu³⁺ has a normal branching ratio. The first step will pilot to the increase of ⁵D₀ emission. So the ratio of ⁵D₀ and ⁵D_{1, 2, 3} emissions is expected to increase. To determine the efficiency of the cross relaxation, the formula proposed by Wegh [11-17] was adopted as follows:

$$\frac{P_{CR}}{P_{CR} + P_{DT}} = \frac{R(^5D_0/^5D_{1,2,3})_{6G_J} + R(^5D_0/^5D_{1,2,3})_{6I_J}}{R(^5D_0/^5D_{1,2,3})_{6I_J} + 1}$$

Where P_{CR} is the probability for cross-relaxation, P_{DT} is the probability for the direct transfer from Gd³⁺ to Eu³⁺. R (⁵D₀/⁵D_{1, 2, 3}) is the ratio of the ⁵D₀ and ⁵D_{1, 2, 3} emission integral intensities. The subscript (⁶G_J or ⁶I_J) represents the excitation level for which the ratio is observed. From the emission spectra, the value of R (⁵D₀/⁵D_{1, 2, 3})⁶G_J and (⁵D₀/⁵D_{1, 2, 3})⁶I_J can be calculated 33.21 and 27.15, respectively. Therefore, the value of P_{CR}/P_{CR} + P_{DT} is 0.17. It means that there are 17% Gd³⁺ ions in the ⁶G_J excited state settle down through a two-step energy transfer emitting two visible photons in this method. So the quantum cutting efficiency of 117% can be obtained. Quantum cutting in the Gd to Eu understanding requires energy transfer over the Gd sublattice to Eu [10].

4. CONCLUSIONS

The inorganic material $\text{CaF}_2: \text{Gd}^{3+}, \text{Eu}^{3+}$ was successfully prepared through reactive atmosphere process. The XRD pattern confirmed its cubic structure. The visible quantum cutting and energy transfer through down-conversion was observed in $\text{CaF}_2: 1\% \text{Gd}^{3+}, 1\% \text{Eu}^{3+}$ and the quantum efficiency was found to be around 117% under the excitation of 203 nm equivalent $^8\text{S}_{7/2} \rightarrow ^6\text{G}_7$ transition of Gd^{3+} ions.

ACKNOWLEDGEMENTS

We are thankful to 4B8 VUV spectroscopy beam line scientists of Beijing Synchrotron Radiation Facility (BSRF), China for given that access in recording VUV on beamline 4B8 under dedicated synchrotron mode using remote access mode. One of the authors S.R. Jaiswal thankful to Head, Department of Physics SantGadge Baba Amravati University, Amravati for providing necessary facilities.

REFERENCES

- [1] C.R. Ronda, J. Alloys Compd. 225 (1993) 534.
- [2] M. Y. William, Phosphor Handbook, CRC press is an imprint of the Taylor & Francis Group, ISBN: 0-8493-3564-7.
- [3] S. Pote, C. Joshi, S. Moharil, P. Muthal, S. Dhopte. ISSN 1061-3862, International Journal of Self-Propagating High-Temperature Synthesis. 22 (2013) 37-40
- [4] B. Herden, A. García-Fuente, H. Ramanantoanina, T. Jüstel, C. Daul, W. Urland, Chemical physics letter. 620 (2015) 29-34.
- [5] W. Binder, S. Dislerhoff, J. Cameron, Dosimetric Properties of $\text{CaF}_2: \text{Dy}$, (a) Proc. II Int. Conf. on Lumin. Dosim., Gatlinberg, 1968, pp. 45–53; (b) Health Phys., 1969, vol. 17, no. 4, pp. 613–618.
- [6] (a) A.C. Lucas, R.H. Moss, B.M. Casper, Thermoluminescent $\text{CaF}_2: \text{Tm}$ and Method for Its Use, US Patent 4 039 834, 1977; (b) Lucas, A.C. and Casper, B.M., Thermoluminescence of Thulium Doped Calcium Fluoride, Proc. Int. Conf. on Lumin. Dosim., Sao Paulo (Brazil), 1977, pp. 131-139
- [7] P. Belsare, C. Joshi, S. Moharil, V. Kondawar, P. Muthal, S. Dhopte, J. Alloys Compd. 450 (2008) 468–472.
- [8] R.T. Wegh, E.V.D. van Loef, A. Meijerink, J. Lumin., 90 (2000) 111.
- [9] B. Liua, Y. Chena, C. Shia, H. Tanga, Y. Tao, Journal of Luminescence 101 (2003) 155–159.
- [10] R.T. Wegh, H. Donker, K. Oskam, and A. Meijerink, J. Lumin., 82 (1999) 93.
- [11] R.T. Wegh, H. Donker, K. Oskam, A. Meijerink, Science 663 (1999) 283.
- [12] N. Kodama, Y. Watanabe, Appl. Phys. Lett. 4141 (2004) 84.
- [13] N. Kodama, S. Oishi, J. Appl. Phys. 103515 (2005) 98.
- [14] R. Hua1, J.H. Niu, B.J. Chen, M.T.Z. Li, T. Yu, W.L. Li, Nanotechnology 1642 (2006) 17.
- [15] Y. Zhou, S.P. Feofilov, J.Y. Jeong, D.A. Keszler, R.S. Meltzer, Phys. Rev. B 075129 (2008) 77.
- [16] M. Karbowski, A. Mech, W. Ryba-Romanowski, J. Lumin. 65 (2005) 114.
- [17] B. Liu, Y.H. Chen, C.S. Shi, H.G. Tang, Y. Tao, J. Lumin. 101 (2003) 155.



STRUCTURAL AND OPTICAL STUDIES ON IN DOPED ZINC OXIDE THIN FILMS BY SPRAY PYROLYSIS TECHNIQUES

L.H. Kathwate^a, Nitin T. Gurude^a, Dipak Kadam^a, M. B. Awale, S. D. Lokhande^a,
P.M. Kulal^b, V.D. Mote^{a*}

^aThin Films and Materials Science Research Laboratory, Department of Physics, Dayanand Science College, Latur- 413 512, Maharashtra, India.

^bDepartment of Physics, Shivaji Mahavidhyala, Renapur, Maharashtra, India

*E-mail corresponding author: vmote.physics@gmail.com

ABSTRACT :

We report a systematic studies on the structural and optical properties of In doped Zinc Oxide thin films grown by spray pyrolysis route. Samples were systematically characterized using x-ray diffraction (XRD) and UV-Vis spectroscopy. X-ray diffraction (XRD) results confirm that all prepared thin films have hexagonal crystal structure without any extra impurities. From X-ray diffraction data, the lattice parameters and volume of the unit cell increased with increasing In doping, indicating the successful incorporation of In ions into ZnO. The average crystalline size in the range of 19-40 nm. The optical absorption spectra of the thin films obtained using UV-Vis spectrometer. The values of band gap energy have been found to be 3.21 eV for pure ZnO and 3.09 eV for 6% In doped ZnO films.

KEYWORDS: In doped ZnO; thin films; x-ray diffraction; optical properties.

1. INTRODUCTION

ZnO is an important material in the II-VI family with a wide band gap (3.3 eV) and a large excitonic binding energy (60 meV) owing to its superior and diverse properties such as piezoelectricity, chemical stability, biocompatibility and high voltage-current nonlinearity etc. It has a variety of applications such as catalysis, solar cells and other optoelectronic devices. All the properties make doped ZnO promising materials that many combine the optical transport and gas sensing properties for devices such as gas sensor, transparent conducting films, piezoelectric transducers and photocatalytic activity [1-4]. There are very limited researches to develop In doped ZnO thin film for gas sensing applications.

Most transition metals doped ZnO samples are grown employing complex and expensive techniques like molecular beam epitaxy metal, organic vapour phase epitaxy, pulsed laser deposition that require high grown temperatures, thermal hydrolysis technique [5], spray pyrolysis [6], chemical vapour deposition [7], thermal evaporation of Zn [8], hydrothermal syntheses [9, 10], low temperature wet-chemical reaction [11].

In the present work, pure and 6 % In doped ZnO thin films were synthesized by spray pyrolysis method. The structural and optical properties of pure as well as In doped ZnO thin films were systematically investigated. Additional, theoretical calculation based was carried out in order to strain and crystalline size of prepared samples. This study might help to the novel applications in opto-electronics and nano devices.

2. MATERIALS AND METHODS

Pure and In doped Zinc oxide thin films were deposited on glass substrate at the substrate temperature of 400 using fully atomized spray pyrolysis technique. The precursor solution was prepared by mixing 0.1 M of Zinc acetate dehydrate, In 20 mL deionized water. For In doping in Zinc Oxide, appropriate amount of Indium Acetate dehydrate for preparing 0.1M concentration was added into the precursor solution.

The solution was vigorously stirred using magnetic stirrer for 10 min. Then the prepared solution was into the spray dispenser. The deposition parameters were 2 mL/min solution flow rate, 2 mm diameter of spray nozzle, 20 cm of spray nozzle substrate distance. Atmospheric air was used as carrier gas with one m bar pressure. The thickness was of all the films was minted constant 215 ± 20 nm and confirmed through weight difference method. X-ray diffractometer was used to study the impact of Indium doping on the structural properties of nanostructure Zinc oxide thin films. The optical measurement of the deposited thin films were observed using UV –VIS spectrophotometer in the wavelength range 200 -800 nm.

3. RESULT AND DISCUSSION

The XRD patterns of pure and 6% In doped Zinc oxide thin films is shown in figures 1(a & b). All the prepared films exhibited the polycrystalline nature with hexagonal crystal structure without any extra impurities phases. The absence of extra peaks other than (002) and (101) plane of ZnO crystal clearly indicated that In ions were substituted in the Zinc oxide matrix. No extra peaks related to the crystal phases of In clusters or In O compounds were found, it confirm that the doping level is within the solubility limit. The say axis (002) growth of Zinc oxide thin films may be due to the starting inorganic precursor effect. In our present case, the peak position shifted to the lower or the higher angle shifted it means that the possibility of In^{2+} ions occupying the interstitial sites.

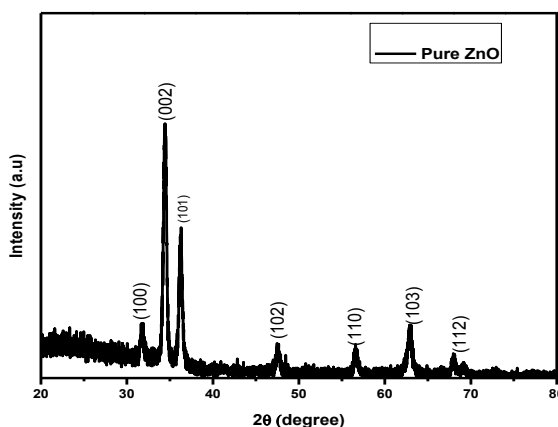


Fig.1(a). X-ray diffraction pattern of pure ZnO thin films.

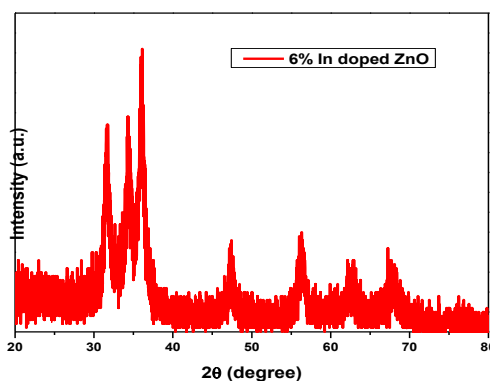


Fig.1(b). X-ray diffraction pattern of 6% In doped ZnO thin films.

The lattice parameters were calculated using following equation:

The lattice parameters were calculated from XRD diffraction using following equation:

$$\frac{1}{d^2} = \frac{4(h^2+hk+k^2)}{3a^2} + \frac{l^2}{c^2} \quad (1)$$

Here, d – is interspacing distance, (hkl) Mirror Indices, a and c are lattice parameters. The calculated lattice parameters are shown in table 1. From table it is clear that the lattice increased with increasing In content it may due to larger ionic radius In^{2+} ions as compared to the Zn^{2+} ions. The volume of the unit cell was also found that the value of volume is increased with increasing In doping level. The bond length and u parameters are also calculated and given in table 1. The u parameter of Zinc Oxide thin films was smaller than that of In doped Zinc oxide thin films. Based on this structural parameter studies, it is clear that In impact on structural properties of Zinc Oxide (ZnO) thin films.

The average crystallite size was estimated using well known Scherer's formula:

$$D = \frac{k\lambda}{\beta \cos\theta} \quad (3)$$

Where D is crystallite size (nm), k is shape factor (0.9), λ is X-ray wave length (1.5406 Å). B is full width half maxima (radian), θ is Bragg angle (radian). The average crystallite sizes of pure ZnO and In doped ZnO thin films are tabulated in table 1. From table it is clear that the average crystallite size was in the range of 19 – 40 nm of pure and In doped ZnO films.

Table 1: Lattice parameters, volume, average crystallite size, strain and bond length of $\text{Zn}_{1-x}\text{In}_x\text{O}$ thin films.

Samples In doping	Lattice Parameters (Å)		Volume (Å) ³	D (nm)	Strain	L (Å)
	a	c				
Pure ZnO	3.2476	5.1948	47.448	30.3134	0.001358	1.9755
6%	3.2606	5.2068	47.9386	15.3194	0.00271	1.9823

The optical absorption spectra of pure and In doped ZnO thin films as shown in fig 2. The observed sharp absorption edge in pure ZnO samples confirmed that the films were in highly crystalline nature. As the doping varied 6%, the absorption was gradually decreased due to the more impurity state below the conduction band. From fig. 2(a) and (b), it was observed that the absorption edge is shifted to higher wavelength. The optical band gap was calculated using Tauc's plot by extra plotting the linear region of $(\alpha h\nu)^2$ versus incident energy ($h\nu$) as shown in fig 3. The calculated band gap was found to that decreased gradually from 3.21-3.07 eV Fig 3(a, & b). As increases In in doping concentrations. The decrease in band gap energy is attributed to the exchange interaction of s and p electrons in the conduction band of ZnO and localized electrons of doped In ions.

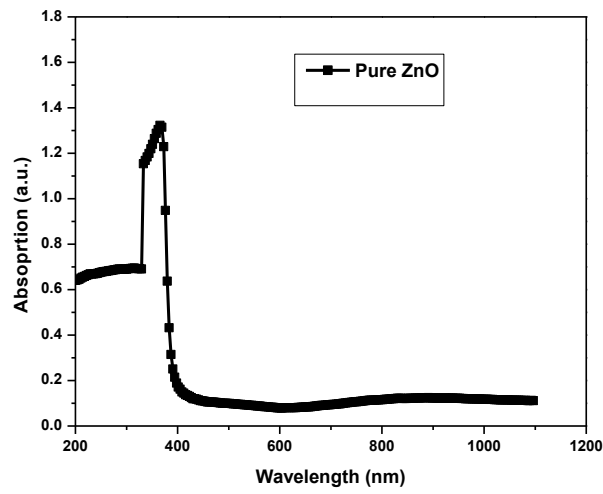


Fig.2(a). Absorption spectra of pure ZnO thin films.

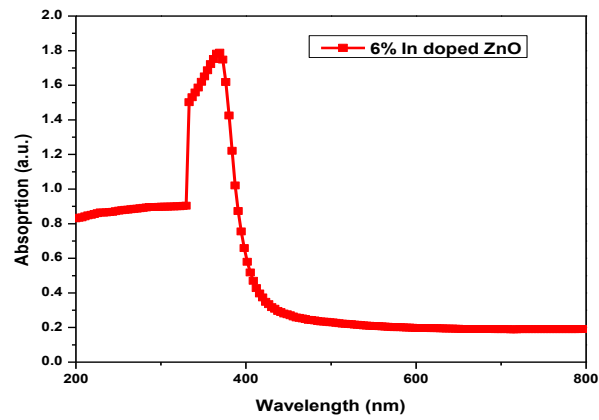


Fig.2(b). Absorption spectra of In doped ZnO thin films.

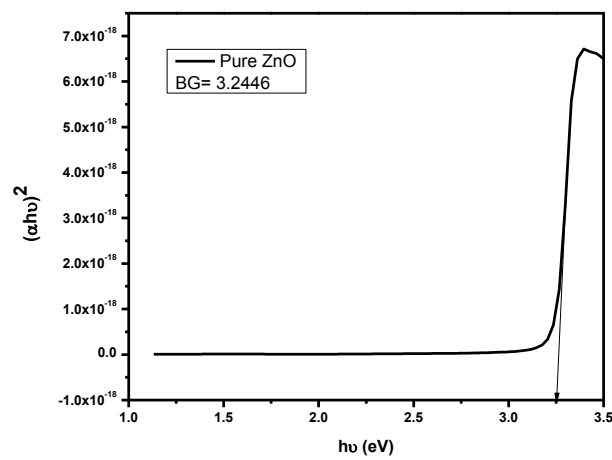


Fig.3(a). Tauc's plot of pure ZnO thin films.

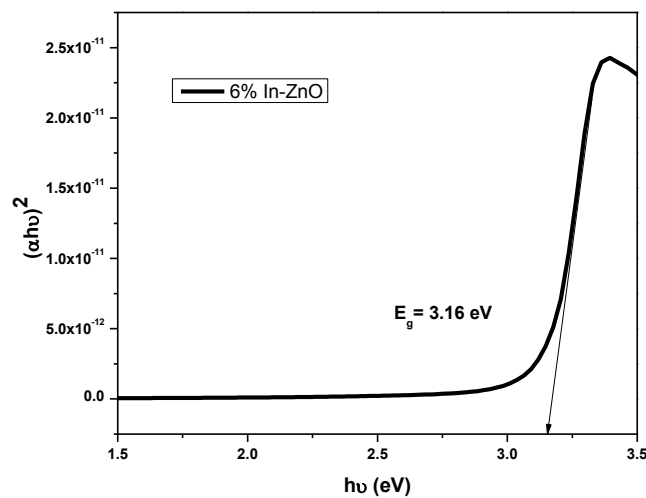


Fig.3(b). Tauc's plot of 2% In doped ZnO thin films.

4. CONCLUSIONS

The pure and In doped ZnO thin films were successfully deposited on the glass substrates using spray pyrolysis technique. Structural studies reveal that pure and ion doped ZnO thin films have hexagonal crystal structure. The lattice parameters of cobalt doped ZnO thin films were increased. The films shows all films have polycrystalline nature increase in volume of unit cell were observed as In doping concentration increased. The average crystalline size was found to be in the range of 19 - 40nm of pure and In doped ZnO thin films. The optical properties shows that the energy band gap was decreased with increased In in Zinc Oxide thin films. The observed results suggest that doping concentration provides new direction for spintronics and solar cell applications in future.

5. REFERENCES

1. Zhang J, Wang S, Xu M, Wang Y, Zhu B, Zhang S, et al. *Crystal growth Des* 9 (2009) p3532.
2. Nayak PK, Yang J, Kim J, Chung S, Jeong J, Lee C, et al. *J Phys D: Appl Phys* 42 (2009) p035102.
3. Bdikin KI, Gracio J, Ayochi R, Schwarz R, Kholkin AL, *Nanotechnology* 21(2010) p235703.
4. Wang Y, Li X, Wang N, Quan X, Chen Y. *Sep purify Technol* 62 (2008) p727.
5. H. K. Park, D. K. Kirn, C. H. Kirn, *J. Am. Ceram. Soc.* 80 (1992) 743.
6. T. T. Kodas, *Adv. Mater.* 6 (1989) 180.
7. B. P. Zhang, N. Y. Binh, K. Wakatsuki, Y. Segawa, Y. Yamada, N. Usami, M. Kawasaki, H. Koinuma, *J. Phys. Chem. B* 108 (2004) 10899.
8. G. Z. Shen, Y. Bando, Ch.J. Lee, *J. Phys. Chem. B* 109 (2005) 10578.
9. S. I. Hirano, *Ceram. Bull.* 66 (1987) 1342.
10. H. Zhang, D. R. Yang, D. S. Li, X. Y. Ma, S. Z. Li, D. L. Que, *Cryst. Growth Des.* 2 (2005) 547.
11. B. Liu, H.C. Zeng, *Langmuir* 20 (2004) 4196.



INHOMOGENEOUS PLANE SYMMETRIC COSMOLOGICAL MODELS WITH COSMOLOGICAL CONSTANT

¹A. R. Gupta and ²M. M. Sancheti

¹Department of Mathematics, L. P. G. Arts and Science College, Shirpur Jain, Washim, Maharashtra.

²Department of Mathematics, R. A. Arts Science and Commerce College, Washim, Maharashtra.

Corresponding Author:-apuravgupta2011@gmail.com

ABSTRACT :

We have investigated the inhomogeneous plane symmetric models with perfect fluid and cosmological constant, the perfect fluid is taken to be one obeying us all of state (EOS) $P = \gamma\rho$ with $\gamma \in [0, 1]$. Some physical properties of the model are discussed.

KEYWORDS : Inhomogeneous Plane Symmetric model, cosmology, perfect fluid, cosmological constant.

1. INTRODUCTION

In recent years, modifications of general relativity are attracting more attention to explain the late time cosmic acceleration of universe. This late time cosmic accelerated expansion of universe has been confirmed by high red-shift supernovae experiments (Riess et al 1998; Perlmutter et al 1999; Bennet et al 2003). Broadly, the model building undertaken in the literature to capture the alternative theory of gravitation can be classified into two categories: dimensional scalar field and non-dimensional scalar field model. In 1961, Brans and Dicke formulated the scalar-tensor theories of gravitation on the basis of coupling between an adequate tensor field and scalar field ϕ . The scalar field has a dimension of G^{-1} where G is the gravitational constant. Therefore, ϕ^{-1} play the role of $G(t)$. This theory successfully describes the Mach's principle but fails to explain the missing matter problems and absolute properties of space. Later on Saez and Ballester (1985) developed a scalar-tensor theory in which the metric is coupled with a dimensionless scalar field in a simple manner. This coupling gives a satisfactory description of weak fields.

The recent observations suggest that the matter distribution in the present universe is on the whole isotropic and homogeneous. But on the theoretical ground, the universe could have not had such smoothed out picture close to big bang singularity, the assumption of spherically symmetric and isotropy cannot be strictly valid. Therefore, inhomogeneous cosmological models play an important role to study the essential features of universes such as process of homogenization and formation of galaxies at early stage of evolution. So in literature, many authors consider plane symmetry, which is less restrictive than spherical symmetry and provides an avenue to study inhomogeneities in early universe. Da Silva and Wang (1998), Anguige (2000), Nouri-Zonoz and Tavanfar (2001), Pradhan et al. (2003, 2007) and Yadav (2011) have studied the plane symmetric and inhomogeneous cosmological models in different physical context.

In our paper, we find an inhomogeneous plane symmetric model with perfect fluid. The paper is organized as follows: In section 2, we have provided the metric and field equation in connection to the proposed model for inhomogeneous plane symmetric model. In Section 3, we have provided the physical properties of the model.

2. BASIC EQUATIONS

We consider the plane symmetric metric in the form

$$ds^2 = -dt^2 + A^2 dx^2 + B^2 (dy^2 + dz^2) \quad \dots (2.1)$$

Where, the metric potential A & B are the function of x & t alone. The energy momentum tensor for perfect fluid distribution is given by

$$T_i^j = (P + \rho)u_i u^j - P\delta_i^j \quad \dots (2.2)$$

Where u^i is the flow vector satisfy

$$g_{ij} u^i u^j = 1 \quad \dots (2.3)$$

Here ρ is the total energy density of a perfect fluid, while P is the corresponding pressure. P & ρ are related by the equation of state.

In a co-moving system of co-ordinates from (2.2), we find

$$T_1^1 = T_2^2 = T_3^3 = -P; \quad T_4^4 = \rho \quad \dots (2.4)$$

The inhomogeneous field equation

$$-8\pi T_i^j = R_i^j - \frac{1}{2}R\delta_i^j - \Lambda\delta_i^j \quad \dots (2.5)$$

For line element (2.1) are

$$\frac{\dot{B}^2}{B^2} + \frac{2\ddot{B}}{B} = 8\pi P + \Lambda \quad \dots (2.6)$$

$$\frac{\ddot{A}}{A} + \frac{\dot{A}\dot{B}}{AB} + \frac{\ddot{B}}{B} = 8\pi P + \Lambda \quad \dots (2.7)$$

$$\frac{\dot{B}^2}{B^2} + \frac{2A\dot{B}}{AB} = -8\pi P + \Lambda \quad \dots (2.8)$$

Substituting (2.6) from (2.7), we have

$$\frac{d}{dt} \left(\frac{\dot{A}}{A} - \frac{\dot{B}}{B} \right) + \left(\frac{\dot{A}}{A} - \frac{\dot{B}}{B} \right) \left(\frac{\dot{A}}{A} + \frac{2\dot{B}}{B} \right) = 0 \quad \dots (2.9)$$

Let V be a function of 't' denoted by

$$V = A^2 B \quad \dots (2.10)$$

Then from (2.9), we obtain

$$\frac{d}{dt} \left(\frac{\dot{A}}{A} - \frac{\dot{B}}{B} \right) + \left(\frac{\dot{A}}{A} - \frac{\dot{B}}{B} \right) \frac{\dot{V}}{V} = 0 \quad \dots (2.11)$$

By integrating above equation, we get

$$\frac{A}{B} = L_2 \exp \left(L_1 \int \frac{1}{V} dt \right) \quad \dots (2.12)$$

Where L_1 & L_2 are the constants of integration.
In view of

$$V = AB^2 \rightarrow A = \frac{V}{B^2}$$

We can write A, B in the explicit form

$$A = D_2 V^{\frac{1}{3}} \exp\left(X_2 \int \frac{1}{V} dt\right) \quad \dots (2.13)$$

$$B = D_1 V^{\frac{1}{3}} \exp\left(X_1 \int \frac{1}{V} dt\right) \quad \dots (2.14)$$

Where D_i ($i = 1,2$) & X_i ($i = 1,2$) satisfy the relation

$$D_1^2 D_2 = 1 \quad \text{and} \quad 2X_1 + X_2 = 0$$

From the equations (2.6), (2.7) and (2.8) we yield

$$\frac{2\dot{B}^2}{B^2} + \frac{2\ddot{B}}{B} + \frac{4\dot{A}\dot{B}}{AB} + \frac{\ddot{A}}{A} = 12\pi(P - \rho) + 3\Lambda \quad \dots (2.15)$$

In view of $V = B^2 A$, from (2.15) we obtain

$$\frac{\dot{V}}{V} = 12\pi(P - \rho) + 3\Lambda \quad \dots (2.16)$$

The conservation law for the energy momentum tensor gives

$$\dot{\rho} = -\frac{\dot{V}}{V}(\rho + P) \quad \dots (2.17)$$

From (2.16) and (2.17), we have

$$\dot{V} = \sqrt{-24\pi V^2 \rho + 3\Lambda V^2 + 2C_1} \quad \dots (2.18)$$

Where C_1 being integration constant.

Rewriting (2.17) in the form

$$\frac{\dot{\rho}}{\rho + P} = -\frac{\dot{V}}{V} \quad \dots (2.19)$$

And taking into account that the pressure and the energy density obeying an equation of state of type $P = f(\rho)$, we conclude that ρ & P are the function of V .

Hence the right hand side of (2.16) is a function of V only

$$\dot{V} = 12\pi(P - \rho)V + 3\Lambda V = F(V) \quad \dots (2.20)$$

From the mechanical point of view equation (2.20) curve interpreted as equation of motion of single particle with unit mass under the force $F(V)$, then

$$\dot{V} = \sqrt{2(\epsilon - U(V))} \quad \dots (2.21)$$

Here ϵ can be viewed as energy and $U(V)$ as the potential of the force F. Comparing (2.18) and (2.21), we find

$$\epsilon = C_1 \& U(V) = 12\pi V^2 \rho - \frac{3}{2} \Lambda V^2 \quad \dots (2.22)$$

Finally, we write the solution of (2.18) in the quadrature form

$$\int \frac{dV}{\sqrt{2(C_1 - 12\pi V^2 \rho + \frac{3}{2} \Lambda V^2)}} = t + t_0 \quad \dots (2.23)$$

Where, the integration constant t_0 can be taken to be zero, since it only gives a shift in time. Hence, let us take $t_0 = 0$.

$$\int \frac{dV}{\sqrt{2(C_1 - 12\pi V^2 \rho + \frac{3}{2} \Lambda V^2)}} = t \quad \dots (2.24)$$

3. UNIVERSE AS A BINARY MIXTURE OF PERFECT FLUID

We consider the evolution of the plane of symmetric universe filled with the perfect fluid

$$P = \gamma \rho \quad \dots (3.1)$$

Here the γ is constant and lies in the interval $\gamma \in [0,1]$. Depending on its numerical values γ describes the following types of universe

$$\left. \begin{aligned} \gamma = 0 & \text{(Dust universe)} \\ \gamma = \frac{1}{3} & \text{(Radiation universe)} \\ \gamma \in \left(\frac{1}{3}, 1\right) & \text{(Hard Universe)} \\ \gamma = 1 & \text{(Zeldovich Universe or Stiff matter)} \end{aligned} \right\} \quad \dots (3.2)$$

In a co-moving frame the conservation law of energy momentum tensor leads to the balance equation for the energy density

$$\dot{\rho} = -\frac{\dot{V}}{V} [\rho + P] \quad \dots (3.3)$$

From the equation (3.3) we get,

$$P = \frac{\gamma \rho_0}{V^{1+\gamma}} \quad \dots (3.4)$$

&

$$\rho = \frac{\rho_0}{V^{1+\gamma}} \quad \dots (3.5)$$

Here ρ_0 is the integration constant.

Therefore, equation (2.24) gives

$$\int \frac{dV}{\sqrt{2C_1 - 24\pi \rho_0 V^{1+\gamma} + 3\Lambda V^2}} = t \quad \dots (3.6)$$

Case I:

Let us consider $\gamma = 1$ (Zeldovich universe) for $C_1 = 0$, equation (3.6) reduces to

$$\int \frac{dV}{\sqrt{(\sqrt{3\Lambda V})^2 - (\sqrt{24\pi\rho_0})^2}} = t \quad \dots (3.7)$$

This gives,

$$V = \frac{\sqrt{8\pi\rho_0}}{\sqrt{\Lambda}} \cosh \sqrt{3\Lambda} t \quad \dots (3.8)$$

Putting the value of V in eqⁿ (2.13) and (2.14), we get

$$\left. \begin{aligned} A &= D_2(K_1)^{\frac{1}{6}} \cosh^{\frac{1}{3}}(\sqrt{3\Lambda}t) (\operatorname{sech}(\sqrt{3\Lambda}t) + \tanh(\sqrt{3\Lambda}t))^{\frac{X_2}{\sqrt{3\Lambda}K_1}} \\ B &= D_1(K_1)^{\frac{1}{6}} \cosh^{\frac{1}{3}}(\sqrt{3\Lambda}t) (\operatorname{sech}(\sqrt{3\Lambda}t) + \tanh(\sqrt{3\Lambda}t))^{\frac{X_1}{\sqrt{3\Lambda}K_1}} \end{aligned} \right\} \quad \dots (3.9)$$

Where $K_1 = \sqrt{\frac{8\pi\rho_0}{\Lambda}}$ & $D_i (i = 1,2)$ & $X_i (i = 1,2)$ satisfy the relation

$$D_1^2 D_2 = 1 \quad \& \quad 2X_1 + X_2 = 0$$

From equation (3.4) and (3.8), we have

$$\rho = \frac{\Lambda}{8\pi \cosh^2(\sqrt{3\Lambda}t)} \quad \dots (3.10)$$

i.e.,

$$P = \rho = \frac{\Lambda}{8\pi \cosh^2(\sqrt{3\Lambda}t)} \quad \dots (3.11)$$

The physical quantities of observational interest in cosmology are the expansion scalar θ , the mean anisotropy parameter Δ , the shear scalar B^2 and the deceleration parameter q .

They are defined as

$$\theta = 3H \quad \dots (3.12)$$

$$\Delta = \frac{1}{3} \sum_{i=1}^3 \left(\frac{\Delta H_i}{H} \right)^2 \quad \dots (3.13)$$

$$\sigma^2 = \frac{1}{2} \left(\sum_{i=1}^3 H_i^2 - 3H^2 \right) = \frac{3}{2} \Delta H^2 \quad \dots (3.14)$$

$$q = \frac{d}{dt} \left(\frac{1}{H} \right) - 1 \quad \dots (3.15)$$

By using above equations, we can express the physical quantities as

$$\theta = \sqrt{3\Lambda} \tanh \sqrt{3\Lambda} t \quad \dots (3.16)$$

$$\Delta = \frac{2}{9H^2} \left[\frac{\dot{A}}{A} - \frac{\dot{B}}{B} \right]^2 \quad \dots (3.17)$$

$$\sigma^2 = \frac{1}{3} \left[\frac{\dot{A}}{A} - \frac{\dot{B}}{B} \right]^2 \quad \dots (3.18)$$

Where A and B by using equation (3.9)

$$q = -3 \operatorname{cosech}^2(\sqrt{3\Lambda}t) - 1 \quad \dots (3.19)$$

Case II:

Let us consider $\gamma = 0$ (Dust universe) for $C_1 = 0$, equation (3.6) reduces to

$$\frac{1}{\sqrt{3\Lambda}} \int \frac{dV}{\sqrt{\left(V - \frac{K}{2}\right)^2 + \left(\frac{K}{2}\right)^2}} = t \quad \dots (3.20)$$

This gives

$$V = \frac{K}{2} [\cosh \sqrt{3\Lambda}t] + \frac{K}{2} \quad \dots (3.21)$$

From (2.13), (2.14) and (3.21), we get

$$\left. \begin{aligned} A &= D_2 \left(\frac{K}{2} \cosh \sqrt{3\Lambda}t + \frac{K}{2} \right)^{\frac{1}{3}} e^{X_2 \int \frac{dt}{\frac{K}{2} \cosh \sqrt{3\Lambda}t + \frac{K}{2}}} \\ B &= D_1 \left(\frac{K}{2} \cosh \sqrt{3\Lambda}t + \frac{K}{2} \right)^{\frac{1}{3}} e^{X_1 \int \frac{dt}{\frac{K}{2} \cosh \sqrt{3\Lambda}t + \frac{K}{2}}} \end{aligned} \right\} \quad \dots (3.22)$$

Where $K = \frac{8\pi\rho_0}{\Lambda}$ & $D_i (i = 1,2)$ & $X_i (i = 1,2)$ satisfy the relation

$$D_1^2 D_2 = 1 \quad \& \quad 2X_1 + X_2 = 0$$

From equation (3.4) and (3.21), we have

$$\rho = \frac{\rho_0}{\frac{K}{2} \cosh \sqrt{3\Lambda}t + \frac{K}{2}} \quad \dots (3.23)$$

i.e.,

$$P = 0 \quad \dots (3.24)$$

The physical quantities of observational interest in cosmology are the expansion scalar θ , the mean anisotropy parameter Δ , the shear scalar B^2 and the deceleration parameter q .

By using above equations, we can express the physical quantities as

$$\theta = \frac{\sqrt{3\Lambda} \sinh \sqrt{3\Lambda}t}{\cosh \sqrt{3\Lambda}t + 1} \quad \dots (3.29)$$

$$\Delta = \frac{2}{9H^2} \left[\frac{\dot{A}}{A} - \frac{\dot{B}}{B} \right]^2 \quad \dots (3.30)$$

$$\sigma^2 = \frac{1}{3} \left[\frac{\dot{A}}{A} - \frac{\dot{B}}{B} \right]^2 \quad \dots (3.31)$$

Where A and B by using equation (3.22)

$$q = -3 \operatorname{cosech} \sqrt{3\Lambda}t (\operatorname{cosech} \sqrt{3\Lambda}t + \coth \sqrt{3\Lambda}t) - 1 \quad \dots (3.32)$$

4. CONCLUSION

In this paper, we have studied the plane symmetric in homogeneous cosmological models with perfect fluid as source of matter within the framework of scalar-tensor theory of gravitation. The exact solution to the corresponding field equation is found. The inclusion of the perfect fluid into the system gives rise to an accelerated expansion of the model. As a result, we approached to infinity quicker than it does when the universe is filled with perfect fluid alone. The solution for constant deceleration have been studied in detail for power-law and exponential forms. The particular cases for $\gamma = 1$ and $\gamma = 0$ have also been analysed in detail.

5. REFERENCE

- [1] Anguige, K.: Class Quantum Gravi 17, 2117 (2000)
- [2] Bennet, C.L., et al.: Astrophys. J. Suppl. Ser. 148, 1 (2003)
- [3] Brans, C., Dicke, R.H.: Physical Review 124, 925 (1961)
- [4] Da Silva, M.F.A., Wang, A.: Phys Lett A A244, 462 (1998)
- [5] Marra, V., Paakkonen, M.: JCAP 01, 025 (2008)
- [6] Nouri-Zonoz, M., Tavanfar, A.R.: Class Quantum Gravi 18, 4293 (2001)
- [7] Pradhan, A., Pandey, H.R.: Int J Mod Phys. D 12, 941 (2003)
- [8] Pradhan, A., Rai, K. K., Yadav, A. K.: Braz. J. Phys. 37 , 1084 (2007)
- [9] Riess, A. G., et al.: Astron J. 116 , 1009 (1998)
- [10] Saez, D., Ballester, V.J.: PhysLett A 113 , 467 (1985)
- [11] Katore, S.D, Adhao, K.S, Sancheti, M.M: Astrophys Space Sci 333, 333-341 (2011)
- [12] Yadav, A. K.: Int. J. Theor. Phys. 49, 1140, (2011).



CADMIUM CHLORIDE AN EFFECTIVE CATALYST FOR KNOEVENAGEL REACTION IN WATER

K. F. Shelke, A. D. Badar and J. B. Devhade

Department of Chemistry, Late PushpadeviPatil Arts and Science College,
Risod, Dist. Washim (MS), India
E-mail: kiranshelke82@gmail.com

ABSTRACT :

Efficient synthesis of 2, 2-dimethyl-5- [(4-oxo-4H-chromen-3-yl) methylene]-1, 3-dioxane-4, 6-diones by Knoevenagel condensation of aldehydes with Meldrum's acid in the presence of catalytic amount of cadmium chloride in water medium at room temperature. Simple work-up procedure, mild reaction conditions, short reaction times and good yield of products are the advantages of this method. Moreover, the catalyst used is easily available, inexpensive, non-toxic and eco-friendly.

KEYWORDS : Knoevenagel reaction, Cadmium chloride, Aldehyde, Meldrum's acid.

1. INTRODUCTION

Knoevenagel condensation is one of the most important reaction for the preparation of substituted alkenes by reactions of carbonyl compounds with active methylene compound [1]. The Knoevenagel condensation reactions are classically catalyzed by base in liquid-phase systems; various catalysts are known to effect the reaction with different aldehydes and active methylene group.

Meldrum's acid (2,2-dimethyl-1,3-dioxane-4,6-dione) is an active methylene compound having rigid cyclic structure with high acidity ($pK_a = 4.9$) and it undergoes hydrolysis very easily [2].

Compounds having chromone moiety are synthetically versatile molecules with a reactive carbonyl group. They have considerable significance for their biological activities [3] and for their reactivity towards nucleophiles, which allow the synthesis of a wide variety of heterocycles.

Water is unique solvent due to easy availability, cheap, non-toxic, safer to organic solvents and environmental benign[4]. Cadmium chloride ($CdCl_2$) has exploited in the organic synthesis as a non-toxic, inexpensive, eco-friendly nature, easy handling and Lewis acid mild catalyst [5].

2. EXPERIMENTAL SECTION

2.1. Reagents and analysis:

All chemicals were purchased from Merck, Aldrich and Rankem chemical companies and used without further purification. The uncorrected melting points of compounds were taken in an open capillary in a paraffin bath. The progress of the reactions was monitored by TLC (Thin Layer Chromatography). IR spectra were recorded on Perkin-Elmer FTIR spectrophotometer in KBr disc. 1H NMR spectra were recorded on an 300 MHz FT-NMR spectrometer in $CDCl_3$ as a solvent and chemical shift values are recorded in units δ (ppm) relative to tetramethylsilane (Me_4Si) as an internal standard.

2.2. Spectral data of compounds

(3a) IR (KBr, cm^{-1}): 3062, 2996, 1732, 1670, 1396, 1251. ^1H NMR (300 MHz, CDCl_3) δ (ppm): 1.8 (6H, s, $2\times\text{CH}_3$), 7.2-8.1 (4H, m, aromatic), 8.7 (1H, s, olefinic), 9.6 (1H, s, $\text{C}_2\text{-H}$ of chromone moiety). EIMS (m/z , %): = 301 [M+1].

(3d) IR (KBr, cm^{-1}): 3065, 2989, 1729, 1674, 1392, 1293, 791. ^1H NMR (300 MHz, CDCl_3) δ (ppm): 1.9 (6H, s, $2\times\text{CH}_3$), 7.2-8.2 (3H, m, aromatic), 8.6 (1H, s, olefinic), 9.5 (1H, s, $\text{C}_2\text{-H}$ of chromone moiety). EIMS (m/z , %): = 370 [M+1].

(3f) IR (KBr, cm^{-1}): 3084, 3018, 1714, 1662, 1392, 1280, 798. ^1H NMR (300 MHz, CDCl_3) δ (ppm): 1.8 (6H, s, $2\times\text{CH}_3$), 7.2-8.3 (2H, s, aromatic), 8.6 (1H, s, olefinic), 9.5 (1H, s, $\text{C}_2\text{-H}$ of chromone moiety). EIMS (m/z , %): = 370 [M+1].

(3g) IR (KBr, cm^{-1}): 3063, 2993, 1735, 1664, 1395, 1280, 805. ^1H NMR (300 MHz, CDCl_3) δ (ppm): 1.8 (6H, s, $2\times\text{CH}_3$), 7.2-8.2 (3H, m, aromatic), 8.6 (1H, s, olefinic), 9.6 (1H, s, $\text{C}_2\text{-H}$ of chromone moiety). EIMS (m/z , %): = 380 [M+1].

2.3. Synthesis of 2,2-dimethyl-5-[(4-oxo-4H-chromen-3-yl)methylene]-1,3-dioxane-4,6-dione 3(a-h):

A mixture of aromatic aldehyde (1 mmol), Meldrum's acid (1 mmol), CdCl_2 (2 mol%) and 10 mL water were taken in a single neck round bottom flask equipped with mechanical stirrer and stirred at room temperature for the appropriate time given in Table 2. The completion of the reaction was monitored by TLC. The solid product was filtered and recrystallized from ethyl acetate to get pure product. All the products were characterized by IR, ^1H NMR and mass spectra and by comparison of their physical characteristics with those of the authentic compounds

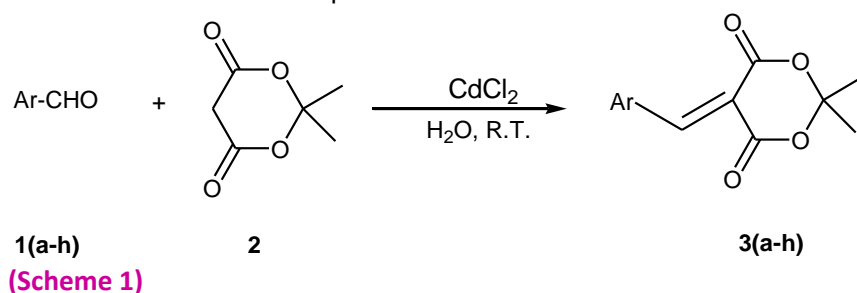


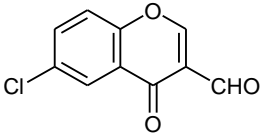
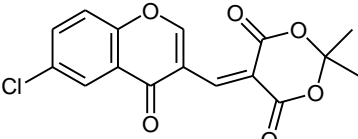
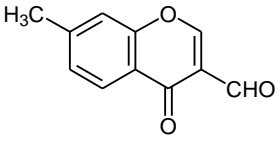
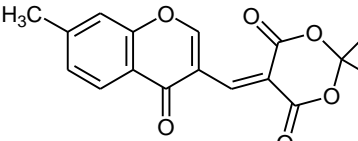
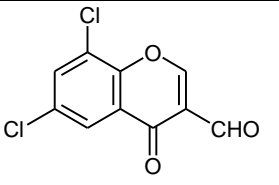
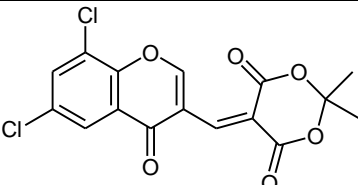
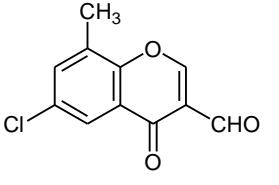
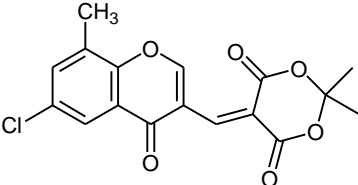
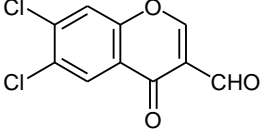
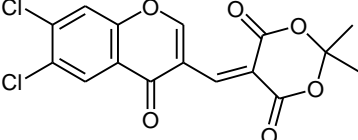
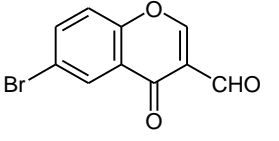
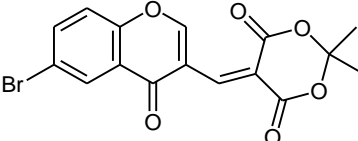
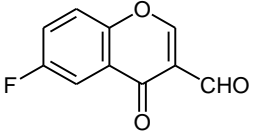
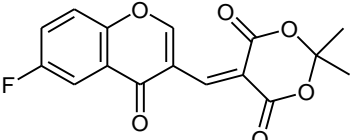
Table 1. Standardized the reaction condition for the synthesis of 2,2-dimethyl-5-[(4-oxo-4H-chromen-3-yl)methylene]-1,3-dioxane-4,6-dione 3a^a.

Entry	Reagent	Solvent	Time [min]	Yield [%] ^b
1	CdCl_2	EtOH	30	89
2	CdCl_2	MeOH	20	86
3	CdCl_2	H_2O	10	93

^a1a (1 mmol) treated with Meldrum's acid (1 mmol) and CdCl_2 (2 mol%) under different solvents at ambient temperature; ^bIsolated yields

Table 2. Knoevenagel condensation of 4-oxo-4H-benzopyran-3-carbaldehydes with Meldrum's acid in presence of CdCl_2 in water at room temperature

Entry	Ar	Product	Time (min)	Yield (%) ^a	M.p.(°C)	
					Found	Reported[6]
3a			25	93	181-183	182

3b			15	92	197-199	198
3c			20	87	184-186	186
3d			15	91	178-180	180
3e			10	89	198-200	200
3f			15	92	240-242	242
3g			15	95	202-204	205
3h			10	96	200-202	-

^aIsolated yields based upon starting aldehyde.

3. RESULTS AND DISCUSSION

In continuation our development of novel synthetic methodologies [7], herein, we would like to report a simple, efficient and green methodology for the synthesis of 2,2-dimethyl-5-[(4-oxo-4H-chromen-3-yl)methylene]-1,3-dioxane-4,6-diones. The synthetic route has been shown in Scheme 1.

In search for the best experimental condition, the reaction of 4-oxo-(4H)-1-benzopyran-3-carbaldehyde **1a** with Meldrum's acid in the presence of cadmium chloride at room temperature has been considered as the standard model reaction.

To study the effect of the different solvents on synthesis of 2,2-dimethyl-5-[(4-oxo-4H-chromen-3-yl)methylene]-1,3-dioxane-4,6-dione **3a** and results are summarized in Table 1. We used different solvents like EtOH, MeOH and water at room temperature. Surprisingly, water the unique solvent gave excellent yield of the product **3a** (Table 1, entry 3). These results suggest that water is the best solvent for synthesis of 2,2-dimethyl-5-[(4-oxo-4H-chromen-3-yl)methylene]-1,3-dioxane-4,6-dione. The best result was obtained by carrying out the reaction with 1:1 mol ratios of 4-oxo-(4H)-1-benzopyran-3-carbaldehyde **1a**: Meldrum's acid

and 2 mol% of CdCl_2 in water at room temperature, this condition 2,2-dimethyl-5-((4-oxo-4H-chromen-3-yl)methylene)-1,3-dioxane-4,6-dione 3a was obtained 93% yield after 25 min (Table 2, entry 1). The same reaction was carried out in the absence of catalyst, which resulted in 44% yield after 1h reaction time

The standard model reaction proceeded smoothly and was completed within 25 min of reaction time and 93 % yield. We were encouraged by the results obtained with model reaction. In a similar fashion, we have taken different heteroaryl aldehydes containing electron-withdrawing or electron-donating compounds with Meldrum's acid. They all gave the expected results with good yields in short reaction times.

We have developed a newer route for the Knoevenagel condensation of heteroaryl aldehydes with active methylene compound in presence of CdCl_2 in water medium at room temperature with constant stirring (Table 2). All the reactions were carried out at room temperature with constant stirring i.e. using mild reaction conditions. In this methodology, the products are isolated in pure form by simple filtration and as a result of which yield losses are avoided.

4. CONCLUSION

We have developed a novel and green methodology for the synthesis of 2, 2-dimethyl-5- [(4-oxo-4H-chromen-3-yl) methylene]-1, 3-dioxane-4, 6-diones from the condensation of substituted 4-oxo-4H-benzopyran-3-carbaldehyde with Meldrum's acid in presence of cadmium chloride in water at room temperature. The major merits offered by this methodology are mild reaction conditions, simple work-up procedure, cleaner reactions, short reaction times without phase transfer catalyst (PTC) and excellent yield of products. Moreover, the catalyst used is easily available, inexpensive, non-toxic, eco-friendly and water was chosen as a unique solvent, which makes the reaction convenient, more economic and environmentally benign.

REFERENCES

- [1] (a) N.Sachan, S. S.Kadamand V. M.Kulkarni *Ind. J. Hetero. Chem.* 17(2007) 57; (b) R. S.Mahalle, P. D.Netankar, S.P.Bondge andR. A.Mane *Green Chem. Lett. Rev.* 1(2008) 103.
- [2] H.McNab *Chem. Soc. Rev.* 7(1978)345.
- [3] W. H.Gerwick, A.Lopez, G.D.Van Duyne, J. Clardy, W.Ortiz and A.Buez *Tetrahedron Lett.* 270 (1979)1986.
- [4] (a) S. S. Pawar, M. S. Shingare and S. N. Thore *Lett. Org. Chem.* 4 (2007)486; (b) Y. Ren and C. Cai *Catal. Lett.* 118 (2007) 134;
- [5] (a) K. F. Shelke, A. D. Badar, S. S. Idhole, J. B. Devhade *International J.Universal Sci. and Tech.*, 03, (2018), 289.(b) B Sammaiah, D Sumalatha, G.S. Satyanarayana, ReddyM. Rajeswari and L.N. SharadaInte. J. Industrial Chem.3, 11 (2012); (c)G. Venkateshwarlu, A. Premalatha, K. C. Rajanna and P. K. Saiprakash, *Synth. Commu.*, 39, 4479(2009)
- [6] S. S.Shindalkar, B. R. Madje andM. S.Shingare *Ind. J. Chem. Sec.* 45B(2006)2571.
- [7] (a) K.F. Shelke, S.B. Sapkal, B. R. Madje, B. B. Shingate and M. S. Shingare *Bull. Catal. Soci. Ind.* 8 (2009)30; (b) K. F. Shelke, S. B. Sapkal, G. K.Kakade, S. A.Sadaphal, B. B.Shingate andM. S. Shingare, *Green Chem. Lett. Revi.*3(2010) 17;(c) K. F.Shelke, S. B.Sapkal andM. S. Shingare *Chin. Chem. Lett.*20 (2009) 283; (d) K. F.Shelke, S. B.Sapkal, , S. S.Sonar, B. R.Madje, B. B.Shingate and M. S.Shingare, *Bull. Korean Chem. Soc.* 30(2009) 1057; (e)) K. F Shelke, S. B Sapkal, N. V.Shitole, B. B.Shingate andM. S. Shingare, *Org. Commun.*2(2009)11.



STUDIES ON SURFACE PLASMON RESONANCE IN CHEMICALLY SYNTHESIZED CONDUCTING POLYTHIOPHENE

N. S.Wadatkar* and S. A.Waghuley

***Department of Physics, Government Polytechnic, Amravati 444603, India.
Department of Physics, Sant Gadge Baba Amravati University, Amravati 444602, India.
*Corresponding author E-mail: nswadatkar81@gmail.com**

ABSTRACT :

In the present work, we studied the surface plasmon resonance in one pot chemically synthesized conducting polythiophene (PTh) using oxidant anhydrous $FeCl_3$. The surface morphology of prepared samples were analyzed through FE-SEM, which shows irregular structure and spongy amorphous morphology. The optical transmission spectra of chemically synthesized PTh samples were recorded by using UV-Vis spectroscopy. The surface plasmon resonance of PTh samples was studied in 200-1100 nm using UV-Vis analysis.

KEYWORDS : Chemical polymerization; conducting polythiophene; surface plasmon resonance.

1. INTRODUCTION

Among the conducting polymers, polythiophene (PTh) is one of the most highly researched polymeric material because of its extraordinarily electronic optical properties, good processability, environmental stability and ease of synthesis [1-4]. It is in fact also the most frequently used conducting polymer incorporated with various carbon materials [5, 6]. The conjugated conducting polymers are well-known for their excellent electrical conductivities in oxidized (doped) state. The recent development in processable conducting polymers has opened the way for large-scale industrial applications.

In recent years, a lot of advancement has taken place in the development of intrinsically conducting polymers such as polyaniline (PANI), polythiophene (PTh), polypyrrole (PPy) and their derivatives due to their interesting electrical, chemical and physical properties [7]. In addition the conductivity of these materials can be controlled from conducting to insulating range by using different routes of polymerization as well as its surface charge characteristics can easily be modified by changing the dopant species in the material during synthesis [8,9]. Usually, polymerization can be carried out by electrochemical or chemical processes, which provide films with different morphologies and consequently slightly different chemical and physical properties [10]. Now days, these conducting polymers have been widely used as effective materials for the detection of toxic, hazardous and flammable gases due to their ease of synthesis and low cost [11]. The most important advantage of these conducting polymer-based sensors is their room temperature operation and high sensitivity. Among these intrinsically conducting polymers, PTh and its derivatives have attracted considerable attention due to their good environmental and thermal stability, easy polymerization process and high electrical conductivity [12, 13]. PTh can be produced in bulk powder as well as in thin film form [14] and it found wide applications in various fields such as supercapacitors [15], field effect transistors [16], light emitting diodes [17], photoconductive and photovoltaic devices and optical modulator devices [18]. PThs have also found applications in gas sensor field [7]. Soluble PTh derivatives can provide high sensitivity to certain gases, such as NO_2 at small concentration [19] as well as it has been reported that, PTh film showed gas response to ammonia, trimethylamine, acetone, alcohol and toluene at room temperature [7]. Wadatkar *et al* [20] successfully studied the complex optical and thermal properties of chemically as-synthesized

conducting polythiophene. Also Wadatkar *et al* [21] have been successfully synthesized the conducting polyindole by chemical oxidative polymerization using oxidant FeCl_3 in aqueous solution.

In the present study, samples were synthesized by using chemical oxidative polymerization method with anhydrous ferric chloride as an oxidant in deionised water. During polymerization, different concentration of FeCl_3 was taken. Prepared samples were characterized through FE-SEM and UV-Vis spectroscopy.

2. EXPERIMENTAL

Thiophene monomers, anhydrous iron (III) chloride (FeCl_3) from SD Fine Chemicals (AR-grade) were used in the present study. The thiophene monomer was used as received for synthesis of PTh. The sample was synthesized at room temperature (303 K) by mixing thiophene with FeCl_3 in deionised water. H_2O_2 was used to enhance the rate of reaction and also yield. After the rigorous stirring, drop-by-drop monomers was added into the solution. The preliminary polymerization process was identified by the colour change (brown) of the reaction mixture. The polymerization process was allowed to constant stirring for 8 hrs with a magnetic stirrer at 30 °C. The resulting precipitate was collected by vacuum filtration using cellulose nitrate filter papers. The precipitate was washed with copious amounts of triply distilled water until the washings were clear and then kept for overnight at room temperature. Subsequent to this samples were sintered at 60 °C for 30 min. In this way, two samples of PTh were synthesized with different stoichiometric ratios of thiophene and FeCl_3 as (90:10) and (80:20) wt. % [22].

3. RESULTS AND DISCUSSION

3.1 FE-SEM

The morphology and structural features of the material report from FE-SEM (JEOL JSM-6360). The surface morphology of PTh powder samples with stoichiometric ratio of thiophene and FeCl_3 as (90:10) and (80:20) wt. % were analyzed by FE-SEM and the micrograph is displayed in figure 1(a-b). The FE-SEM micrograph represents the non-porous and non-uniform structure containing macro-granular structure formed by the aggregation of small globular structures. The nature of particles has irregular in structure which reflects definite amorphous morphology. The micrograph depicts the presence of aggregation up to some extent as well as an agglomeration of particles.

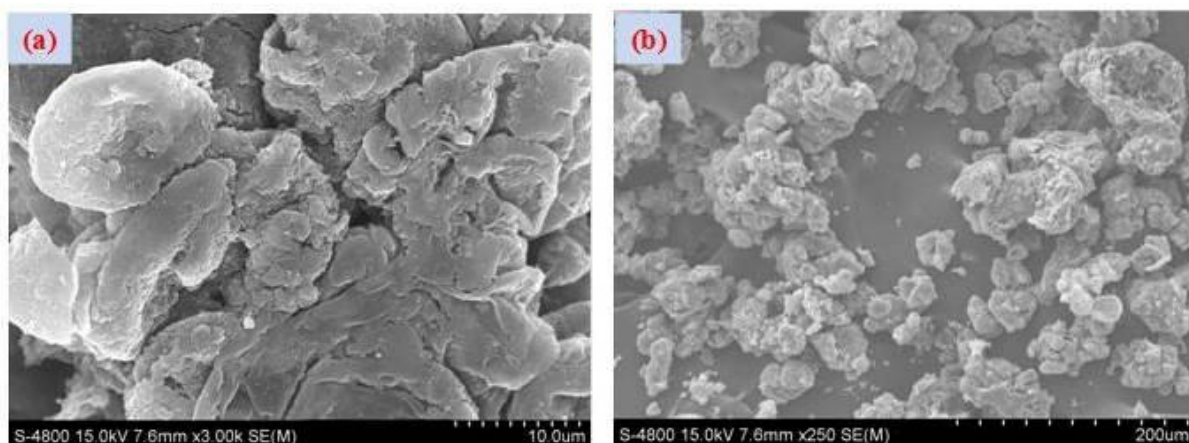


Fig. 1. FE-SEM micrograph of PTh with stoichiometric ratio of thiophene and FeCl_3 as (90:10) and (80:20) wt. %.

3.2 UV-Vis Spectra

UV-Vis absorption spectrophotometer is frequently used to investigate the surface plasmon resonance phenomenon. Figure 2 (a-b) shows the UV-Vis spectra of PTh samples synthesized with different stoichiometric ratios of thiophene and FeCl_3 as (90:10) and (80:20) wt. %. In this case, the transmission observed in the range 200-1100 nm. The transmission peaks of PTh samples are listed in table 1. The

collective oscillation frequency of conduction electron is termed as plasmon's frequency. The characteristic frequency of plasmon's is given by equation (1) [23].

$$\omega_p = (Ne^2/m_e)^{1/2} \quad (1)$$

where, ω_p is the plasma frequency, N is the conduction electron density, e is the charge on electron, m_e is the electron effective mass and ϵ_0 is the vacuum dielectric permittivity.

In the present work, plasmon frequency found to be increased with decrease in transmission wavelength. Also, the conduction electron density increases with decrease in transmission wavelength. According to the Fermi liquid model, plasmon can be satisfactorily described as a negative charged electron cloud displaced from its equilibrium position around the lattice made of positively charged ions, in analogy to factual plasma.

Table1. Values of Transmission wavelength, plasmon frequency and conduction electron density.

Sample (wt. %)	Transmission Wavelength (nm)	Plasmon frequency (ω_p) (MHz)	Conduction electron density (N) (m^{-3})
S ₁	276	0.1089	2.0137×10^{34}
S ₂	274	0.1094	2.0174×10^{34}

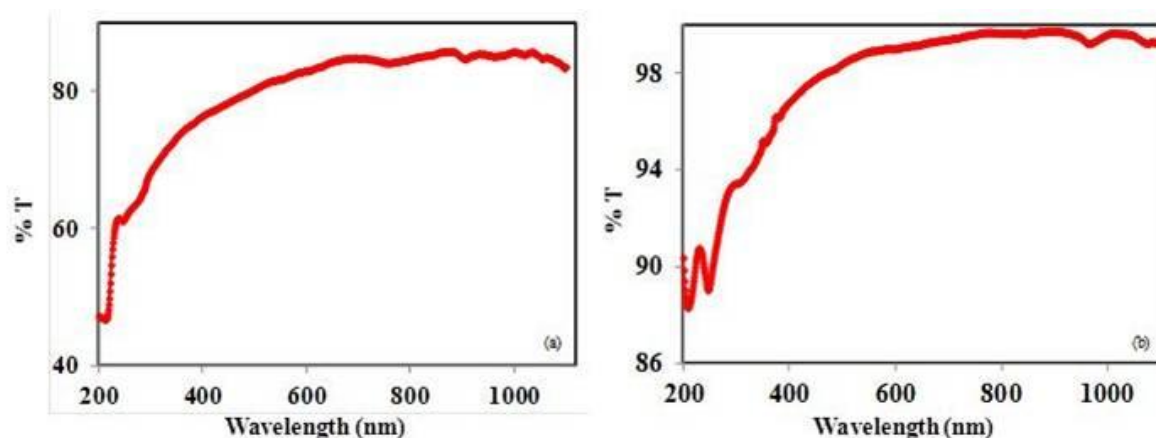


Fig. 2. UV-Vis spectra of PTh with stoichiometric ratio of thiophene and FeCl₃ as (a) (90:10) and (b) (80:20) wt. %.

4. CONCLUSIONS

In the summary of present work, the samples were synthesized by using chemical oxidative polymerization method with anhydrous FeCl₃ as an oxidant in aqueous medium at room temperature. The amorphous nature of as-synthesized material confirmed through FE-SEM analysis. The UV-Vis is a very simple technique to study the surface plasmon resonance. The characteristic frequencies of plasmon resonance in PTh were found to be increase with decrease in transmission wavelength. The conduction electron density is easily computed from this method.

ACKNOWLEDGEMENT

Authors are thankful to Head, Department of Physics Sant Gadge Baba Amravati University, Amravati for providing necessary facilities.

REFERENCES

- [1] C. Zhan, G. Yu, Y. Lu, L. Wang, E. Wujcik, S. Wei, Conductive Polymer Nanocomposites: A Critical Review of Modern Advanced Devices. *J. Mater. Chem. C*, 5 (2017) 1569-1585.
- [2] H. S. Nalwa, Handbook of Organic Conductive Molecules and Polymer (John Wiley & Sons, New York, 1997).
- [3] N.S. Wadatkar, S.A. Waghuley, Studies on properties of as-synthesized conducting polythiophene through aqueous chemical route. *J. Mat. Sci.: Mat. Elec.*, 27 (10), 10573-10581.
- [4] R.S. Bobade, S.V. Pakade (Yawale), S.P. Yawale, Electrical investigation of polythiophene–poly(vinyl acetate) composite films via VTF and impedance spectroscopy. *J. Non-Cryst. Solids*, 355 (2009) 2410–2414.
- [5] V.C. Gonçalves, M. Ferreira, C.A. Olivati, M.R. Cardoso, C.R. Mendonça, D.T. Balogh, Optical, electrical, and thermochromic properties of polyazothiophene Langmuir-Blodgett films. *Colloid. Polym. Sci.*, 286 (2008) 1395-1401.
- [7] X. Ma, G. Li, H. Xu, M. Wang, H. Chen, Preparation of polythiophene composite film by in situ polymerization at room temperature and its gas response studies, *Thin Solid Films*, 515 (2006) 2700-2704.
- [8] H. Yan, L. Zhang, J. Shen, Z. Chen, G. Shi, B. Zhang, Synthesis, property and field emission behaviour of amorphous polypyrrole nano wires. *Nanotech.*, 17(2006) 3446-3450.
- [9] H.K. Jun, Y.S. Hoh, B.S. Lee, S.T. Lee, J.O. Lim, D.D. Lee, J.S. Huh, Electrical properties of polypyrrole gas sensors fabricated under various pre-treatment conditions, *Sens. Actuators B*, 96 (2003) 576-581.
- [10] B. Adhikari, S. Majumdar, Polymers in sensor applications, *Prog. Polym. Sci.*, 29 (2004) 699-766.
- [11] K. Potje-Kamloth, Chemical gas sensors based on organic semiconductor polypyrrole, *Crit. Rev. Anal. Chem.*, 32 (2) (2002) 121-140.
- [12] M.J. Marsella, P.J. Carroll, T.M. Swager, Design of chemoresistive sensory materials: polythiophene-based pseudo polyrotaxanes, *J. Am. Chem. Soc.*, 117 (1995) 9832-9841.
- [13] M. Mastragostino, C. Arbizzani, F. Sovai, Polymer based supercapacitor, *J. Power Sourc.*, 97 (2001) 812-815.
- [14] J. Zhang, S. Wang, Y. Wang, Y. Wang, B. Zhu, H. Xia, X. Guo, S. Zhang, W. Huang, S.Wu, NO₂ sensing performance of SnO₂ hollow-sphere sensor, *Sens. Actuators, B* 135 (2009) 610–617.
- [15] A. Laforgue, P. Simon, C. Sarrazin, J.F. Fauvarque, Polythiophene based super-capacitors, *J. Power Sourc.*, 80 (1999) 142-148.
- [16] D.H. Kim, Y.D. Park, Y. Jang, H. Yang, Y.H. Kim, K. Cho, Enhancement of field effect mobility due to surface mediated molecular ordering in regioregular polythiophene thin film transistors, *Adv. Funct. Mater.*, 15 (2005) 77-82.
- [17] N.S. Sariciftci, D. Braun, C. Zhang, I.V. Srdanov, A.J. Heeger, G. Stucky, F. Wudl, Semiconducting polymer buck minster fullerene heterojunctions: diodes, photodiodes and photovoltaic cells, *Appl. Phys. Lett.*, 62 (1993) 585-587.
- [18] F. Bloisi, A. Cassinese, R. Papa, L. Vicari, V. Califano, Matrix-assisted pulsed laserevaporation of polythiophene films, *Thin Solid Films* 516 (2008) 1594-1598.
- [19] S.T. Navale, A.T. Mane, G.D. Khuspe, M.A. Chougule, V.B. Patil, Room temperature NO₂ sensing properties of polythiophene films. *Synth. Met.*, 195 (2014) 228-233.
- [20] N.S. Wadatkar, S.A. Waghuley, Complex Optical and Thermal Studies on As-Synthesized Conducting Polythiophene. *Journal of Electronic Materials*, (2019). <https://doi.org/10.1007/s11664-019-06991-4>.
- [21] N.S. Wadatkar, S.A. Waghuley, A novel studies on electrical behaviour of chemically synthesized conducting polyindole. *Indian J. Phys.*, 92 (12) (2018) 1551-1559.
- [22] N.S. Wadatkar, S.A. Waghuley, Optical study of chemically synthesized conducting polythiophene using UV-Vis spectroscopy, *Macromol. Symp.*, 362 (2016) 129-131.
- [23] C. Kittel, Introduction to Solid State Physics, (John Wiley & Sons, New York, 1996).



SYNTHESIS, STRUCTURAL AND OPTICAL PROPERTIES OF DOUBLE-PEROVSKITE $\text{Sr}_2\text{FeNiO}_6$ NANO COMPOSITES

A. A. Jadhao¹, V. G. Pahurkar^{1a}, P. R. Padole², G. N. Chaudhari^{2a*}

¹Department of Physics, Prof. Ram Meghe Institute of Research & Technology, Badnera (M.S.), India-444701

²Nanotechnol. Research Laboratory, Department of Chemistry, Shri Shivaji Science College, Amravati (M.S), India-444603
E-mail: cgnroa@yahoo.com

ABSTRACT :

The doubled perovskite $\text{Sr}_2\text{FeNiO}_6$ nanocomposites were synthesized using simple sol-gel citrate method. As-synthesized $\text{Sr}_2\text{FeNiO}_6$ nanocomposites were characterized using ultraviolet visible (UV-vis) spectroscopy for the absorption study. The surface morphology was studied with field emission scanning electron microscopy (FE-SEM). Moreover, the compositional feature of $\text{Sr}_2\text{FeNiO}_6$ nanocomposites was investigated through energy dispersive X-ray spectroscopy (EDS) analysis.

KEYWORDS : $\text{Sr}_2\text{FeNiO}_6$ Nanocomposites; Sol-gel; Double-Perovskite; Nanomaterial.

1. INTRODUCTION

Perovskite and Double-perovskite materials have various alluring chemical and physical properties such as thermal, electrical, optical, magnetic and biological [1-8]. These materials can show superconductivity along with all magnetic properties like antiferromagnetic to ferri- and ferromagnetic, ionic conductivity, photoactivity and can behave like catalytic agent. These materials have wide applications in the fields such as electronics, sensors, magnetic memory components, fuel cells, and solar cells [9-12].

Nowadays, many researchers are interested in double-perovskite oxides that consist of transition metals, due to their diverse applications in material science research as mentioned above. The double-perovskite oxide compounds are synthesized at high temperatures and have a very high flexibility in crystal structure and chemical composition [13].

By arranging two cations such as B' and B'' on the B -site in a simple perovskite ABO_3 ; double-perovskite compounds with chemical formula of $\text{A}_2\text{B}'\text{B}''\text{O}_{6-\delta}$ can be derived. In this formula A stands for alkaline earth metal ions (like Ba, Ca, Sr), and B' , B'' are transition metal ions (like $B' = \text{Co, Fe, Ni, Cr, etc.}$ and $B'' = \text{W, Mo, Sb, etc.}$). Ideally, the framework of double-perovskite structure form is constructed by corner-shared $B'\text{O}_6$ and $B''\text{O}_6$ octahedra in the lattices [1].

In the present research article, as-synthesized $\text{Sr}_2\text{FeNiO}_6$ double perovskite nanocomposites by sol-gel citrate method have been reported. The optical property i.e. absorption and energy band gap of these nanocomposites were studied using UV-Vis spectroscopy. The surface morphological study of prepared sample was studied using field emission scanning electron microscopy (FE-SEM) and elemental compositional study was done using Energy Dispersive X-ray Spectroscopy (EDS). The results are reported.

2. EXPERIMENTAL

2.1 Materials and methods

All the chemicals used for the synthesis of $\text{Sr}_2\text{FeNiO}_6$ double-perovskite nanocomposites i.e. Strontium nitrate [$\text{Sr}(\text{NO}_3)_2$], Ferric nitrate [$\text{Fe}(\text{NO}_3)_3 \cdot 9\text{H}_2\text{O}$] and Nickel Nitrate [$\text{Ni}(\text{NO}_3)_2 \cdot 6\text{H}_2\text{O}$] were of AR-grade and procured from sd Fine chemicals, India.

The $\text{Sr}_2\text{FeNiO}_6$ double perovskite nanocomposites were prepared by using sol-gel citrate method. The stoichiometric mixture of Strontium nitrate [$\text{Sr}(\text{NO}_3)_2$], Ferric nitrate [$\text{Fe}(\text{NO}_3)_3 \cdot 9\text{H}_2\text{O}$] and Nickel nitrate [$\text{Ni}(\text{NO}_3)_2 \cdot 6\text{H}_2\text{O}$] magnetically stirred with citric acid as a chelating agent and ethanol at 80°C for 3 hrs to get homogeneous mixture. Then it was further heated at about 130° for 12 hrs in pressure vessel to get gel precursor. Then it was subjected to 3hrs heat treatment at 350°C in muffle furnace. After heating it was fine milled to get powder. The dried powder sample was calcined in the range of $350\text{-}650^\circ\text{C}$ in order to improve the crystallinity of material.

2.2 Characterization

The optical study of as-synthesized $\text{Sr}_2\text{FeNiO}_6$ nanocomposite was studied using StellarNet UV-vis spectrophotometer, (BLK-CSR, StellarNet, USA). Surface morphology of prepared nanocomposites has been investigated using Field emission scanning electron microscopy (FE-SEM) (S-4800, Hitachi, Japan). The composition was determined with Energy Dispersive X-ray Spectroscopy (EDS) attached with FE-SEM (Bruker, Japan).

3. RESULTS AND DISCUSSION

3.1 UV-vis spectroscopic study

Fig. 1 shows the optical absorption spectrum of $\text{Sr}_2\text{FeNiO}_6$ nanocomposites material in UV-vis region. It shows one broad absorption peak at about $\sim 525\text{ nm}$ in the wavelength ranging, which decides the prepared sample is in nano-range. The rough energy value for band-gap energy (E_g) of the prepared nanocomposite sample was determined using the equation; $E_g = 1240/\lambda_g$. Therefore, the band energy of as-synthesized $\text{Sr}_2\text{FeNiO}_6$ nanocomposite is found to be $\sim 2.4\text{ eV}$.

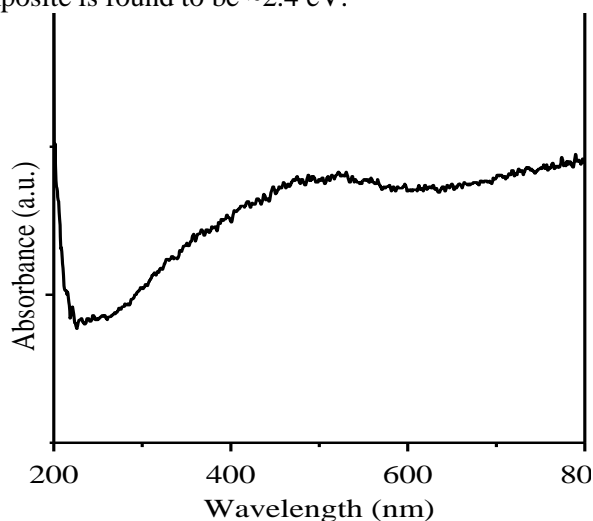


Fig. 1. UV-vis spectroscopy of $\text{Sr}_2\text{FeNiO}_6$ nanocomposites.

3.2 FE-SEM study

Fig. 2 shows the FE-SEM image of $\text{Sr}_2\text{FeNiO}_6$ nanocomposites, which was used to investigate surface morphology of prepared sample. This image depicts the uniform agglomeration of the $\text{Sr}_2\text{FeNiO}_6$ nanocomposites.

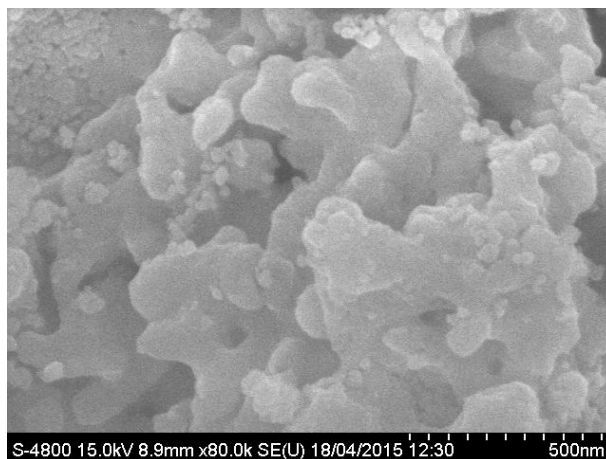


Fig. 2. FE-SEM image of $\text{Sr}_2\text{FeNiO}_6$ nanocomposites.

3.3 EDS study

Fig. 3 depicts the EDS analysis of as-synthesized $\text{Sr}_2\text{FeNiO}_6$ nanocomposite, in order to determine the chemical composition present in the sample to support the structure of $\text{Sr}_2\text{FeNiO}_6$ nanocomposite. It shows that percentage of various cations in as-synthesized nanocomposites was found to be approximately correct as compared to the composition ratio.

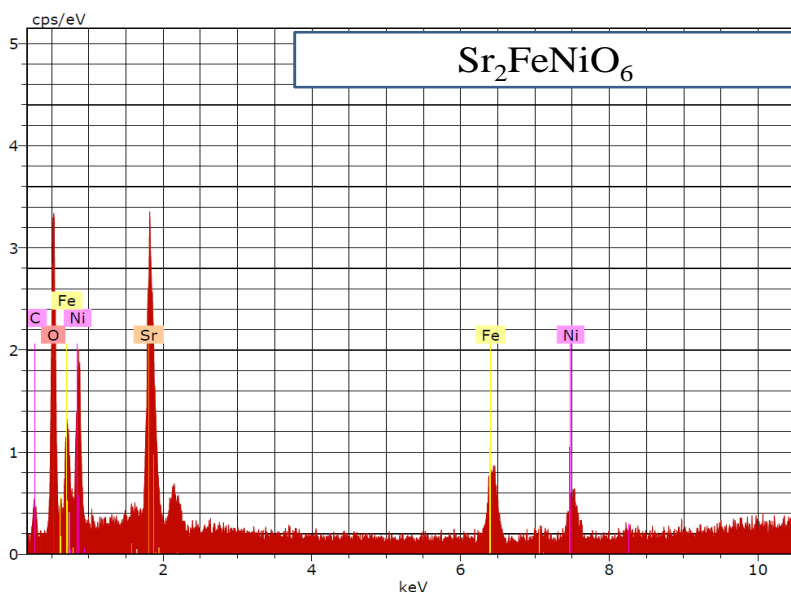


Fig. 3. EDS pattern of $\text{Sr}_2\text{FeNiO}_6$ nanocomposites.

CONCLUSIONS

The doubled-pervoskite $\text{Sr}_2\text{FeNiO}_6$ nanocomposite were synthesized using simple sol-gel citrate method. UV-vis absorption study showed the broad absorption peak at $\sim 525\text{nm}$, which has the good agreement with the nanomaterial. The theoretical energy band-gap of the nanocomposite was found to be 2.4 eV. The $\text{Sr}_2\text{FeNiO}_6$ nanocomposites were found uniform with some agglomeration. EDS measurement shows that all the elemental compositions are present in the prepared samples as per the ratio of compositional formula. The present doubled-pervoskite $\text{Sr}_2\text{FeNiO}_6$ nanocomposites may be useful for the various emerging fields such as solid oxide fuel cells, photocatalysis, sensors, biological activity, etc.

REFERENCES

- [1] L. Xu, Y. Wan, H. Xie, Y. Huang, L. Yang, L. Qin, H. J. Seo, Synthesis, surface structure and optical properties of double perovskite $\text{Sr}_2\text{NiMoO}_6$ nanoparticles, *Applied Surface Science*; 2017, 169-4332(16)31553-7.
- [2] D. Marrero-Lopez, J. Pena-Martinez, J.C. Ruiz-Morales, M. Gabas, P. Nunez, M.A.G. Aranda, J.R. Ramos-Barrado, Redox behavior, chemical compatibility and electrochemical performance of $\text{Sr}_2\text{MgMoO}_{6-\delta}$ as SOFC anode, *Solid. State Ion.* 180 (2010) 1672-1682.
- [3] M. Pichler, D. Pergolesi, S. Landsmann, V. Chawla, J. Michler, M. Döbeli, A. Wokaun, T. Lippert, TiN-buffered substrates for photoelectrochemical measurements of oxynitride thin films, *Appl. Surf. Sci.* 369 (2016) 67-75
- [4] J. Wang, C. Huang, X. Chen, H. Zhang, Z. Li, Z. Zou, Photocatalytic CO_2 reduction of BaCeO_3 with 4f configuration electrons, *Appl. Surf. Sci.* 358, (2015) 463-467
- [5] S. Yang, D. Xu, B. Chen, B. Luo, X. Yan, L. Xiao, W. Shi, Synthesis and visible-light-driven photocatalytic activity of p-n heterojunction $\text{Ag}_2\text{O}/\text{NaTaO}_3$ nanocubes, *Appl. Surf. Sci.* 383, (2016) 214-221
- [6] S. Zhao, L.G. Gao, C.F. Lan, S.S. Pandey, S.Z. Hayase, T.L. Ma; First principles analysis of oxygen vacancy formation and migration in Sr_2BMoO_6 (B = Mg, Co, Ni), *RSC Adv.* 6 (2016) 31968-31975.
- [7] X. Li, J. Yu, J. Low, Y. Fang, J. Xiaoc, X. Chen; Engineering heterogeneous semiconductors for solar water splitting. *J. Mater. Chem. A*, 3 (2015) 2485-2534
- [8] E. Grabowska; Selected perovskite oxides: Characterization, preparation and photocatalytic properties-A review, *Applied Catalysis B: Environmental*, 186 (2016) 97-126
- [9] M. A. Haddouch, A. Abbassi, Y. Aharbil, H. Labrim, Y. Tamraoui, F. Mirinioui, A. Benyoussef, L. Laanab, S. Benmokhtar; *Journal of Applied Surfaces and Interfaces* 1 (1-3) (2017) 1-6
- [10] K.I. Kobayashi, T. Kimura, H. Sawada, K. Terakura, Y. Tokura; *Nature* 395 (1998) 677-680.
- [11] R.J. Cava, B. Batlogg, J.J. Krajewski, R. Farrow, L.W. Rupp, A.E. White, K. Short, W.F. Peck, T. Kometani; *Nature* 332(1988) 814 - 816.
- [12] J.B. Goodenough, J.M. Longo; *Physics.: Magnetic and Other Properties of Oxides and Related Compounds, Part a*, Springer, Berlin, 1970, (4) 126-367.
- [13] Y. A. Alsabab, M. S. AlSalhi, A. A. Elbadawi, E. M. Mustafa, *Materials* 2017, 10, 469-480.



RECENT TRENDS IN NANOTECHNOLOGY AND ITS APPLICATION IN MEDICINE

H. N. Khan , S. B. Pathan , S. T. Kalyankasture , S. S. More
Department of Quality Assurance SSS Indira College of Pharmacy, Vishnupuri,
Nanded- 431606 Maharashtra, India.

ABSTRACT :

The Health care Industry of today is focusing on developing minimally invasive techniques for diagnosis as well as treatment. Science and technology have always been the vitals of humans struggle, utilized exclusively for development of novel tools and products, ranging from micro to Nano size. Nanotechnology is subjected to inordinate progress in various forms especially in Healthcare. Development of various advanced Nano-device and Nano-materials results in establishment of most effective method for delivery of therapeutic for treatment of Ophthalmological, Pulmonary, Cardiovascular disease and more importantly in Cancer therapy. Nanotechnology is the future of advanced development. It is everything today from clothes to foods there are every sector in its range we should promote it more for our future and for more developments in our current life.

KEYWORDS : Nanotechnology, Pharmaceutical Nanosystem , Nanomedicine.

INTRODUCTION:-

Nanotechnology has generated a great deal of excitement and is being considered as the key technology of the 21st century. Nanotechnology is a rapidly developing field involving the interdisciplinary study of materials that covers a broad range of topics and is focused on controlling and exploiting the structure of matter on a large scale below 100 nanometers. It offers an unprecedented ability to study and manipulate molecular interactions at a sub-cellular level leading to the development of new strategies to treat human disease.¹

On December 29, 1959, Physicist Richard Feynman gave a radical lecture at an American Physical Society meeting at Caltech titled "There's Plenty of Room at the Bottom". This lecture was the birth of the idea and study of Nanotechnology.

In 1974, the term nanotechnology was used by Taniguchi for the first time. In 1986 First book on nanotechnology Engines of Creation published by K. Eric Drexler. First nano medicine book by R. Freitas "Nano medicine" was published in 1999 and in 2011 Era of molecular nano technology was started to study the nanotechnology products and processes that help to solve health problem.

Nanotechnology is manipulation of matter on an atomic, molecular and supramolecular scale, with at least one dimension sized from 1 to 100 nm and thus can be used for a broad range of applications and the creation of various types of Nano materials and Nano devices.²

There are two concepts commonly associated with nanotechnology:

- Positional assembly- helps to get the right molecular parts in the right places
- Massive parallelism-helps to keep the costs down.

PHARMACEUTICAL NANOSYSTEM

Pharmaceutical Nano system is a device that functions by means of Nano scale components.³

Nanosystem Applications

- Gold Nanoparticles - Targeted delivery of drugs to Tumors
- Nanowire - Electrical detection of single viruses and biomolecules.
- Carbon nanotubes -Tumortargeting,Blood glucose monitoring; sensors for DNA detection.
- Nanosphere- Polystyrene nanospheres used as vaccine carriers directing human dendritic cells, have been investigated for nasal vaccination.
- Nanobiosensors- Early diagnosis and detection of cancer.
- Nano device Bucky balls have been used to alter the allergy/ immune response. They prevent mast cells from releasing histamine into the blood and tissues, as these bind to free radicals better than any anti-oxidant available, such as vitamin E
- Nanotechnology in Drug Delivery
- Recent research has shown unprecedented development in the areas of Nanoscience, Nanophysics and nanotechnology. Nanomedicine plays an important role in the near future mainly in the fields of Science and technology and helpful for the betterment of life and a new era in the field of Medicine ⁴
- Nano medicine mainly involves nanoparticles to deliver or inject drugs, like heat, light or other substances to recognise some tumour related cells which causes cancers or carcinoma. Nano Particles are specifically made specifically inured in order to attract a diseased cell, which involves treatment of tumour related cells. This technique mainly reduces side effects to health cells and helpful for the easy detection of cancer ⁵
- For Instance nanoparticles are used to target the cancer cells but not healthy cells. Research is going on nano materials which are helpful for the easy detection of cancers, carcinomas sometimes they may cause deaths. Some of the companies or research organisation are taking permission from patient for the easy delivery ofnanomaterial's of and once if it is done they can directly use in cancer patients without any side effects. Many research groups, companies; organisations are conducting many trials in order to release the drug's safety into the cancer cells without causing any side effects to the patients.
- Researchers all over the world are developing a medically related nanoparticle that can be taken orally and which passes through the stomach lining and the intestines are released into the bloodstream. Many investigations are going on lab animals for example such as lab mice in which the drugs are delivered to a target cells .⁶

NANOMEDICINE

Nanomedicineis the process of diagnosing, treating and preventing the diseases to improve human health, using molecular tools and molecular knowledge of human body.

NANO MEDICINE FOR CORNEAL DISEASES

Nanomedicinefor treatment of ocular diseases are as follows

The nanospheres made by pullulan and polycaprolactone that contain ciprofloxacin coated on to contact lenses prevent eye infection caused due to Staphylococcus aureus and Pseudomonas aeruginosa.

For the treatment of ocular inflammation Nanoemulsions (NEs) Ex. Durezol (Alcon Laboratories, Fort Worth, TX, USA) is used.Nano eye-drops Ex.Nano Tears TF,Nano eye-drops utilising brinzolamide, a commercially available glaucoma treatment.⁷

Advantages

- Provide more reproducible and controlled release of the drugs
 - Solubilize both hydrophobic and hydrophilic drugs to improve the stability, half-life and therapeutic efficacy of the drug delivery
 - Increase potency and reduced side effects
 - Nano eye-drops were not toxic to the corneal epithelium after repeated administration for 1 week.
- Disadvantage
- High costs, discomfort to the patients

NANOROBOTS AS MEDICINE

In medical field Nanorobots is used as Nanomedicine.



Robert A. Freitas Jr designed nanorobots which is type of artificial blood

- i. Respirocytes- An artificial erythrocyte programmed to collect carbon monoxide and other poisonous gases from the body.
- ii. Microbivores - Digest and Absorb the pathogens in the blood stream
- iii. Clottocytes- Artificial mechanical platelet that would complete hemostasis in approximately 1 sec.

APPLICATIONS

1. Break blood clots
2. Break kidney stones
3. Destroy and remove Parasite from body
4. Used in treatment of Arteriosclerosis
5. In Dentistry Induces oral analgesia, desensitize tooth, manipulate the tissues to realign and straighten irregular set of teeth.

Delicate surgeries - Nanorobots could be soon used for performing micro surgery

Advantages of Nanorobots

- They help in performing painless and noninvasive surgeries.
- The initial cost of development is only high but batch processing reduces cost of manufacturing.
- The diagnosis and monitoring is continuous and done from inside of the body.
- They disassemble and get excreted after completion of task, if necessary..

Limitations of nanorobots

- Design of nanobots is very complicated and it is very costly
- Hard to interface and control externally.

OTHER NANODEVICES

Nanotech Detector for Heart Attacks

This technology involves tiny blood stream nanosensor chips that might sense the precursor of a heart attack. A person with nanosensor tiny chip might get a warning on their smartphone or another wireless device that they should immediately see their cardiologist. Nanosensors that detect heart attacks before they happen could save both lives and money. It is used for glucose detection in animal studies. Human trials should follow thereafter. The combination of a nanosensor and coupled smartphone could be used to track autoimmune disease and cancer.⁷



Dragonfly-Inspired Black Silicon Fights Off Bacteria

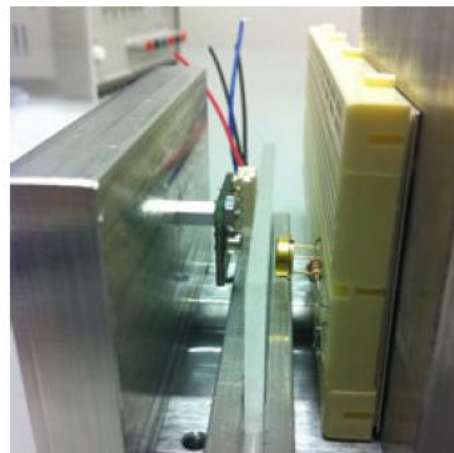
The scientists verify that the black silicon material proved to be effective against an array of Gram-negative and Gram positive bacteria as well as endospores. The researchers

confirm that the breakthrough is the first "physical bactericidal activity of black silicon or indeed for any hydrophilic surface.

Nanotech-Enabled Breathalyzer For Diabetics

In Western New England University Researchers have developed a nanotech-powered breathalyzer prototype that can detect acetone levels in the breath, which is theorized to correlate to blood glucose levels. The technology, if commercialized, could do away with the need for finger-prick-based testing of blood sugar. The breathalyzer prototype is roughly the size of a book. The researchers are working on shrinking the technology to yield a breathalyzer with a similar size to those used by police to detect blood alcohol content levels.

The Breathalyzer design is initially the size of a book which is developed by Western New England University researchers. Then further development is Electron Beam and Plasma Technology FEP which are actually working a breath-analyzing spectrometer that is so tiny it can fit into a mobile phone.⁸ These breath-analyzing spectrometer is developed by Scientists from the Technische Universität Dresden (Germany) and Fraunhofer.



CONCLUSION

Nanodevices and Nanomaterials for tissue repair and drug delivery is a medical application of nanotechnology in the treatment of human diseases.

Recent progress in nanotechnology to design and engineer nanoparticles is counterpoised to revolutionize the way we diagnose, monitor and treat corneal diseases. In ocular diseases Nanomedicines may have applications as a next-generation ophthalmic treatment.

in the field of medicine the Nanobots have many applications. When the severe side effects of the existing therapies are been considered, the nanorobots are found to be more innovative, supportive to the treatment and diagnosis of vital diseases exhibit strong potential to diagnose and treat various medical conditions like cancer, heart attack, diabetes, arteriosclerosis, kidney stones etc. allow us a personalized treatment. Nanotechnology significantly improve the quality of life of patients New possibilities in Nanomedicine also involve risks and raise sociological and ethical questions which must be analyzed and debated.

FUTURE SCOPE,

With each day, the advance in nanoscale actuation brings us close to a world of nanotechnology. In the mere future nanobots as nanomedicine would become integral part of medical field An exhaustive development effort could have a employed representation of the micro robot prepared within a year or two, and this would definitely progress the development of nanotechnology

The Figure shows the four research and development areas which will probably receive the greatest impetus from nanomedicine in the coming decades.

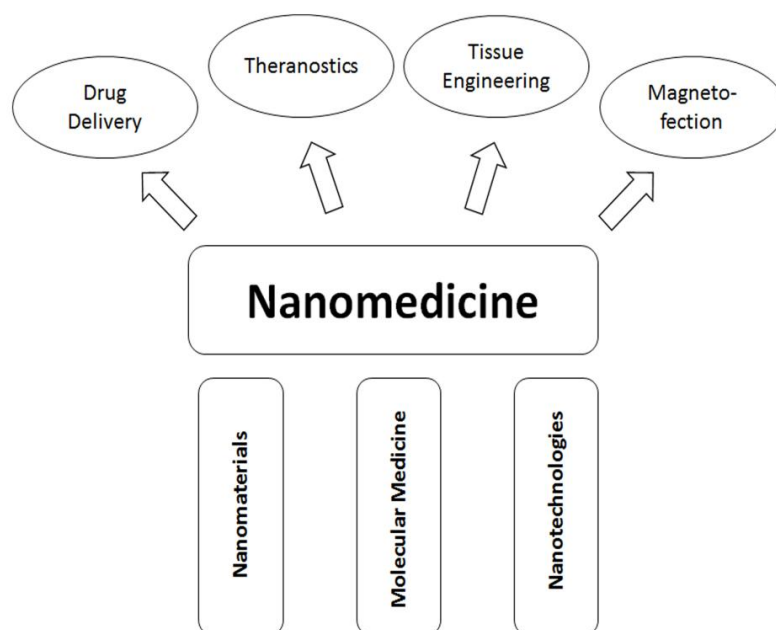


Figure - Future development of nanomedicine

Future applications of nanomedicine will include activity monitors, biochips, needle less injectors, insulin pumps, glucose monitoring devices and drug injecting systems, medical flow sensors and blood pressure. In future at its best it is hoped that nanomedical machines will cover up the deficiencies by replacing or improving the DNA molecules of body. What nanomedicine will be able to achieve in the future is beyond current imagination.

REFERENCES

1. Nikalje A.P., (2015) in their article described Nanotechnology and its Applications in Medicine. *Med chem* 5: 081-089.
2. Kuldeep P., (2012) reported Recent Advances in Nanotechnology *International Journal of Scientific & Engineering Research*, Volume 3, Issue:1-11.
3. Shyam S. Chaurasia (2015) Nanomedicine Approaches for Corneal Diseases *J. Funct. Biomater.*,6, 277-298
4. ApoorvaManjunath., (2014) reported The Promising Future in Medicine: Nanorobots, *Biomedical Science and Engineering*, , Vol. 2, No. 2, 42-47
5. Bhagyashree S. Durgaker., (2016) described Application of Nanorobots in Medical field *International Journal of Research in Communication Engineering*, Vol. 6, Special Issue, November 52-55 Application Nanorobot Adv N Disadv.
6. Mitra M (2017) Medical Nanobot for Cell and Tissue Repair. *Int Rob Auto J* 2(6): 00038.
7. Dones I, et al. (2016) Intrathecal Drug Delivery Therapy with Implantable Pump System in Refractory Cancer and Non-Cancer Pain. *J Pain Relief.*;5:004.
8. Patil J. (2016) Encapsulation Technology Opportunity to develop Novel Drug Delivery Systems. *J Pharmacovigil.*;4157.
9. Brian Buntz (2014) 10 Nanotech Breakthroughs You Should Know About (Updated) | MDDI Online By in R&D (/primary-keywords/rd-0):1-9



COMPARATIVE DIELECTRIC STUDY OF 2-PROPANOL-WATER AND GLYCEROL-WATER MIXTURES USING TDR

Nandkishor Bharose^{*1}, Satyajit Chavan^{#1}, Ashok Kumbharkhane^{*2}

R.B.Attal College, Georai,

[#]Department of physics, Adarsh College, Hingoli,
School of Physical Sciences, SRTM University Nanded.

¹satyajit.chavan@gmail.com

²akumbharkhane@yahoo.co.in

ABSTRACT :

Dielectric properties of 2-Propanol-water and glycerol-water mixtures have been studied in this paper. Time domain reflectometry(TDR) technique has been used in frequency range 10MHz to 20GHz to determine the dielectric parameters at room temperature. Relaxation time gives orientation relation between two mixtures. Dielectric constant, Kirkwood correlation factor, excess permittivity have been studied for molecular interaction variation between two mixtures.

KEYWORDS : 2-Propanol, glycerol, water, TDR, dielectric parameters.

I. INTRODUCTION

Isopropyl alcohol (2-Propanol) have formula $(\text{CH}_3)_2\text{CHOH}$ with molecular weight 60.10g.mol^{-1} . Glycol (G) have formula $[\text{C}_3\text{H}_5(\text{OH})_3]$ with molecular weight 92.09g.mol^{-1} . Glycerol (G) and 2-Propanol both have 2 carbon atoms and 8 hydrogen atoms only difference in Oxygen atoms, 2-Propanol have one and glycerol have three atoms resp. Alcohols-water mixture dielectric studies have been carried out to investigate hydrogen bond nature and molecular interaction between mixtures.[1-6] Both the liquids have industrial importance and also soluble in water. Both the liquids have difference in molecular weight which causes difference in their dielectric properties, in this paper we studied comparative differences of dielectric parameters of both of aqueous solutions.

II. EXPERIMENTAL TECHNIQUE

The dielectric permittivity of all alcohol-water mixtures were measured by TDR in the frequency range between 10 MHz to 20GHz. The Hewlett Packard HP54750 sampling oscilloscope with HP 5475A. A TDR plug in module has been used. A fast rising step voltage pulse of about 40ps rise time was propagated through a coaxial line system. SMA sample cell with 3.5mm outer diameter and 1.35mm effective Pin length was used. All measurements were done under open load conditions. The time window chosen for the measurements was kept at 5ns. First, the reflected pulse $R_1(t)$ and $R_x(t)$ without and with sample in the cell, respectively was recorded. The pulse Reflected through the sample $R_x(t)$ was compared with the reflected pulse without sample $R_1(t)$.

III. RESULT AND DISCUSSION

The complex permittivity spectra, $[\varepsilon^*(\omega) = \varepsilon'(\omega) - j\varepsilon''(\omega)]$ where, $\varepsilon'(\omega)$ is real component known as dielectric dispersion and $\varepsilon''(\omega)$ is imaginary component known as dielectric loss of given liquids. The dielectric relaxation parameters like static dielectric constant (ε_0), relaxation time (τ) and distribution

parameters (α and β) are obtained by the non-linear least squares method to the Havriliak-Negami expression [7]

$$\epsilon^*(\omega) = \epsilon_\infty + \frac{(\epsilon_0 - \epsilon_\infty)}{[1 + (j\omega\tau)^{1-\alpha}]^\beta} \quad (1)$$

With $\epsilon_0, \epsilon_\infty, \tau, \alpha$ and β are the fitting parameters. The equation includes the Cole-Cole ($\beta=1$), Davison-Cole ($\alpha=0$) and Debye ($\alpha=0, \beta=1$) relaxation model. The values of the errors are estimated by assuming 2% errors in the values of ϵ' and ϵ'' from the goodness of fit of the data with eq.(1).

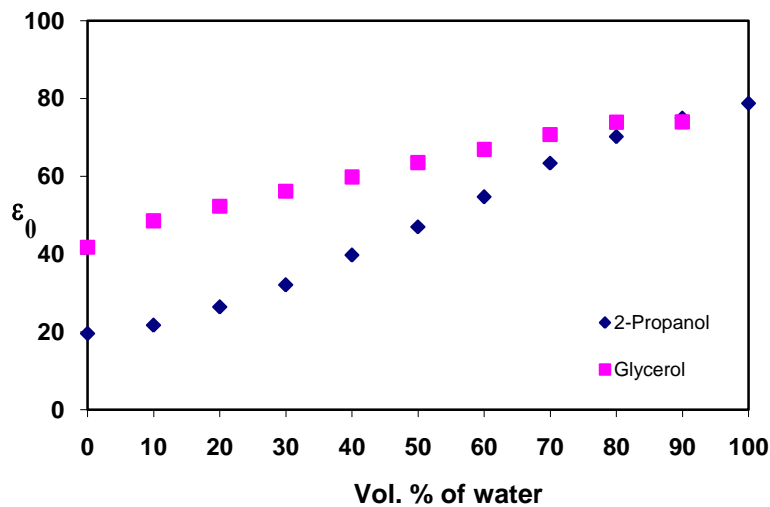


Fig.1. Static dielectric constant Vs Vol. % of water of 2-Propanol and Glycerol.

Variation of the static permittivity (ϵ_0) as a volume fraction of water concentration is shown in Fig.1. The static permittivity increases as the concentration of water in both the liquids 2-Propanol and Glycerol increases. The value of static dielectric constant of Glycerol is twice than that of 2-Propanol, this difference is only due to difference in their molecular weights.

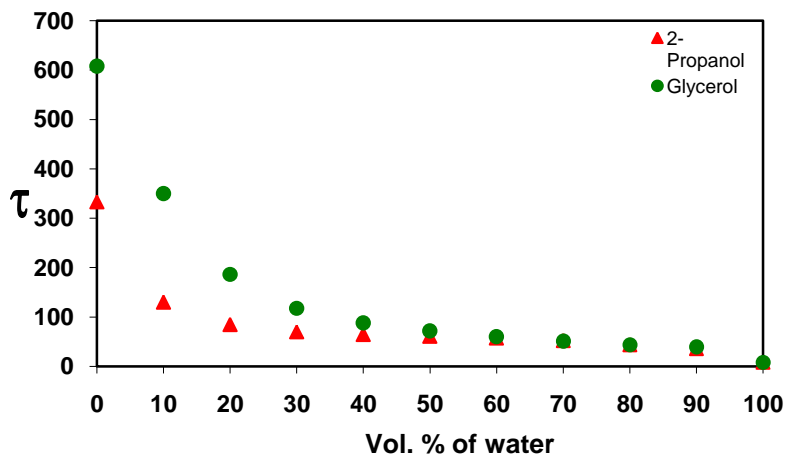


Fig.2. Relaxation time Vs Vol. % of water of 2-Propanol and Glycerol.

Variation of relaxation time (τ), as a volume fraction of water in 2-Propanol and Glycerol is shown in Fig.2. The relaxation time (τ) decreases as the concentration of water increases in both the mixtures. The relaxation time of 2-Propanol is smaller than the Glycerol. This difference in relaxation time is also due to difference in their molecular weights difference between them.

The Kirkwood correlation as determined from the dielectric constant gives information about collective orientation correlation between molecules.[8] The calculation of Kirkwood correlation factor 'g' provides information regarding the hindrance of molecular orientation by neighboring molecules. The deviation of 'g' from unity is a measure of degree of hindered relative molecular motion arising from short range intermolecular forces. When the molecules tend to direct themselves with parallel dipole moments, 'g' will be greater than unity. If the molecules prefer an ordering with anti parallel dipoles, 'g' will be smaller than unity.

For a mixture, the Kirkwood correlation factor 'g' can be expressed as follows:

$$\left[(\epsilon_{0i} - \epsilon_{\infty i}) (2\epsilon_{0i} + \epsilon_{\infty i}) / 9\epsilon_{0i} \right] = 4\pi/9kT \sum_{i=1}^2 g_i \rho_i \mu_i^2 \quad (2)$$

where $i=1,2$ represent water and 2-propanol or glycerol, respectively; μ_i is their dipole moment in gas phase, ρ_i is the density, k is the Boltzmann constant, T is the temperature, ϵ_{0i} and $\epsilon_{\infty i}$ are the static dielectric constant and dielectric constant at high frequency. 'g_i' is the Kirkwood correlation factor for the i^{th} liquid system.

The interpretation of the dielectric phenomena in terms of the Kirkwood correlation factor is very difficult for mixtures of associating compound.

(i) In the first model, we have assumed that the mixture can be represented by one correlation factor g^{eff} as follows:

$$\left[(\epsilon_{0m} - \epsilon_{\infty m}) (2\epsilon_{0m} + \epsilon_{\infty m}) / 9\epsilon_{0m} \right] = [4\pi/9kT] g^{\text{eff}} [\rho_m \mu_m^2] \quad (3)$$

To calculate g^{eff} values, we have taken dipole moment of 2-Propanol, Glycerol and water as 1.70D, 2.67D and 1.84D respectively. The value ($\epsilon_{\infty m}$) is taken as the square of the refractive index data. We believe that g^{eff} defined by eq.(3) is a reasonable measure of the molecular correlation. The observed value is greater than unity in water-2-Propanol and water-Glycerol mixtures, but Fig.5 shows that the values of water-2-Propanol and water-Glycerol mixtures are similar. The high values of g^{eff} indicate average parallel orientation of electric dipoles in a molecule. It can be seen that as water is added in 2-Propanol and Glycerol at regular steps in the mixture, the values of g^{eff} increases. The correlation factor is essentially connected to the total orientation polarization and the dominating contribution to it is embodied in $(\epsilon_{0m} - \epsilon_{\infty m})$. To calculate the Kirkwood correlation factor (g^{eff}) from eq. (3) is not fully legitimate since in the investigating binary system, the water-water, water-2-Propanol, water-G and 2-Propanol-2-propanol, G-G correlation exist.

(ii) It is impossible to determine 'g₁' and 'g₂' from a single value of the static dielectric constant without some assumption. In the second model, the Kirkwood correlation factors for individual species $i=1,2$ are modified by assumed for 2-Propanol-water, Glycerol-water mixtures that two kinds of intermolecular hydrogen bonds exist. One is the hydrogen bond between the water molecules, another is the hydrogen bond between the 2-Propanol, G and water molecules. These new correlations (g_1 and g_2) are described by the relation as follows

$$g_1 = 1 + Z_{11} \cos \varphi_{11} + Z_{12} \cos \varphi_{12} (\mu_2 / \mu_1) \quad (4)$$

$$g_2 = 1 + Z_{21} \cos \varphi_{21} (\mu_1 / \mu_2) \tag{5}$$

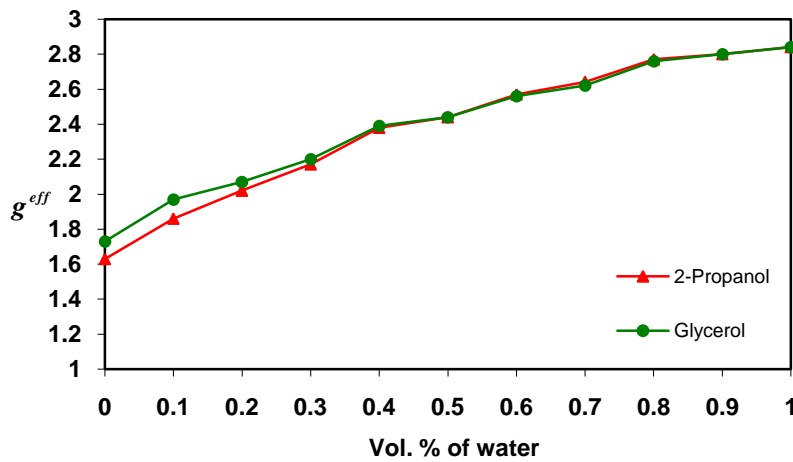


Fig.3. Variations of g^{eff} values for 2-Propanol and Glycerol with water mixtures.

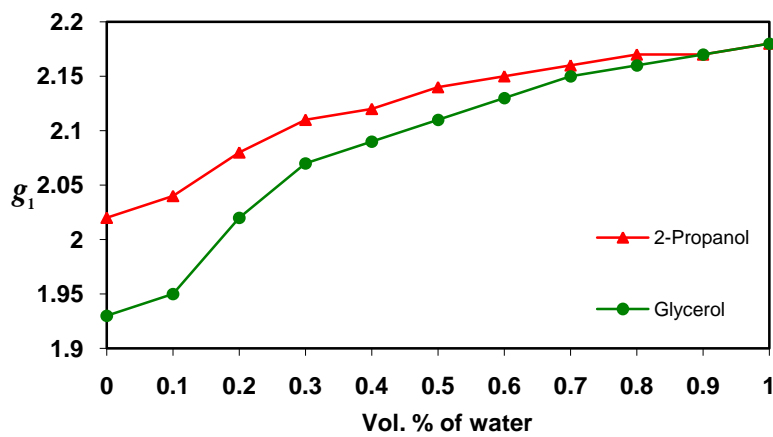


Fig.4. g_1 values for different 2-Propanol and Glycerol with water mixtures.

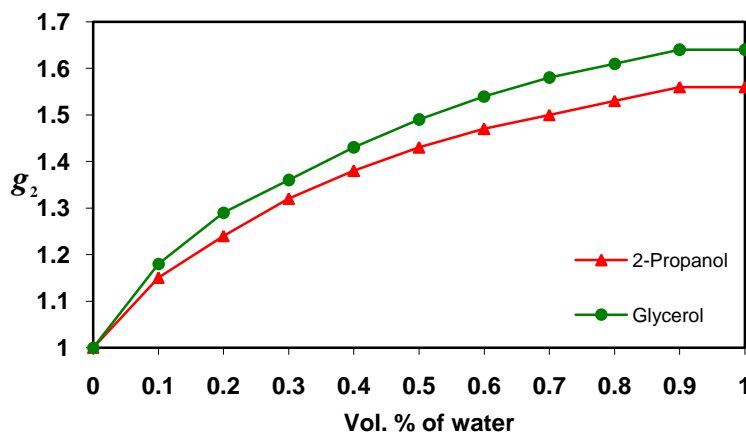


Fig.5. g_2 values for different 2-Propanol and Glycerol with water mixtures.

The excess dielectric constant parameters approach is useful which may provide some trend regarding the interactions. The contribution of hydrogen bonds to the dielectric properties of mixtures is studied in terms of the excess static dielectric constant. The excess permittivity (ϵ_0^E) may also provide structural information. This is determined for the 2-Propanol-water and G-water aqueous solutions as follows.[8]

$$\epsilon_0^E = (\epsilon_0)_M - [(\epsilon_0)_W X_1 + (\epsilon_0)_A (1 - X_1)] \quad (6)$$

where $(\epsilon_0)_M$, $(\epsilon_0)_W$ and $(\epsilon_0)_A$ represent values static dielectric constant corresponding to mixture, water and alcohol, respectively and 'X₁' is the mole fraction of water.

The excess permittivity (ϵ_0^E) may provide qualitative information in the mixture as follows:

- (i) $\epsilon_0^E = 0$ indicates that water and 2-Propanol or Glycerol do not interact at all.
- (ii) $\epsilon_0^E < 0$ indicates that water and 2-Propanol or Glycerol interaction is such that the total effective dipolar polarization get reduced.

The resulting excess dielectric constants of water-2-Propanol and water-G mixture are shown in Fig.8. The negative values of excess permittivity were observed. The negative values of excess parameter suggest that the addition of 2-Propanol and Glycerol to water may create multimeric structure leading to decrease in the total permittivity. The hydrogen bonded model gives quantitative agreement with the experimental data of excess dielectric constant of the mixture. Excess dielectric constant of 2-Propanol-water mixture have greater negative value than the G-water mixture..

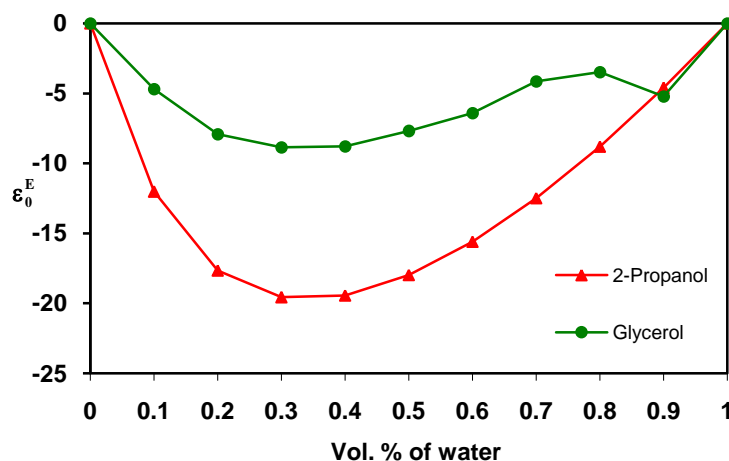


Fig.6. Excess permittivity of 2-Propanol and Glycerol Vs volume fraction of water.

IV. CONCLUSIONS

In this paper dielectric properties have been compared between 2-Propanol-water and Glycerol-water mixture. Static dielectric constant of both the mixture have same pattern and have large difference in their values. There is large difference found in relaxation time of 2-Propanol-water mixture and Glycerol-water mixture because of greater molecular weight of Glycerol. The Kirkwood correlation factor for both mixtures shows nearly similar association effect. Excess permittivity shows in 2-Propanol-water mixture interaction in

molecules is greater may be due to extra –OH group. Both aqueous solutions have similar no. of carbon atoms and H atoms but molecular weights are different which makes a difference in dielectric properties.

ACKNOWLEDGMENT

Sincere thanks to Dr.A.C.Kumbharkhane for his constant support in research activity.

REFERENCES

- [1] S M Puranik, A C Kumbharkhane and S C Mehrotra, *Proc. Natl. Acad. Sci. India*,63(A)II (1993)
- [2] W A P Luck, H Borgholte and T Hobermehl, *J. Mol. Struct.*,177 (1988)523.
- [3] S Mashimo, S Kuwabara, S Yagihara and K J Higasi, *Chem. Phys.*, 90 (1989)3292.
- [4] D Bertolini, M Cassettari, and G Salvetti, *J. Chem. Phys.*, 78 (1983)365.
- [5] B Gestblom, and S Joblom, *J. Acta. Chem. Scand.*,A38 (1984) 575.
- [6] J P Perl, D T Wasan, P Winsor and R H Cole, *J. Mol. Liq.*, 28 (1984)103.
- [7] S Havriliak and S Negami, *J. Polym. Sci.*,14 (1996) 91.
- [8] J B Hasted, "Aqueous dielectric", [Chapman and Hall London.] (1973)



**EFFECT OF Zr CONTENT ON THE STRUCTURAL CHARACTERISTICS OF
LEAD TITANATE PZT CERAMICS****Vijendra A. Chaudhari* and Govind K. Bichile**

Department of Physics, Dayanand Science College, Latur - 413 512.

Department of Physics, Dr. Babasaheb Ambedkar Marathwada University, Aurangabad - 431 004.

*Corresponding author Tel: +91 9890309211.

E_mail address: vijendra333@gmail.com (V.A. Chaudhari)

ABSTRACT :

Polycrystalline samples of $PbZr_xTi_{1-x}O_3$ [referred as PZT] where $x = 0.0, 0.2, 0.4, 0.6, 0.8$ and 1.0 have been synthesized by a high-temperatures solid-state reaction technique. One of the objectives of this work was to optimize carefully the process variables which influence the structural and microstructural properties of the samples prepared. Structural phase evolution studies of $PbZr_xTi_{1-x}O_3$ (PZT) system have been carried out as function of Zr/Ti ratio using room temperature X-ray powder diffractometric studies. The analysis of the X-ray diffraction patterns (XRD) for the sample with $0.0 \leq x \leq 0.4$ confirmed the tetragonal phase formation and no impurity peaks were observed. With increase in Zr content i.e. for $x = 0.6$ and 0.8 the observed diffraction peaks indicate the presence of rhombohedral phase in this composition range. With further increase in Zr content i.e. $x = 1.0$ the observed diffraction pattern confirmed the presence of single phase orthorhombic structure. The average linear particle sizes for all the compositions estimated using Scherrer's formula lie in the rang 400-500 nm. Microstructural studies for all the samples have been carried out using scanning electron microscopy (SEM). The SEM analysis of the samples also showed nearly uniform grain distribution i.e. uniform microstructure with no abnormal grain growth. The values of average grain size were obtained using mean intercept method and the value of grain size lie between 1-2 μm . Vibrational spectroscopy data obtained in the wavenumber region 350 to 800 cm^{-1} for the samples showed characteristic peaks corresponding to the vibrational modes of perovskite structure and a shift in the frequency of the peaks towards the lowered side with the increase of Zr content have been observed.

KEYWORDS : A. Powders: solid state reaction; sintering; B. Electron microscopy; Grain size; Porosity; X-ray methods; D. PZT; Perovskites; E. Capacitors .

1. INTRODUCTION

A solid solution of perovskite ferroelectric $PbTiO_3$ and antiferroelectric $PbZrO_3$ in different Zr/Ti ratio has been considered as an important material for a wide range of piezoelectric, pyroelectric and ferroelectric device applications such as transducers, computer memory and display and pyroelectric sensors [1,2]. The physical properties or device parameters of lead zirconate titanate (PZT) can be tailored by synthesizing the material with improved processing techniques and making suitable substitutions at A and/ or B- sites. The properties of these substituted ferroelectric are greatly influenced by the manner in which B-site cations are distributed and ordered on the B-site of lattice. It is important to understand the influence of the Zr/Ti ratio on the properties, such as structural phase evolution, electric and dielectric properties, the piezoelectric constant, the coupling factor etc.

Although PZT ceramics have been established in technological applications for years [3], the microstructure of this class of materials is still under investigation and the atomistic phenomena that cause the strong extrinsic piezoelectric and ferroelectric effect have not yet been completely understood, neither the mechanisms of its degradation. So far, the microstructure of PZT's close to the morphotropic phase boundary (MPB) of the quasibinary phase diagram of lead titanate has not been completely elucidated. The structural phase evaluation in the $\text{PbZr}_x\text{Ti}_{1-x}\text{O}_3$ is strongly composition dependent.

Lead titanate zirconate $\text{PbZr}_x\text{Ti}_{1-x}\text{O}_3$ solid solutions noted PZT, which crystallize in various distorted perovskite-type structures, are well-known for their dielectric and ferroelectric properties. The PZT binary phase diagram can be roughly described in three areas at room temperature [3]: the rhombohedral Zr-rich region is separated from the tetragonal Ti-rich one by a morphotropic phase boundary (MPB) in which the two phases coexist. Above the Curie temperature, which increases with Ti content, all the compounds crystallize in a paraelectric cubic phase (space group $\text{Pm}\bar{3}\text{m}$). The compositions near the morphotropic phase boundary are interesting due to their important piezoelectric response [4-6]. Moreover, the substitution of modifier ions in PZT produces ceramics with highly improved piezoelectric properties as compared with the parent composition [7-9]

The morphotropic phase boundary (MPB) has been believed to be a sharp transition, but in practice the MPB has a finite range of compositions over which the tetragonal and rhombohedral phases coexist in the materials. The width of the MPB has been investigated by several workers in different Pb based perovskite ferroelectric systems and the width has been found to be related to the distribution of cations on the B-site of the perovskite lattice [10-12].

Many factors have been found to influence the non-uniformity of composition of PZT near the MPB, such as particle size of starting powders, surface area and purity. More important however, are process variables such as calcination temperature, sintering time and temperature and the method employed to minimize PbO loss. The volatility of the PbO component of PZT at high temperatures makes the stoichiometry difficult to control. Either an excess or a deficiency of PbO can degrade the properties of the material. Excess PbO is usually added to compensate for loss of PbO during the synthesis by solid-state reaction. In the present work the loss of PbO is compensated by adding excess PbO (5%).

Polycrystalline samples of $\text{PbZr}_x\text{Ti}_{1-x}\text{O}_3$ [referred as PZT] where $x = 0.0, 0.2, 0.4, 0.6, 0.8$ and 1.0 have been synthesized by a high-temperatures solid-state reaction technique. The objective of this work was to optimize carefully the process variables which influence the structural and microstructural properties of the samples prepared. Structural phase evolution studies of $\text{PbZr}_x\text{Ti}_{1-x}\text{O}_3$ (PZT) system have been carried out as function of Zr/Ti ratio using room temperature X-ray powder diffractometric studies. Microstructural studies for all the samples have been carried out using SEM. IR studies have been performed to understand the effect of the substitution of Ti/Zr on the vibrational modes. The IR measurements were performed on powder samples at room temperature in KBr matrix.

2. EXPERIMENTAL

Polycrystalline samples of $\text{PbZr}_x\text{Ti}_{1-x}\text{O}_3$ [for $x = 0.0, 0.2, 0.4, 0.6, 0.8$ and 1.0] were synthesized from high purity ingredients via PbCO_3 (99.9% purity; Aldrich chemicals), ZrO_2 (99.9% purity; Aldrich chemicals) and TiO_2 (99.9% purity; Loba chemie.) using a high-temperature solid-state reaction technique in an air atmosphere. To prevent PbO loss or vaporization during the high-temperature sintering, 5% by weight excess of PbO was added. The excess PbO helps to compensate for the lead evaporation during sintering process. The constituent compounds in a suitable stoichiometry were thoroughly mixed and wet ground using an agate mortar and pestle for 2 hr. The sieved fine powders were then calcined in an alumina crucible at temperature ranging from $450\text{--}550^\circ\text{C}$ for 8 hr. in air atmosphere and brought to room temperature under slow cooling. The process of grinding was repeated and the ground material was sieved through $75\mu\text{m}$ (200 mesh). The sieved fine powder was cold pressed into cylindrical pellets of size 10mm and 1-2 mm of thickness using hydraulic press at a pressure of 50 MPa. The pellets were sintered in an air atmosphere at 900°C for 12 hr. The formation and purity of the compounds were checked by an X-ray diffraction (XRD)

technique. Densities of the sintered pellets were measured by Archimedes principle. Porosity was evaluated from the observed and theoretical densities (X-ray). The grain morphology and average grain size were determined using SEM. The average grain size was determined by using a linear intercept method. The average particle size was also determined from the full width at half maximum using Scherrer's equation [13]

The X-ray diffraction pattern of the compounds were recorded at room temperature using X-ray powder diffractometer (Xpert Pro-PAN Philips) with $\text{CuK}\alpha$ radiation ($\lambda = 1.5418 \text{ \AA}$) in a wide range of Bragg angles 2θ ($10^\circ \leq 2\theta \leq 80^\circ$) with a scanning rate of 0.02° . The surface morphology of the pellets was studied by scanning electron microscopy (SEM) (JEOL JSM- 6360 A). The FTIR data of $\text{PbZr}_x\text{Ti}_{1-x}\text{O}_3$ was recorded using computer controlled FTIR-8400 Shimadzu spectrophotometer in the wave number range 4000 to 400 cm^{-1} in KBr medium at room temperature (25°C). The experiment was carried out in an inert atmosphere. The optical resolution for data collection was 4 cm^{-1} .

3. RESULTS AND DISCUSSION

Fig.1 shows the room temperature x-ray diffraction patterns of $\text{PbZr}_x\text{Ti}_{1-x}\text{O}_3$ for different x values. The XRD pattern show sharp diffraction peaks, which indicate a better homogeneity and crystallization of the samples.

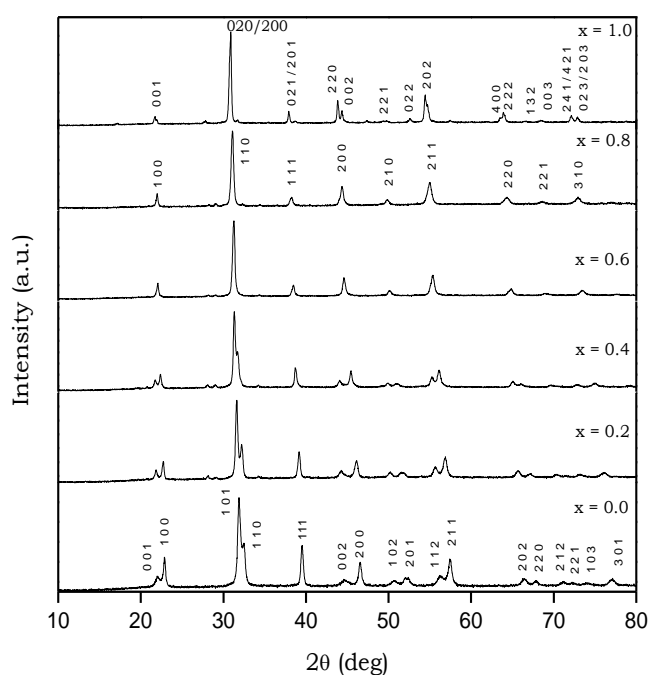


Fig. 1 Room temperature X-ray diffraction patterns of $\text{PbZr}_x\text{Ti}_{1-x}\text{O}_3$ ($0.0 \leq x \leq 1.0$).

The X-ray diffraction patterns for the samples with $x = 0.0, 0.2$ and 0.4 were indexed in the tetragonal system and a good agreement between calculated and observed (d) values for all observed diffraction peaks of PZT with $x = 0.2$ and 0.4 confirm the tetragonal phase formation. No impurity peaks were observed. With increase in Zr content i.e. for $x = 0.6$ and 0.8 , the position of observed diffraction peaks indicate the presence of rhombohedral phase in this composition range. With further increase in Zr content, i.e. $x = 1.0$ the observed peaks confirm the presence of single phase orthorhombic structure. All the reflection peaks were indexed using observed interplanar spacing (d) and lattice parameters of PZT were determined using a least squares refinement method. All the calculations were done using a computer program package "Powder X". The observed peaks positions were compared with the information from the "JCPDS" data base to identify the phases present and to index the peaks. Table 1 lists the value of unit cell

parameters (a, b, c), unit cell volume, density and porosity of $\text{PbZr}_x\text{Ti}_{1-x}\text{O}_3$ for different x values. The average linear particle sizes for all the composition estimated by using Scherrer's formula are presented in Table 1.

Table 1 Value of unit cell parameters (a, c), Unit cell volume, density and porosity of $\text{PbZr}_x\text{Ti}_{1-x}\text{O}_3$, ($0.2 \leq x \leq 1.0$).

Composition (x) Zr / Ti	Lattice Parameter			α (deg.)	Unit Cell Vol. $V (\text{\AA})^3$	Fraction of theoretical Density (%)	Porosity (%)
	a (\AA)	b (\AA)	c (\AA)				
0.2 / 0.8	3.9476	3.9476	4.1185	90	64.18	91.6	8.3
0.4 / 0.6	3.9985	3.9985	4.1237	90	65.93	91.9	8.0
0.6 / 0.4	4.0896	4.0896	4.0896	89.91	68.39	89.9	10.0
0.8 / 0.2	4.0976	4.0976	4.0976	89.95	68.80	91.6	8.3
1.0	5.8893	5.8840	4.0995	90	142.06	94.3	5.7

Figs.2 (a)-(e) show SEM images of the surfaces of PZT ceramics. It is clear from the nature of micrographs that the grains are nearly spherical in shape and do not show the presence of any microcracks. The image analysis also showed nearly uniform grain distribution i.e. uniform microstructure with no abnormal grain growth. The average grain size was determined by using mean linear intercept method [14]. The values of average grain size obtain from SEM micrograph are also listed in Table 2.

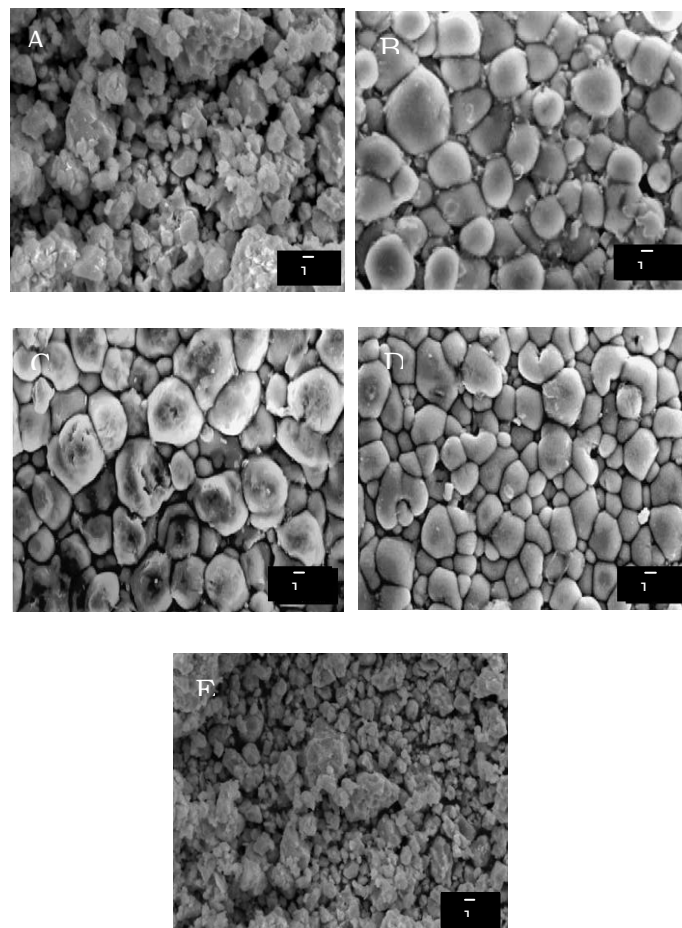


Fig. 2 SEM micrographs of $\text{PbZr}_x\text{Ti}_{1-x}\text{O}_3$ at (A) $x = 0.2$, (B) $x = 0.4$, (C) $x = 0.6$, (D) 0.8 , (E) $x = 1.0$.

Fig. 3 shows the IR spectra from 350-800 cm^{-1} of $\text{PbZr}_x\text{Ti}_{1-x}\text{O}_3$ (PZT) for $x = 0.2, 0.6$ and 1.0 composition. The characteristic bands of Pb-O and Ti-O at 500-700 cm^{-1} are observed. The spectra show a characteristic peak appearing at a wave number $\sim 575 \text{ cm}^{-1}$ in case of all the samples. It is found that a shift in the frequency in the lower side of the spectrum in accordance with the relation:

$$\nu = \frac{1}{2} \pi \sqrt{\frac{k}{\mu}}$$

Higher the mass of substituents the shift in frequency as a result would be towards the lower side of the spectrum. Zirconium is heavier than titanium, results in shift of peak towards lower side on being substituted at the site of Ti. This result also supports that the substitution of Zr take place in Ti site and not in oxygen octahedral site.

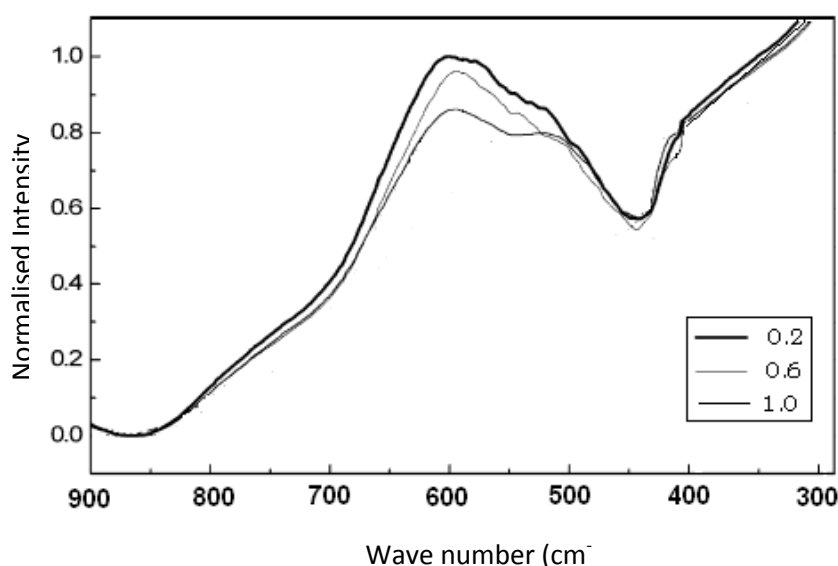


Fig. 3 FT-IR spectra of $\text{PbZr}_x\text{Ti}_{1-x}\text{O}_3$ ceramics for $x = 0.2, 0.6$ and 1.0 .

Table 2 Particle size (XRD), Grain size (SEM) and phase and space group of PZT.

Composition (x)	Particle Size (nm)	Average grain size (μm)	Phase & Space Group
Zr / Ti			
0.2 / 0.8	515	1.38	T (P4mm)
0.4 / 0.6	498	2.28	T (P4mm)
0.6 / 0.4	476	2.35	R (R3m)
0.8 / 0.2	454	1.67	R (R3m)
1.0	491	1.35	O (Pbma)

4. CONCLUSIONS

Lead Zirconate Titanate [referred as PZT] powder samples have been synthesized by solid-state reaction in accordance with the formula $\text{PbZr}_x\text{Ti}_{1-x}\text{O}_3$ with compositions $0.0 \leq x \leq 1.0$. The structural analysis performed from X-ray powder diffraction data (XRD) reveals that the tetragonal phase exists in the composition range $0.2 \leq x \leq 0.4$ and rhombohedral phase exist in the composition range $0.6 \leq x \leq 0.8$. For $x = 1.0$ the sample exhibited orthorhombic phase. The morphological studies using SEM showed nearly uniform

grain distribution i.e. uniform microstructure with no abnormal grain growth. Analysis of IR data showed the characteristic peaks corresponding to the vibrational modes of perovskite structure and a shift in the frequency of the peaks towards the lowered side with the increase of Zr content has been observed.

REFERENCES

- [1] B. Jaffe, R. Cook, H. Jaffe, Piezoelectric Ceramic. Academic Press, London/New York, 1971.
- [2] S.L. Fu, S.Y. Cheng, C.C. Wei, Ferroelectrics 67 (1986) 93-96.
- [3] L. Li, X.M. Chen, Mater Sci Eng B 108 (2004) 200-205.
- [4] C. Bedoya, C.h. Muller, J-L. Baudour, V. Madigou, M. Anne, M. Roubin, Material Science and Engineering B 75 (2000) 43-52.
- [5] B. Jaffe, W. Cook, H. Jaffe, Piezoelectric Ceramic. New York: Academic Press Inc; 1971.
- [6] W. Eremkin, W.G. Smotrakow, E.G. Fesenko Sov, Solid State Phys 31 (1989)156-160.
- [7] D. Viehland, Phys Rev B 52 (1995) 778-791.
- [8] V. Koval, J. Briancin, Ferroelectrics 193 (1997) 41-49.
- [9] F. Kulcsar, J Amer Ceram Soc 42 (1959) 343-349.
- [10] A.E. Crawford, Br Comm Elec 6 (1959) 516-521.
- [11] G.H.L. Wong, B.W. Chua, Lu. Li, M.O. Lai, J Mater Process Tech 113 (1974) 450-455.
- [12] S.A. Mabud, J Appl Cryst 13 (1980) 211-216.
- [13] B.D. Cullity, Elements of X-ray Diffraction. 2nd ed. Addison –Wesley:Massachusetts;1978.
- [14] D.G. Brandon, W.D. Kaplan. Microstructural Characterization of Materials. John Wiley & sons Ltd; 1999.



CdS AND CdZnS QUANTUM DOTS THIN FILMS PREPARED BY LOW COST CHEMICAL ROUTE METHOD FOR SOLAR CELL APPLICATIONS

Mr. Akash Raut ^a, Mr. Akash Sawate, ^a Mr. Dipak Tonpe ^a, Mr. Pawan More ^a, Mr. Makarand Sonawne ^a, Dr. Avinash Dive ^a, Dr. Ketan Gattu ^a, Dr. Sandip Mahajan ^a, Dr. Vinod Mokale ^a, Dr. Rajesh A. Joshi ^b, Ramphal Sharma ^{a*}

^aThin Film and Nanotechnology Laboratory, Department of Physics and Nanotechnology, Dr. Babasaheb Ambedkar Marathwada University, Aurangabad-431004, (M.S.), India.

^bDepartment of Physics, Toshniwal Arts, Commerce & Science College, Sengaoan, Dist. Hingoli -431542 (MS)

ABSTRACT :

Chemical bath deposition of CdZnS is achieved by the slow release of sulphide ions and the controlled release of cadmium and zinc ions in solution. However the difference in the solubility products of CdS and ZnS by several orders usually narrows the chalcogenide operating window, this coupled with the difference in their stability constant makes CdZnS CBD process very difficult. We report the deposition and optimization of the growth parameters that maximizes the thickness of the deposited film in alkaline solution. The Optical and electrical properties characterized by UV-Vis spectroscopy and I-V characteristics method. The absorption of CdS is shifted higher wavelength and band gap was decreased. The composited CdZnS band gap increases with decreases in absorption. The band gap of CdS and CdZnS thin film are 2.02eV and 2.20eV respectively. The electrical properties shows the current increases of CdZnS thin film. The optoelectrical properties of CdZnS thin film has superior compared CdS thin film confirmed by studies.

KEYWORDS : CdZnS, thin film, Optical absorption, Band Gap etc.

INTRODUCTION

Ternary derivatives of CdS have generated a lot of research interest for applications in the field of optoelectronic devices. One such ternary compound is Cadmium Zinc Sulphide have generated a lot of research interest for applications in the field of optoelectronic devices [1-5]. One such ternary compound is Cadmium Zinc Sulphide. (CdZnS) which is gaining prominence as good candidate for wide band gap material for photovoltaic and photo-conducting devices [4-9]. Its band gap can be tailored from 2.42eV (CdS) to 3.7eV (ZnS). The addition of Zn to CdS enhances the open-circuit voltage and shortcircuits current in hetero-junction devices as a result of the decrease in the window absorption losses [4-12]. CdZnS films have been deposited in various ways: Sol Gel, Physical Vacuum evaporation (PVD), Spin coating, Successive Ionic Layer Adsorption and Reaction method (SILAR) and chemical bath deposition (CBD) [2-5]. Among these techniques CBD is favoured because it is relatively simple, inexpensive and scalable technique for the deposition of high quality and large area films. The CBD process is performed by slow release of S²⁻ and controlled free Zn²⁺ and Cd²⁺ ions in an alkaline solution Thiourea (CS(NH₂)₂) and thioacetamide (CH₃CSNH₂) are two sulphiding agents commonly used [6-10]. A chelating agent is used to limit the hydrolysis of the metal ion and impart some stability to the bath, which would otherwise undergo rapid hydrolysis and precipitation. The proper chalcogenide operating window is further narrowed and the process made more difficult due to the different stability constants of the Cd and Zn precursors. As a result of these difficulties, some researchers have resorted to the use of multilayer processing. Acidic bath deposition has also been investigated. This has been based on the successive acidic bath deposition of ZnS, with the use of

urea hydrolysis in the control of the pH. It is thus argued that if CdS could be successfully deposited from similar bath, the possibility of depositing the true ternary compound could be improved as the problem of the gross insolubility of Zinc hydroxyl specie would be reduced at low pH [10-12]. Adherent orangeyellow films were obtained at a ph of 9.2. We report the alkaline deposition of CdZnS and the investigation of the various deposition parameters to obtain optimum film thickness.

EXPERIMENTAL WORK

CdZnS thin films were deposited on Menzel-glazer glass slides. The chemicals used were 0.015M cadmium acetate ($\text{Cd}(\text{CH}_3\text{COO})_2$), 0.015M zinc acetate ($\text{Zn}(\text{CH}_3\text{COO})_2$) and 0.05M thiourea ($\text{SC}(\text{NH}_2)_2$). The concentration of ammonium acetate ($\text{NH}_4\text{CH}_3\text{COO}$) used as buffer was varied from 0.1-0.6M in steps of 0.1, while ammonia solution (NH_3OH) concentration was varied from 0.4-1.2M in steps of 0.2. The temperature was also varied from 55- 85°C while keeping the ammonium acetate and ammonium hydroxide constant. A 25ml beaker was used as container for the reacting chemicals; this was immersed in a water bath and heated to desired temperature with a hot plate. Cadmium acetate, Zinc acetate, ammonium acetate and thiourea were first mixed in the 25ml beaker and heated to desired temperature, ammonia solution was then added and substrates immersed vertically. The substrate had earlier been washed with detergent, rinsed in deionised water, soaked in nitric acid, degreased in ethyl alcohol and then rinsed in deionised water [1-6]. The reacting bath was agitated throughout the period of deposition. The film thickness was measured using weight-difference-density consideration. The normal incidence absorbance spectrum of the film obtained at optimum deposition parameter was measured UV- Vis spectrophotometer (perkin Lamda 25). The measurements were taken from the near ultraviolet (300nm) to the near infrared (900nm) regions. The I-V Characteristics measurements were taken under the light condition by using Keithely 2601 Instrument.

RESULT AND DISCUSSION

Figure 1 shows the basic mechanism of Chemical bath deposition (CBD) method. The chemical bath deposition method has advantages such as low cost techniques, less instruments, easily producible as compared physical techniques. Figure 2 shows the absorption spectra of CdS and CdZnS thin film in visible range. Figure 2 shows the absorption spectra of CdZnS thin films as a function of wavelength. The absorption decreases with increasing wavelength. A sudden decrement at absorption edge is observed in the absorption spectra for each CdZnS composite [2-12].

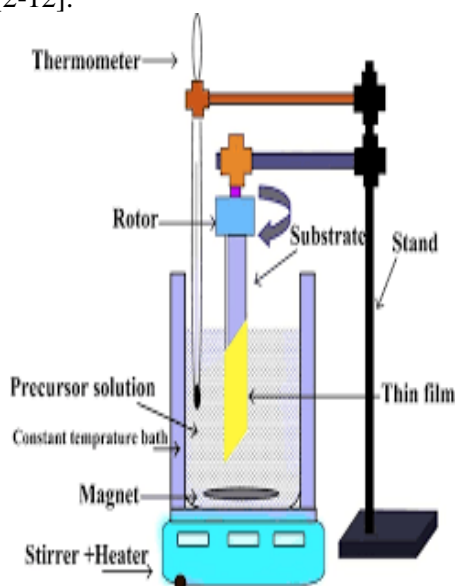


Figure : 1 Chemical Bath Deposition [CBD]

The band gap of CdS and CdZnS thin film were calculated by Tauc's equation. In absorption spectra, the absorption edge shifts towards the lower wavelength side with increasing Zn content in CdS. Figure 3

shows band gap CdS and CdZnS thin films. The energy band gap of these CdZnS is 2.2eV. The CdS thin film band gap 2.02eV. The film had a high enough long wavelength optical absorption for solar cell application [6-11].

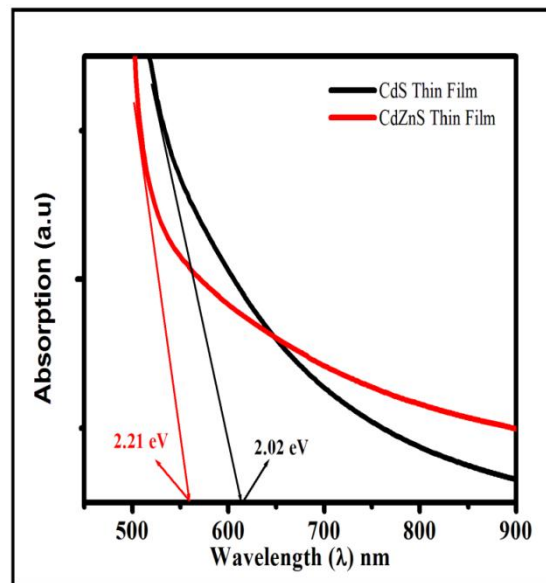


Figure : 2 spectra of CdS Absorption and CDZnS thin films

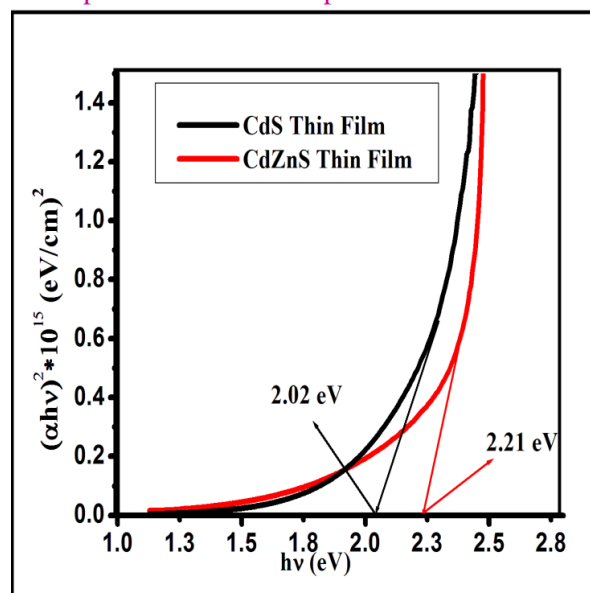


Figure: 3 Energy band gap of CdS and CdZnS thin films

Figure 4 shows the electrical properties of CdS and CdZnS thin films studied by I-V characteristics measurement at room temperature under 300 W/cm² illuminations light. The CdZnS thin film shows enhancement current as compared CdS thin film. Zn inserted in CdS nanocrystals due to current shifted in higher range [1-9].

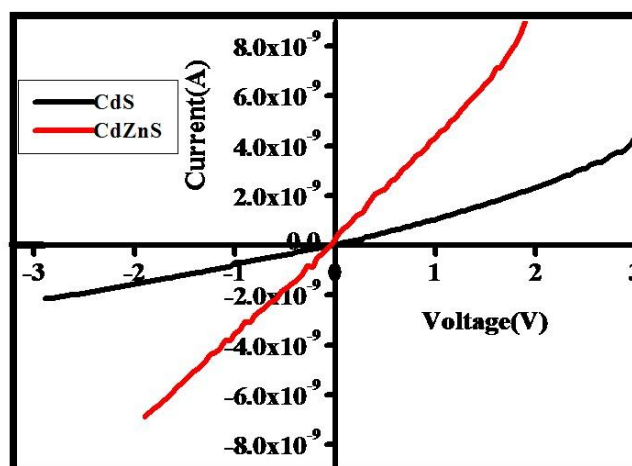


Figure: 4 I-V Characteristics of CdS and CdZnS thin films

CONCLUSION

CdZnS films were deposited at a temperature of 75°C and a pH of between 9.2 and 9.7. Optimum film thickness was obtained for ammonium acetate concentration of 0.3M and 0.8M ammonium hydroxide. These concentrations tend to minimize homogeneous reaction leading to improved film quality and thickness maximization. The film had a high enough long wavelength optical absorption for solar cell application. The CdZnS thin film was wavelength beyond the absorption edge for the optimum film thickness obtained. The film had a band gap of 2.20eV of the CdZnS was determined. The enhancement of current of CdZnS thin film as compared CdS thin film.

ACKNOWLEDGEMENT

One of the authors Mr. Akash Raut is thankful to department of Nanotechnology, Dr. Babasaheb Ambedkar Marathwada University, Aurangabad, Maharashtra for financial support and facilities

REFERENCES:-

- [1] Gruzsecki T and Halmstrom B 1993 *Solar Energy Mater. Solar Cells* **31** 227
- [2] X.-D. Xiang, X. Sun, G. Briceno, Y. Lou, K.-A. Wang, H. Chang, W.G. Wallace, S.W. Freedman, P.G. Schultz, *Science* **268**, 1738(1995)
- [3] B. D. Wllihy, *Elements of X-ray diffraction*, Addison-wesley MA, (1978) pp. 102.
- [4] S. Thanikaikarasan, T. Mahalingam, K. Sundaram, A. Kathalingam, Y. D. Kim and T. Kim, *Vacuum*, (2009) **83**, 1066–1072.
- [5] Yamaguchi T., Yamamoto Y., Tanaka T., Demizu Y., Yoshida A., Title of the article, *Thin solid films*, 1996, **375**, p. 281-282.
- [6] Valkonen M.P., Kannianien T., Lindroos S., Leskela M. and Rauhala E., Growth of ZnS, CdS and multilayer ZnS/CdS thin film by SILAR technique, *Appl. Surf. Sci.*, 1997, **115**, p. 386-392.
- [7] Zhou J., Wu X., Teeter G., To B., Yan Y., Dhare R. G. and Gessert T.A., CBD Cd_{1-x}Zn_xS thin films and their application in CdTe solar cell, *Phys. Stat. Sol.*, 2004, **241**(3), p. 775- 778.
- [8] Oladeji I. O and Chow L., Optimization of chemical bath deposited cadmium sulfide thin films, *J. Electrochem. Soc.*, 1997, **144**, p. 2342-2346.
- [9] A. Owens, A. Peacock, *Nucl. Instrum. Methods Phys. Res. A* **531**, 18 (2004)
- [10] Dzhanfarov T D and Ongul F 2005 *J. Phys. D: Appl. Phys.* **38** 3764 IOPscience
- [11] S P 1995 *J. Electron. Mater.* **24** 697
- [12] Bacaksiz E, Dzhanfarov T D and Novruzov V D et al 2004 *Phys. Status. Solids. (a)* **201** 2948



STRUCTURAL AND SURFACE PROPERTIES OF PURE AND Fe DOPED TiO₂ NANOPARTICLES PREPARED BY CHEMICAL ROUTE METHOD

Mr. Akash Sawate^a, Mr. Akash Raut^a, Mr. Dipak Tonpe^a, Mr. Pawan More^a, Mr. Makarand Sonawne^a, Dr. Avinash Dive^a, Dr. Ketan Gattu^a, Dr. Sandip Mahajan^a, Dr. Vinod Mokale^a, Dr. Rajesh A. Joshi^b, Prof. Ramphal Sharma^{a*}

^aThin Film and Nanotechnology Laboratory, Department of Physics and Nanotechnology, Dr. Babasaheb Ambedkar Marathwada University, Aurangabad-431004, (M.S.), India.

^bDepartment of Physics, Toshiwal Arts, Commerce & Science College, Sengaoan, Dist. Hingoli -431542 (MS)

ABSTRACT :

The Pure and Fe-doped TiO₂ nanoparticles were synthesized by the sol-gel method and it annealed at 400°C for 2 hour. The Structural and Surface properties have characterized by using various techniques such as X-ray diffraction (XRD), and Brunner Emmet teller (BET) technique. The pure TiO₂ XRD spectra revealed that the synthesized sample is a Poly-crystalline nature with high intensity of peaks compared Fe doped TiO₂. Both XRD spectrum shows anatase phase. The BET surface analyzer shows pore size and pore volume of pure and Fe doped TiO₂ nanoparticles. The absorption spectra shifted to higher wavelength in visible ranger after doping and band gap was decreases.

KEYWORDS : TiO₂ Nanoparticles, Sol Gel method, Surface properties, and pore size etc.

INTRODUCTION

Titanium dioxide (TiO₂) is a well-known non-toxic, bio-compatible and corrosion-resistant material. It is a significant material that has been widely used for a large number of applications in photovoltaic cells batteries chemical sensing, optical emissions, photonic crystals, catalysis, photocatalysis, environmental purification and biological templates due to its optical, chemical and mechanical properties[1-5]. It is important to increase the specific surface area to obtain a high efficiency for these applications that are commonly used with nanoscale TiO₂ materials. The use of TiO₂ nanoparticles is expanding day by day with healthcare and various energy application. TiO₂ mainly exist in three crystalline nature polymorphs namely anatase, rutile and brookite. Anatase is the most highly than the rutile and brookite [4-10]. TiO₂ is odourless and insoluble in water. TiO₂ has the many application mainly as photocatalyst and healthcare, self cleaning, sunscreen, cosmetics. Air pollution and waste water treatment and drug deliver[10-14]. the doping of a Fe³⁺ ion reduces the recombination of the photogenerated electron and hole which leads to the enhancement of photocatalytic activity of TiO₂. In these present work I m synthesized the pure and Fe doped TiO₂ nanoparticle photocatalyst by sol-gel method at the temperature 400 °c the objective of these work is to examine the role of fe doping on the phase transition, average crystalline size and surface properties.

EXPERIMENTAL WORK

Take a stoichiometric quantity of ferric nitrate is dissolved in 80 ml of distilled water with add 5 ml of Glacial Acetic acid stirring these solution mixture few minutes. Same as stoichiometric quantity of titanium Isopropoxide is mixed with 70 ml ethanol and placed in stirring machine and constant stirring. After that two solution were added dropwise together for 60 min under constant stirring. After that the obtained the sol-gel were stirred constantly for 2 hours stirred and aged for the 2 days in room temperature. After these two days

bottom of conical flask gel was formed and obtained precipitate were filtered and wash several [5-6] times with ethanol and distilled water and dried for 12 hours at 100°C . The obtained material were ground and annealed at 400°C for 4 hours. After the annealed material was ground again and used further for characterization. The samples were characterized by X-ray diffraction (XRD), and BET surface area analyzer Bruker and Quantachrome ASiQwin system. X-ray diffraction measurements were carried out in the reflection mode on a Rigaku model diffractometer with $\text{Cu K}\alpha$ radiation ($\lambda = 0.154 \text{ nm}$). The nitrogen adsorption-desorption isotherms were obtained at 77 K using Brunauer-Emmett-Teller (BET) technique using a Quantachrome ASiQwin system.

RESULT & DISCUSSION

I have successfully synthesized a pure and Fe-doped TiO_2 photocatalyst by the Sol-Gel Method. XRD is a very important experimental technique that has long been used to address all issues related to the crystal structure of solids, including lattice constants and geometry, identification of unknown materials, orientation of single crystals, preferred orientation of polycrystals, defects, stresses, etc [5-10]. Fig (1) shows the XRD patterns of undoped and Figure (2) Fe doped nanoparticles. The observed peaks could be indexed according to the anatase phase tetragonal structure of TiO_2 (JCPDS, No. 861157). All the samples had a high degree of crystallinity and there was a slight increase in crystallinity on TiO_2 doping without any phase change [10-12]. Also, there were no obvious peaks showing the presence of TiO_2 in the samples which indicated that TiO_2 did not form the crystal but homogeneously distributed on the surface of TiO_2 [12-14].

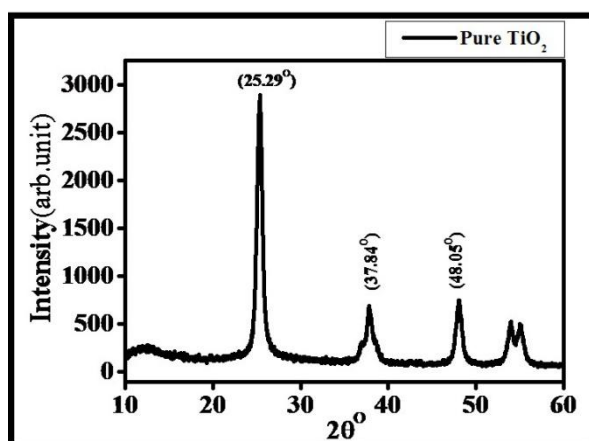


Fig 1:- X-ray diffraction spectra of Pure TiO_2 nanoparticles

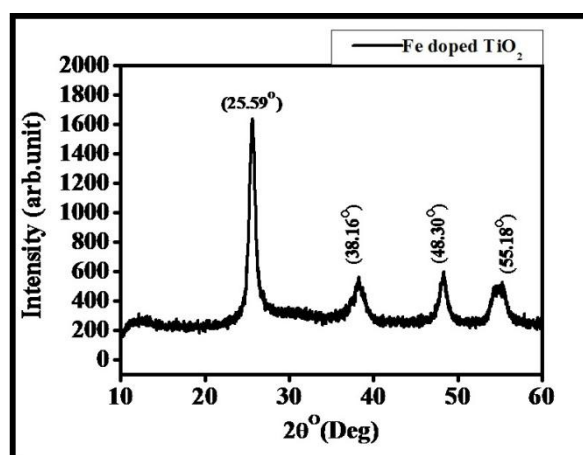


Fig 2: X-ray diffraction spectrum of Fe-doped TiO_2 nanoparticles

Figure (3) shows the undoped TiO_2 nanoparticles of BET graph and Figure (4) Fe doped TiO_2 nanoparticles. The specific surface area of the powders was measured by the dynamic BET method, in which N_2 gas was adsorbed at 77 K using a Micromeritics system. The surface areas measured for the Fe-doped samples were higher than that for the undoped sample $373.958\text{m}^2/\text{g}$. The high surface area was due to the reduction of the TiO_2 crystallite size brought about by the Fe ions. However, there was only a slightly higher surface area when the Fe content was than 0.5 wt% [5-12].

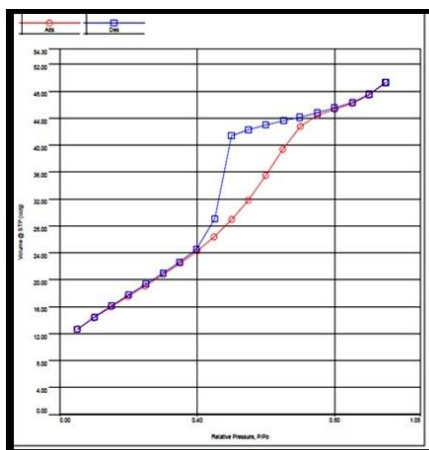


Fig 3: BET graph of TiO_2 nanoparticles shows surface area

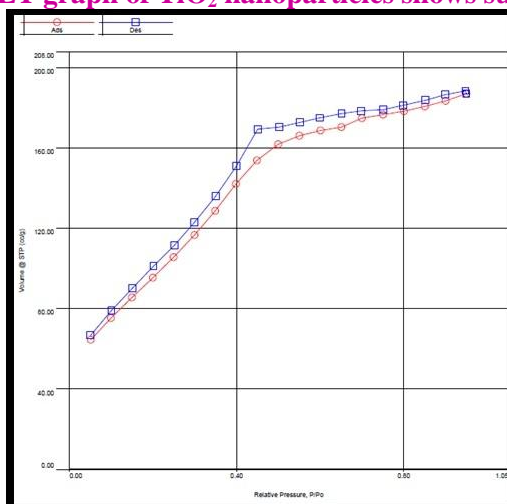


Fig 4: BET graph of Fe doped TiO_2 nanoparticles shows surface area

CONCLUSION

TiO_2 and Fe doped TiO_2 nanoparticles phase were synthesized by sol-gel method. XRD study confirmed that the Fe doping resulted in the reduction of the crystallite size of TiO_2 from 16 to 18 nm due to increase in surface area without any phase change. Both pure and doped nanoparticles shows anatase phase confirmed by XRD techniques. Fe doped TiO_2 nanoparticles surface area increases and it shows enhancement particles size.

ACKNOWLEDGEMENT

One of the authors Mr.Akash sawate is thankful to department of Nanotechnology ,Dr.Babasaheb Ambedkar Marathwada University, Aurangabad, Maharashtra for financial support and facilities

REFERENCES

- [1] S. Valencia, J.M. Marin, G. Restrepo, Study of the Bandgap of Synthesized Titanium Dioxide Nanoparticules Using the Sol-Gel Method and a Hydrothermal Treatment~!2009-10-14~!2009-10-30~!2010-01-27~!, *Open Mater. Sci. J.* 4 (2010) 9–14. doi:10.2174/1874088X01004020009.
- [2] K. Madhusudan Reddy, C.V. Gopal Reddy, S.V. Manorama, Preparation, Characterization, and Spectral Studies on Nanocrystalline Anatase TiO₂, *J. Solid State Chem.* 158 (2001) 180–186. doi:10.1006/jssc.2001.9090.
- [3] F. Cheng, S.M. Sajedin, S.M. Kelly, A.F. Lee, A. Kornherr, UV-stable paper coated with APTES-modified P25 TiO₂ nanoparticles, *Carbohydr. Polym.* 114 (2014) 246–252. doi:10.1016/j.carbpol.2014.07.076.
- [4] J. Virkutyte, S.R. Al-Abed, D.D. Dionysiou, Depletion of the protective aluminum hydroxide coating in TiO₂-based sunscreens by swimming pool water ingredients, *Chem. Eng. J.* 191 (2012) 95–103. doi:10.1016/j.cej.2012.02.074.
- [5] Q. Zhao, C. Liu, X. Su, S. Zhang, W. Song, S. Wang, et al., Antibacterial characteristics of electroless plating Ni-P-TiO₂ coatings, *Appl. Surf. Sci.* 274 (2013) 101–104. doi:10.1016/j.apsusc.2013.02.112.
- [6] S. Banerjee, J. Gopal, P. Muraleedharam, A.K. Tyagi, B. Raj, Physics and Chemistry of photocatalysis of TiO₂.pdf, *Curr. Sci.* 90 (2006) 1378–1383.
- [7] T. Ochiai, A. Fujishima, Photoelectrochemical properties of TiO₂ photocatalyst and its applications for environmental purification, *J. Photochem. Photobiol. C Photochem. Rev.* 13 (2012) 247–262. doi:10.1016/j.jphotochemrev.2012.07.001.
- [8] A. Fujishima, T.N. Rao, D. a. Tryk, Titanium dioxide photocatalysis, *J. Photochem. Photobiol. C Photochem. Rev.* 1 (2000) 1–21. doi:10.1016/S1389-5567(00)00002-2.
- [9] A. Fujishima, TiO₂ photoelectrochemistry and photocatalysis, 213 (2001) 8656.
- [10] K. Nakata, T. Ochiai, T. Murakami, A. Fujishima, Photoenergy conversion with TiO₂ photocatalysis: New materials and recent applications, *Electrochim. Acta.* 84 (2012) 103–111. doi:10.1016/j.electacta.2012.03.035.
- [11] C. Zheng, Z. Qi, W. Shen, G. Chen, Self-cleaning Bombyx mori silk: room-temperature preparation of anatase nano-TiO₂ by the sol-gel method and its application, *Color. Technol.* 130 (2014) 280–287. doi:10.1111/cote.12092.
- [12] A. Sakae, Titanium-Oxide Photocatalyst, *Three Bond Tech. News.* (2004) 1–8. doi:10.1016/0009-2614(95)00740-U.
- [13] C. Raillard, V. Héquet, P. Le Cloirec, J. Legrand, Kinetic study of ketones photocatalytic oxidation in gas phase using TiO₂-containing paper: Effect of water vapor, *J. Photochem. Photobiol. A Chem.* 163 (2004) 425–431. doi:10.1016/j.jphotochem.2004.01.014.
- [14] A. Fujishima, X. Zhang, D. a. Tryk, TiO₂ photocatalysis and related surface phenomena, *Surf. Sci. Rep.* 63 (2008) 515–582. doi:10.1016/j.surfrep.2008.10.001.



OPTICAL PROPERTIES OF COPPER OXIDE AND BISMUTH OXIDE NANOPARTICLES

K. G. Kalmegh^a and S. A. Waghuley^{*b}

^aDepartment of Physics, Govt. Vidarbha Institute of science and Humanities, Amravati, 444 604 India.

^bDepartment of Physics, Sant Gadge Baba Amravati University, Amravati, 444 602 India.

* Corresponding author email: sandeepwaghuley@sgbau.ac.in

ABSTRACT :

The optical properties of copper oxide and bismuth oxide nanoparticles have been studied in the present research paper. The nanoparticles were synthesized by chemical method using sodium hydroxide as a templating agent. The synthesized materials were characterized by X-ray diffraction (XRD) and UV-Visible (UV-Vis) spectroscopy. In XRD study, the peaks show single phase monoclinic structure and particle size of copper oxide and bismuth oxide nanoparticles found to be 42.12 and 46.47 nm respectively. The absorption spectra of copper oxide and bismuth oxide nanoparticles have been recorded and determined the absorption peaks, approximately at 290 and 340 nm. The corresponding band gap values were estimated at 3.5 and 2.8 eV respectively.

KEYWORDS : Copper oxide; Bismuth oxide; Optical properties.

1. INTRODUCTION

All the aspects of material Science and Physics, metal oxides constitute the most diverse class of materials covering properties. In recent years, worldwide researchers have focus their attention towards materials having suitable properties with a variety of doping materials with which enhancement of properties can be done.

There are number of metal oxides available in environment but some of the metal oxides are most beneficial in accordance with their applications. Metal oxides have excellent thermal stability, good electrical and optical properties. Transition metals are large in number and have number of applications in different fields [1-2]. Among the oxides, transition metal copper oxide and bismuth oxide are of special importance due to their applications. Copper oxide is use for the magnetic storage device, solar energy transfer, sensors, super capacitors, chemical plants etc. Bismuth oxides is widely use in many applications such as fuel cells, medical field, gas sensing and catalysis process.

Copper oxide is a P-type semiconductor with a direct bandgap of 2.0 eV [3]. Copper oxide nanomaterial affects electron field emission properties due to their lower surface potential barrier than that of the metals. Copper oxide is considered as a potential field emitter, an efficient catalytic agent, as well as good gas sensing material. It also plays an important role in the optoelectronics and solar cell [4-5].

In particular, bismuth is suggested as an alternative to mercury for an environmental sensor. The advantageous analytical properties of bismuth are attributed to its fused alloy formation with different metal [6-8]. Bismuth oxide is a well-known transition metal oxide and it has been intensively studied due to interesting thermal and electrical transport properties [9]. Semimetal bismuth has a highly anisotropic fermi surface, low conduction band, effective mass and high electron mobility which is of great interest because of its size induced semimetal to semiconductor transition [10-13].

In the present work, the optical properties of copper oxide and bismuth oxide nanoparticles are highlighted using XRD and UV-Vis analysis.

2. EXPERIMENTAL

2.1 Materials

copper nitrate, bismuth nitrate, sodium hydroxide were used for synthesis of nanoparticles.

2.2 Synthesis of Copper oxide nanoparticles

2 gm of sodium hydroxide dissolved in 50 ml of distilled water then 0.25 M of copper nitrate were dissolved by constant stirring for 1 h. Blue colour precipitate of copper was collected by filtration. The obtained copper oxide nanoparticle was dried in a vacuum oven at 80 °C for 2hr. and then collected copper oxide nanoparticles.

2.3 Synthesis of Bismuth oxide nanoparticle

2 gm of sodium hydroxide dissolved in 50 ml of distilled water then 0.75 M of bismuth nitrate were dissolved by constant stirring for 1hr. white colour precipitate of bismuth was collected by filtration. The obtained bismuth oxide nanoparticle was dried in a vacuum oven at 80 °C for 2hr. and then collected bismuth oxide nanoparticles.

2.4. Characterization

Analysis of XRD and UV-Vis spectroscopy were confirmed the formation of oxide nanoparticles. X-ray diffraction (XRD) studies were carried out using Rigaku X-ray diffractometer. UV-Vis measurements were carried out on Perkin Elmer- Lambda 25 model.

3. RESULT AND DISCUSSION

3.1 XRD STUDY

Fig .1 Shows the XRD Pattern of prepared copper oxide nanoparticles. Diffraction pattern peak shows single phase monoclinic structure of copper oxide. The intensities and position peak are observed and compared with (JCPDS file no. 05-661).

The size of copper oxide crystalline was determined by using Debye - Scherrer's formula of eq. 1.

$$D = \frac{0.9\lambda}{\beta \cos\theta} \quad \text{-----} \quad (1)$$

Where, λ is wavelength of X ray (0.154059) nm

β is FWHM (full width at half maximum) of diffraction peak.

Θ is position angle.

D is the size of particle.

The main diffraction peaks of good resolution reflect the good crystalline size. The average grain size is approximately 46.12 nm

Fig 2 Shows XRD pattern of prepared bismuth oxide nanoparticle. Peak shows monoclinic structure of bismuth oxide in diffraction pattern. The average crystalline size which has been determined by Debye – Scherrer formula. Particle size obtained from XRD is 42.47 nm

The average particle size is less than 50nm are good agreement with the XRD result.

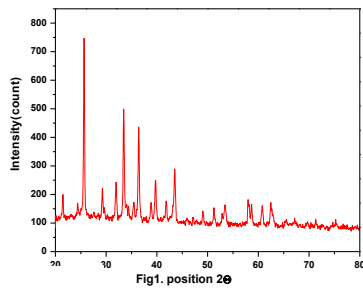


Fig.1 XRD of CuO

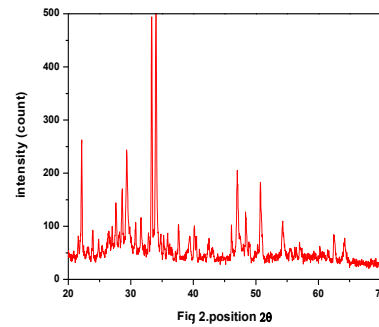


Fig.2 XRD of BiO

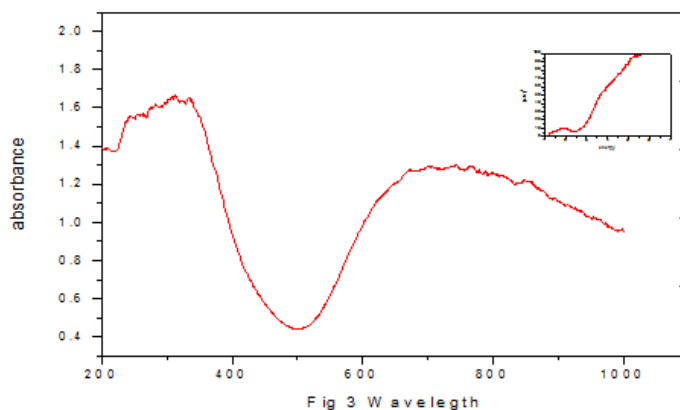
3.2 UV-Vis SPECTROSCOPY STUDY

For the determination of optical band gap energy of crystalline and amorphous material, optical absorption analysis is an important factor. To determine the nature and value of the band gap the fundamental absorption corresponds to the electron excitation from the valence band to the conduction band can be used. The optical band gap calculated from the following relation.

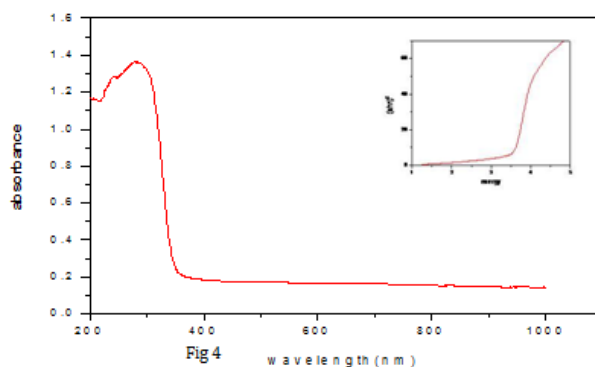
$$(\alpha h\nu)^n = A(h\nu - E_g)$$

Where absorption $h\nu$ is the incident photon energy. n is the exponent that determine the type of electronic transition causing the absorption and can take the value $\frac{1}{2}$ and 2 depending whether transition is direct or indirect respectively.

The absorption spectra of copper oxide and bismuth oxide nanoparticle have been recorded using lambda 25 UV –vis spectroscopy model at room temperature. The absorption peak is approximately 290 nm and 360nm and their corresponding band gap value is 3.5ev and 2.6ev respectively.



UV – vis absorption spectrum CuO



UV – vis absorption spectrum BiO

4.CONCLUSIONS

Copper and bismuth oxide nanoparticles has been successfully synthesized by chemical method. Optical properties of oxide nanoparticles confirmed by XRD and UV –visible techniques.

ACKNOWLEDGMENTS:

The authors are thankful to Head, Department of Physics, Sant Gadge Baba Amravati University, Amravati, for providing necessary facilities. One of the authors (K.G. Kalmegh) is thankful to Head, Department of Physics Govt .Vidarbh Institute of Science and Humanities, Amravati for suggestions in this regard.

REFERENCE

1. C.H. Chon, K.D. Kihm , Thermal conductivity Enhancement of Nanofluid by browian Motion, ASME Journal Heat transfer, 127 (2005) 8.P.810.
2. S.K. Das, et.al Temperature Dependence of Thermal Conductivity Enhancement for Nanofluids, ASME journal Heat transfer, 125 (2003), 4.P.567-574.
3. S.J. Pearton, C.R. Abernathy, M.E. overberg G.T. Thaler, D.P. Norton, N. Theodoropoulou, A.F. Hebard, Y.D. Park, F.Ren, J.Kim and L.A. Boatner, “wide band gap ferromagnetic semiconductors and oxides,” J.Appl. Phys, 93, 1-13 (2003).
4. R.K. Swarnkar, S.C. singh and R.Gopal “Optical Study of Copper-oxide colloidal NPS synthesized by pulsed laser Ablation in Aqueous media”, National laser Symposium, LASTEC New Delhi, Jan (2009) 7-10,
5. C.T. Hsieh, J.M. chen, H.H. Lin and H.C. Shih “Field Emission From Various CuO Nanostructures” Appl. Phys. Lett. 83, (2003) 3383.
6. J. Wang, D.Lu, S. Thongngamdee, Y. lin and O.A.Sadik, Talanta 69 (2006) 914-917.

7. S.B. Hocevar, B. Ogoreve, J. Wang, and B. Pihlar, *Electroanalysis* 14 (2002) 1707-1712.
8. G.Kefala, A.Economou and M.sofoniou, *Talanta* 08 (2006) 1013-1019.
9. X-chem, S.Chen, W.Huang, J.Zheng, Z.Li *Electrochim, Acta* 94 (2009) 7370-7373
10. J.Wang, X. Wang, Q. Peng, and Y. Inorg, *Chem* 43 (2004) 7552-7556.
11. X.Y. Liu, J.H.Zeng, S.Y.Zhang, R.B. Zheng, X.M. Liu and V.T. Qian, *ChemPhys – Lett.* 374 (2003) 348-352.
12. G.G. Briand, N. Burford, M.D. Eelman, N. Aumeerahly, Z. Chem T.S. Cameron and K. N. Robertson, *Inorg, Chem* 43 (2004) 495-650
13. Y.M.Lin, S.B. Cronin, J.Y. Ying, M.S. Dresselhaus and J.P.Heremans, *App. Phys, Lett.* 76 (2000) 3944-3946.



STUDY OF THE DENSITY OF LOCALIZED STATES IN $Zn_{1-x}Mn_xS$ CHALCOGENIDE SEMICONDUCTOR

D. Age^a, K. Rathod^a, F. Khan^a, M. T. Chakma^a, A. S. Khune^a, V. Khnadelwal^a, S. Thorat^a, P. Khedkar^a, S. Humbe^b, A. S. Dive^b, K. Gattu^b and Ramphal Sharma^{a, b*}

^aDepartment of Physics, Dr. Babasaheb Ambedkar Marathwada University, Aurangabad 431004, India.

^bThin Film and Nanotechnology Laboratory, Department of Physics, Dr. Babasaheb Ambedkar Marathwada University, Aurangabad 431004, India.

* Corresponding authors: -rps.phy@gmail.com

ABSTRACT :

In the present paper, pure and manganese-doped zinc oxide (Mn: ZnO) thin films based on the DFT theory systematically investigated. We calculate the exchange interaction parameters of a classical Heisenberg Hamiltonian for Mn-doped ZnO, Mn concentration between 0.10 and 0.20 % by an ab initio Korringa-Kohn-Rostoker coherent-potential approximation method in the framework of density functional theory (DFT). The Zn atoms of ZnO unit cell has easily substituted by Mn atoms along the [0001] direction. For the calculation, we have used a standard crystallographic information file (CIF) as data. When we have doped Mn in ZnO, it is observed that there is a decrease in the band gap and also show that some new intermediate state occurred at the Fermi energy level. Which proves the candidature of this interesting material engineering.

INTRODUCTION

Nanotechnology has brought revolution in the electronic world. It is the branch of physics that deals with making structures that are less than 100 nanometers and also involved study, control, and manipulation of them. Due to its extremely small size, it has proved a bonus to various electrical applications and hence to the industries. In the last decade, there is been a great demand for nanomaterial technology and hence a lot of work has been done in this field and still in progress.

In recent years, everyone is after the production of products which have uniformity in size and the particles are smaller in size and mostly the material is powder based. It is seen that nanoparticles have improved optical, electric and magnetic properties as compared to their bulk counterparts. This has led the majority of researchers to put their keen interest in it. In this experiment, we have studied the effects on ZnO when doped with Mn for different concentration. Also, we have seen that there is the formation of an intermediate band which helps in various electronic properties. And this has various technological applications. The Zinc oxide forms colorless hexagonal crystals or a white dusty powder. ZnO powder mainly used in a calamine lotion is made (1). It is also used in a host of other creams and ointments that are used to treat skin diseases. Zinc oxide is a basic ingredient without which piezo-electric converters, transparent conducting oxides, sensors, luminous diodes, and optoelectronic or spintronic components cannot be dreamt of. Also, zinc oxide-based semiconductors have its applications in transparent conductive layers in blue light-emitting diodes, liquid-crystal screens, visitors, and thin-film solar cells (2). The sizes of ZnO particles used for sunscreens are in the range of 20 to 60 nm. Before being added, these very small ZnO nanoparticles are coated with silicon or aluminum oxide. Manganese is a metal with important industrial metal alloy uses, particularly in stainless steels. In physical property, Manganese (Mn) is a silvery-gray metal that resembles iron. It is hard and very brittle, difficult to fuse, but easy to oxidize (3). Manganese

metal and its common ions are paramagnetic. Manganese tarnishes slowly in air and oxidizes ("rusts") like iron in water containing dissolved oxygen. In chemical property, The most common oxidation states of manganese are +2, +3, +4, +6, and +7, though all oxidation states from -3 to +7 have been observed(4).

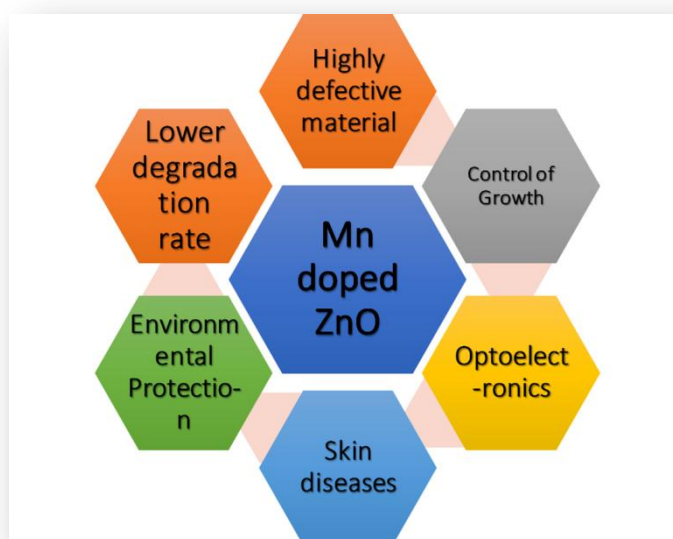


Fig. 1 (a, b). Shows the application of the different dopant into the pure and doped ZnO structure.

It is observed that pure ZnO has an energy band gap of ~ 3.3 eV at room temperature and binding energy as high as ~ 60 MeV. ZnO can also be used as a UV detector and is a metal oxide semiconductor. ZnO is a semiconducting material which shows its characteristics which are excellent for optoelectronics and solar cells(5). Among the II-VI semiconductors, although Cadmium Selenide and Cadmium Telluride have shown to be promising in solar cell applications, they are toxic and harmful to the environment. This type of semiconductor have great potential in various applications and hence many research projects have been made on Mn-ZnO like semiconductor recently. The importance, advantages of the doped system shown in **Fig. 1 (a)**.

Computational Details

In the first principles calculation taking into account fully self-consistent density functional theory (DFT) by solving the Kohn-Sham equation was performed using the MedeA-(VASP)Vienna ab initio simulation package with the plane wave pseudopotentials to carry out the calculation of geometry optimization and electronic structure. We have used the exchange-correlation term and the generalized gradient approximations (GGA) given by Perdew-Burke-Ernzerhof (PBE). We use norm-conserving pseudopotential for Zn and O atoms that indicates the non-relativistic effect. We used the Monkhorst-Pack scheme for k-points sampling of the Brillouin Zone (BZ) integration with $2 \times 2 \times 2$ for the ZnO structure. The structural optimization is obtained until the Hellmann-Feynman force acting on each atom is less than 10^{-3} eV/Å. The DFT equation is solved via the projector augmented wave method using a plane wave basis set as implemented in Vienna ab initio Simulation Package (VASP) interface with MedeA technology platform.

RESULT AND DISCUSSION:

Here, we have made the simulation using Generalised gradient approximation (GGA) of Density functional theory (DFT) with the help of VASP, we have studied the electronic structure and it agrees with the previously reported value. The standard crystallographic information file (CIF) data of the ZnO was used for the DFT simulation of the pure and doped system, we have used the structure with a space group of P6₃mc shown in **Fig. 2. (a)**. The lattice parameters of standard ZnO was $a=3.289$ Å and $c= 5.307$ Å respectively. Initially, we have optimized the pure unit cell and calculated the band structure (BS) and density of state

(DOS) for the same structure. Further, we have replaced the Zn atom with Mn and calculated the BS and DOS respectively.

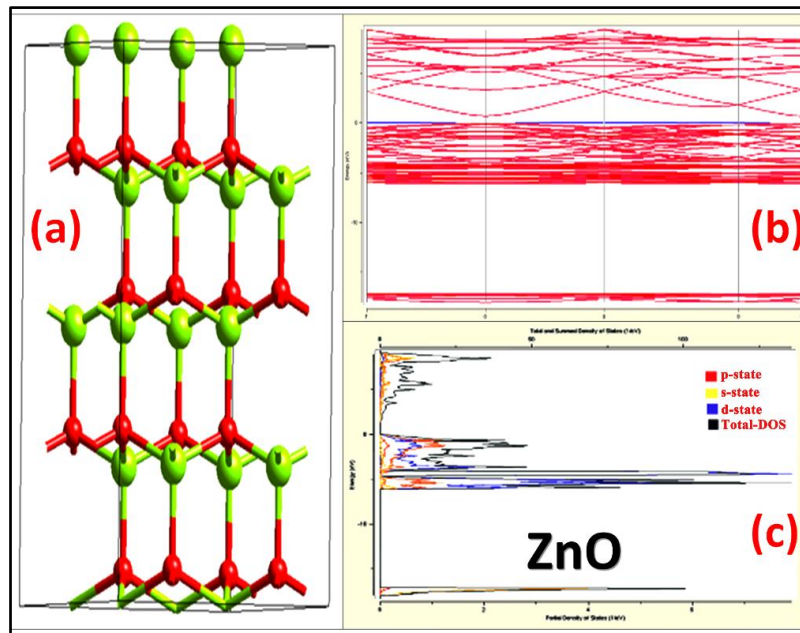


Fig. 2. (a) Show the optimized structure of pure ZnO super-cell, (b) band structure (diagram) of ZnO super-cell, (c) density of states with all the selected states.

For the pure ZnO super-cell, we got the bandgap energy value of ~ 1.2 eV (bulk-counterparts) at the high symmetry gamma (Γ) point in the Brillouin zone respectively. Also, it shows the direct bandgap nature of the optimized super-cell(6). The density of the state was also given reliable results which well matches with BS results. **Fig. 2(b)** shows the estimated band structure of the pure ZnO. From DOS ~ 1.5 eV bandgap energy value got for the DOS plot. There is no any intermediated state occurred here within the bandgap region also suggested by DOS showed in **Fig. 2 (c)**.

Fig. 3. (a) Show the optimized super-cell of the 1_Mn – ZnO. The same was used for the simulation of this specific concentration (0.10%). There is a drastic change in the band diagram has been showing here which includes some new band introduced at the Fermi energy level and some new intermediate states occurred. Specifically, at the 0.10 % doping concentration, there is one or two bands are crossing the Fermi energy level(7).The newly introduced bands are interestingly helping to charge transfer and technological application such as optoelectronics and window layer for photovoltaics. The bandgap value is reliably diminished here as compared to the pure ZnO semiconductor(8).

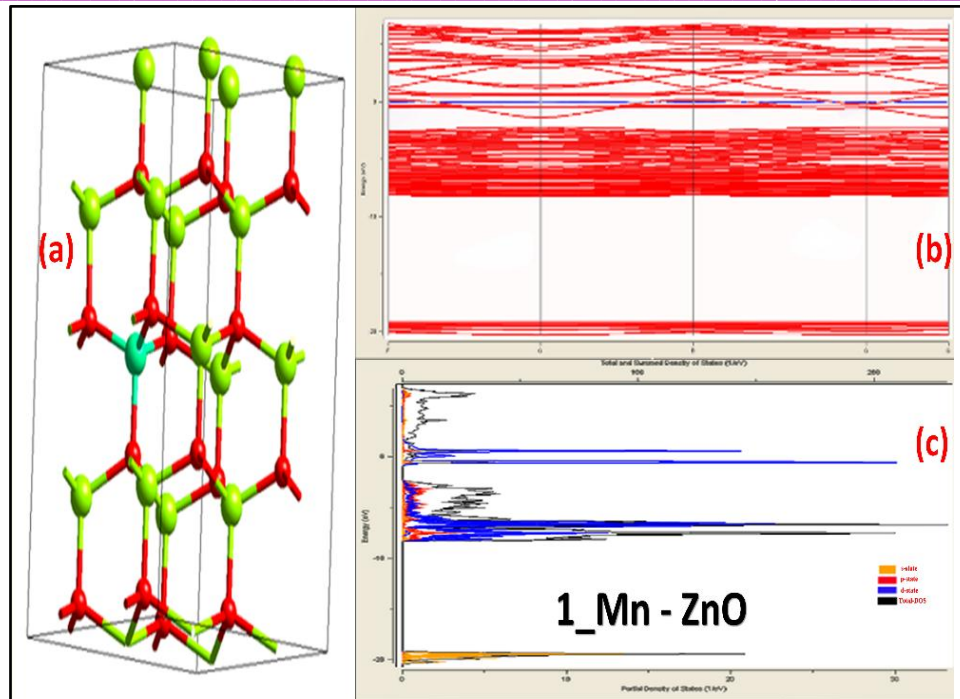


Fig. 3. (a) Show the optimized structure of 1_Mn - ZnO super-cell, (b) band structure (diagram) of 1_Mn - ZnO super-cell, (c) density of states with all the selected states.

After the incorporation of an Mn atom into the host semiconductor, the several changes occur in valance band and the conduction band of the pure ZnO. The same phenomenon is observed in the DOS result of this system(9). **Fig. 3. (c)** Shows the selected and deselected DOS of the 1_Mn - ZnO super-cell(9). Further, the 0.20% doping of Mn in ZnO system we get the interesting results(10). **Fig. 4. (a)** Show the optimized super-cell of the 2_Mn - ZnO in which 2 Mn atoms replaced with Zn atoms. The same was used for the simulation of this specific concentration (0.20%). The distinguishable changes have occurred into the band structure and density of states of the simulated system. The occurrence of some new band at the Fermi energy level and some new intermediate states occurred. Newly occurred intermediate states are more in number as we compare to (~ 0.10%) results(11). Which clearly sounds that more doping concentration will be also effective for the different technological application. At 0.20% doping concentration number of bands from the conduction band are crossing the Fermi energy level towards the valance band. The newly introduced bands are interesting helps to charge transfer and technological application such as optoelectronics and window layer for photovoltaics(12). The bandgap value is reliably diminished here as compared to the pure ZnO semiconductor. After the incorporation of an Mn atom into the host semiconductor, the several are changes occur in valance band and the conduction band of the pure ZnO. The same phenomenon is observed in the DOS result of this system. **Fig. 4. (c)** Shows the selected and deselected DOS of the 2_Mn - ZnO super-cell(13).

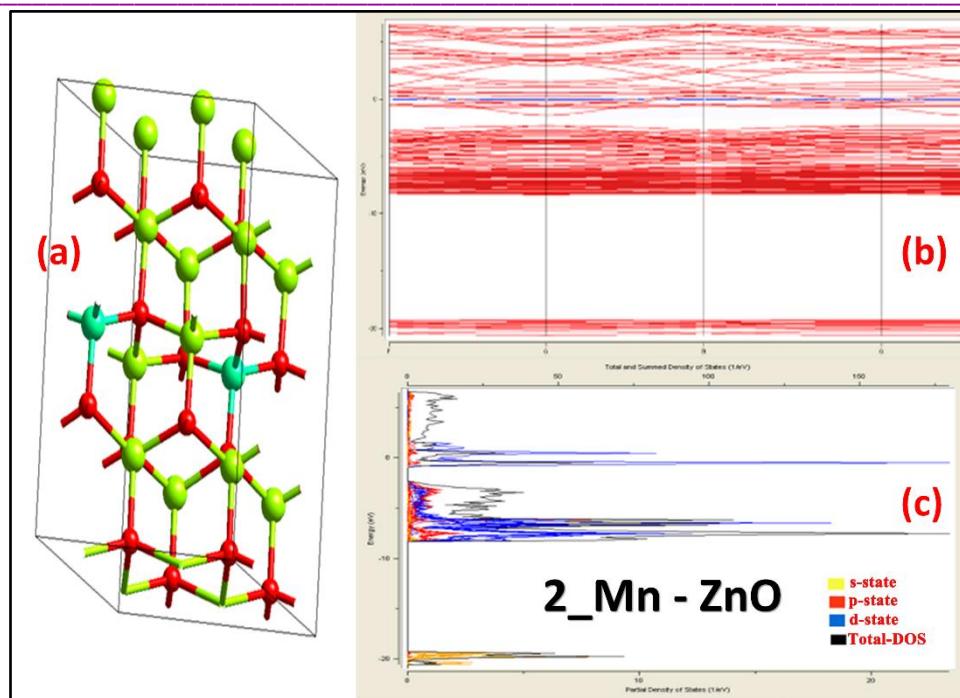


Fig. 4 (a). Show the optimized structure of 2_Mn - ZnO super-cell, (b) band structure (diagram) of 2_Mn - ZnO super-cell, (c) density of states with all the selected states and

CONCLUSION:

In this manuscript, with the application of DFT calculations, we have studied the electronic structure and bandgap properties of the Mn-ZnO for the 0.10 and 0.20% respectively. For the simulation and optimization we have used the standard CIF data of ZnO having space group of P6₃mc. For the optimized band structure and DOS shows approximately ~ 1.5 eV. Further, for the 0.10% of Mn, we get a decrease in bandgap energy as well as a new introduction of new intermediate band states. For 0.20% of doping the increase the intermediate states within the bandgap value at the Fermi energy level. This result confirms as Mn act as donor impurity and the band gap is decreased. This has further technological applications.

REFERENCES:

1. S. R. Christy, L. S. Priya, M. Durka, A. Dinesh, N. Babitha, S. Arunadevi, Simple Combustion Synthesis, Structural, Morphological, Optical and Catalytic Properties of ZnO Nanoparticles. *Journal of Nanoscience and Nanotechnology***19**, 3564-3570 (2019); published online EpubJun (10.1166/jnn.2019.16141).
2. O. O. Apeh, U. K. Chime, S. Agbo, S. Ezugwu, R. Taziwa, E. Meyer, P. Sutta, M. Maaza, F. I. Ezema, Properties of nanostructured ZnO thin films synthesized using a modified aqueous chemical growth method. *Materials Research Express***6**, (2019); published online EpubMay (10.1088/2053-1591/aadcd6).
3. C. Belkhaoui, N. Mzabi, H. Smaoui, Investigations on structural, optical and dielectric properties of Mn doped ZnO nanoparticles synthesized by co-precipitation method. *Materials Research Bulletin***111**, 70-79 (2019); published online EpubMar (10.1016/j.materresbull.2018.11.006).
4. P. Borylo, K. Matus, K. Lukaszewicz, J. Kubacki, K. Balin, M. Basiaga, M. Szindler, J. Mikula, The influence of atomic layer deposition process temperature on ZnO thin film structure. *Applied Surface Science***474**, 177-186 (2019); published online EpubApr (10.1016/j.apsusc.2018.03.169).
5. G. M. M. Gubari, I. M. S. M., N. P. Huse, A. S. Dive, R. Sharma, Synthesis and photosensor study of as-grown CuZnO thin film by facile chemical bath deposition. *AIP Conference Proceedings***1953**, 100072 (2018)10.1063/1.5033008).

6. A. S. Dive, K. P. Gattu, N. P. Huse, D. R. Upadhayay, D. M. Phase, R. B. Sharma, Single step chemical growth of ZnMgS nanorod thin film and its DFT study. *Materials Science and Engineering: B***228**, 91-95 (2018); published online Epub2018/02/01/ (<https://doi.org/10.1016/j.mseb.2017.11.018>).
7. S. Aksoy, Y. Caglar, Synthesis of Mn doped ZnO nanopowders by MW-HTS and its structural, morphological and optical characteristics. *Journal of Alloys and Compounds***781**, 929-935 (2019); published online EpubApr (10.1016/j.jallcom.2018.12.101).
8. K. Chebbah, R. Baghdad, A. Belfedal, A. Reggad, A. Zeinert, M. Clin, K. Zellama, Structural and Optical Properties of N and Mn co-doped ZnO Thin Films Grown by Ultrasonic Spray Pyrolysis Method. *Journal of Nanoelectronics and Optoelectronics***14**, 39-49 (2019); published online EpubJan (10.1166/jno.2019.2428).
9. M. F. Cerqueira, T. Viseu, J. A. de Campos, A. G. Rolo, T. de Lacerda-Aroso, F. Oliveira, I. Bogdanovic-Radovic, E. Alves, M. I. Vasilevskiy, Raman study of insulating and conductive ZnO:(Al, Mn) thin films. *Physica Status Solidi a-Applications and Materials Science***212**, 2345-2354 (2015); published online EpubOct (10.1002/pssa.201532162).
10. M. Chakraborty, A. Ghosh, R. Thangavel, Experimental and theoretical investigations of structural and optical properties of copper doped ZnO nanorods. *Journal of Sol-Gel Science and Technology***74**, 756-764 (2015); published online EpubJun (10.1007/s10971-015-3660-1).
11. H. Saal, M. Binnewies, M. Schrader, A. Borger, K. D. Becker, V. A. Tikhomirov, K. Jug, Unusual Optical Properties of Mn-doped ZnO: The Search for a New Red Pigment-A Combined Experimental and Theoretical Study. *Chemistry-a European Journal***15**, 6408-6414 (2009)10.1002/chem.200802667).
12. L. Wu, T. J. Hou, Y. Wang, Y. F. Zhao, Z. Y. Guo, Y. Y. Li, S. T. Lee, First-principles study of doping effect on the phase transition of zinc oxide with transition metal doped. *Journal of Alloys and Compounds***541**, 250-255 (2012); published online EpubNov (10.1016/j.jallcom.2012.06.091).
13. J. Lu, H. Wang, Significant infrared lateral photovoltaic effect in Mn-doped ZnO diluted magnetic semiconducting film. *Optics Express***20**, 21552-21557 (2012); published online EpubSep (10.1364/oe.20.021552).



EFFECT OF Pb AND Si DOPING ON THE ELECTRONIC STRUCTURE OF MgO: A DENSITY FUNCTIONAL THEORY INVESTIGATION

F. Khan^a, M. T. Chakma^a, A. S. Khune^a, V. Khnadelwal^a, D. Age^a, K. Rathod^a, S. Thorat^a, P. Khedkar^a, S. Humbe^b, M. E. Sonawane^b, A. S. Dive^b, K. Gattu^b and Ramphal Sharma^{a, b*}

^aDepartment of Physics, Dr. Babasaheb Ambedkar Marathwada University, Aurangabad 431004, India

^bThin Film and Nanotechnology Laboratory, Department of Physics, Dr. Babasaheb Ambedkar Marathwada University, Aurangabad 431004, India

* Corresponding authors: -rps.phy@gmail.com

ABSTRACT :

Application of density functional theory the electronic properties and the trends of the sample MgO have been studied by doping it with Si and Pb separately. With the doping of Si, it was found that there is a change in the geometrical structure as well as the band gap. This agrees well with the theoretical computations reported earlier and the same was performed by doping with Pb, the results henceforth were found to be changed in electronic properties. In both the cases, the Mg atom has been replaced by Si and Pb independently which shows increment in band gap energy after assembled with Si and extreme decrement after Pb doping. It is observed that there is an increase in the band gap when MgO is doped with Si and decrease when doped with Pb. Several calculated results have been compared with available experimental and other theoretical data.

INTRODUCTION

In the contemporary world, there is a dire need of a better and compact technology and nanotechnology has its answers. Therefore, nanotechnology is the most uprising and developing field at present (1). Nanotechnology deals with the study, control, and manipulation of materials at the nanoscales, typically having dimensions less than 100 nm. Recently, the synthesis of metal oxide nanomaterials has drawn a large attraction of researchers towards itself due to its potential application (2).

Probably, in most of the industries, they believe in producing their products in the form of fine sized powders and materials (3). The improvement in the uniformity of the size and production of particles of smaller size has been a great trend among the industries (4). As we study the bulk counterparts of the same nanomaterials it is found to have a substantial increase in the electric, optical and magnetic properties and this leads to a subject of interest for the researchers for the potential technological application (5).

The objective of our experiment is to study the effects on band gaps when MgO is doped with Si and Pb separately which will help in various electronic properties. Magnesium oxide (MgO) has been a spark for us due to its high ionic character, simple stoichiometry and crystal structure (6). Due to its good reactivity and vital applications in chemistry, physics and material sciences, MgO is a great place in the researcher community. Exhibiting a rock salt structure, they have a great number of electronics and structural geometries that describes metallic, semiconductor and insulator character, and it can be prepared in widely variable particle sizes and shapes (7). It is seen that nanocrystalline MgO particles exhibit high specific surface and reactivity, because of its high concentration of edge/corner sites.

As we dope MgO with Si, surely there is the formation of SiO₂, alias Silica. Molar mass of SiO₂ is 60.1 g/mol and its melting point and boiling point are 1710°C and 2230°C respectively. Silicon dioxide is stable in water and at high temperature. Due to its high availability, modern technology uses Silicon oxide materials in various fields (8). The semiconductor devices have a basic need for chemical stability and good

electrical insulation properties for its efficiency. The different applications of Si doping into MgO shown in **Fig. 1(a)(9)**. When our sample is doped with lead, it forms a lead oxide (PbO). Lead oxide is one of the most promising photoconductive materials(10).The four most important criteria when potential x-ray photoconductors are considered include: (1) high conversion gain; (2) high x-ray absorption efficiency; (3) compatibility with large areadetector technology and (4) good photoconductive properties,PbO satisfies the first three criteria shown in **Fig. 1(b)(11)**.In this work, we have systematically investigated the electronic structures by DFT of MgO doped with Si and Pb under a concentration of 0.10 % respectively. We have investigated both the cases, in which dopant atoms replace the Mg atom and calculated the changed band gaps and density of states.

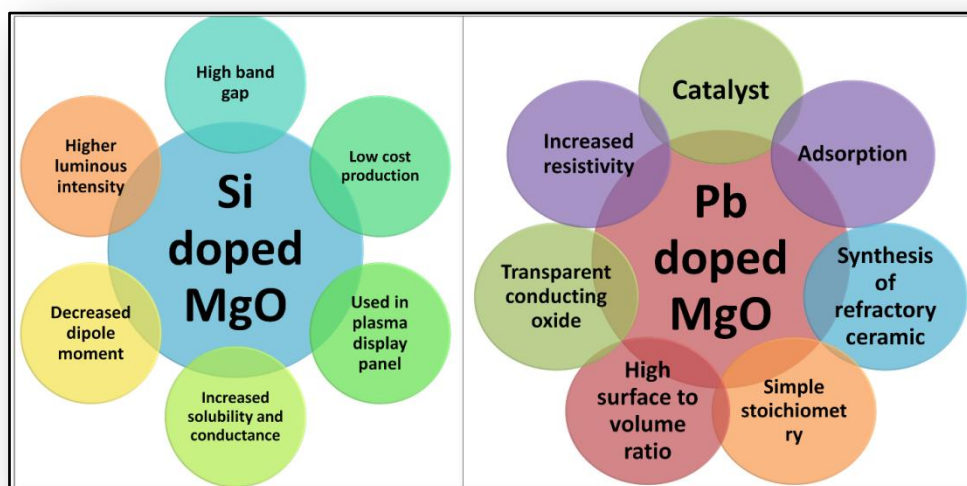


Fig. 1 (a, b). Shows the application of the different dopant into the pure MgO structure.

COMPUTATIONAL DETAILS:

Two different quantum mechanical approaches, namely, the density functional theory (DFT) and Hartree–Fock method (HF), are used in computer simulations of interface systems. However, there is a strong separation of these methods depending on the periodicity of the model used. DFT theory is generally applied for treating a 3D periodical slab model and the HF approximation for treating a 2D periodical slab model. Also, the DFT calculations are usually made with the plane-wave (PW) basis, whereas, HF calculations are based on the linear combination of atomic orbital (LCAO). But, HF results in more approximate and inanimate solutions. So, we focus on DFT and solve the problem by DFT analysis. Hence in this paper, we used the density functional theory (DFT) which was performed using the MedeA-(VASP) Vienna ab initio simulation package with the plane-wave pseudo-potentials, to carry out the calculations of geometry optimization and electronic structures(12). The Brillouin zone integration was performed using $1 \times 2 \times 1$ points for the cells. In an organized way the Si is doped in the MgO system and in another case, Pb is doped in the same. The DFT calculations were performed using generalized gradient approximation (GGA) functional with Perdew-Burke-Ernzerhof (PBE) to describe the electron-electron exchange and correlation effects. The DFT equations were solved via the projector augmented wave method using a plane wave basis set as implemented in Vienna Ab Initio Simulation Package (VASP) interfaced with the MedeA technology platform(13).

RESULT AND DISCUSSION:

Using Generalised gradient approximation (GGA) of Density functional theory(DFT)with the help of Vienna Ab initio Simulation Package (VASP), we have studied the bandgap structure and it agrees with the experimental value. For the DFT simulation of the pure and doped system, we have used the standard crystallographic information file (CIF) data of the MgO structure with a space group of Fm-3m shown in **Fig. 2. (a)**. The lattice parameters of standard MgO are found as $a=4.257\text{\AA}$. Initially, we have optimized the pure

unit cell and calculated the band structure (BS) and density of state (DOS) for the same structure(14). Further, we have replaced the Mg atom with Pb and Si respectively and calculated the BS and DOS respectively.

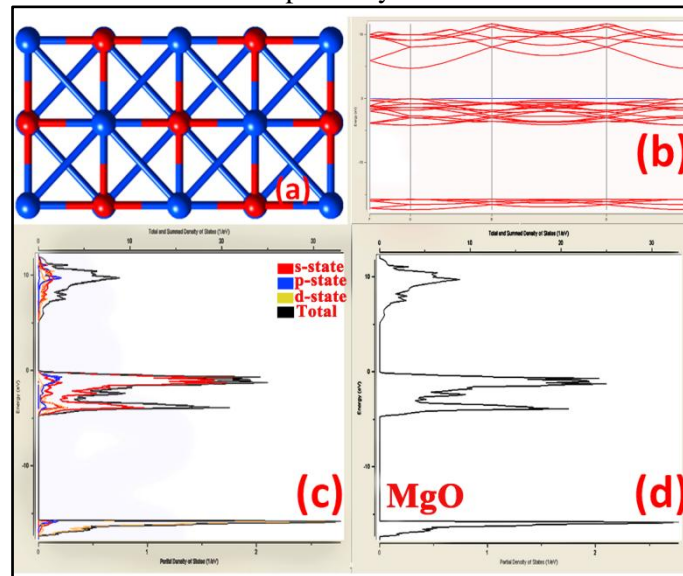


Fig. 2. (a) Show the optimized structure of pure MgO super-cell, (b) band structure (diagram) of MgO super-cell, (c) density of states with all the selected states and (d) Total density of states of MgO super-cell.

For the pure MgO super-cell, we got the bandgap energy value of $\sim 4.7\text{eV}$ at the high symmetry gamma (Γ) point in the Brillouin zone respectively. Also, it shows the direct bandgap nature of the optimized super-cell. The density of the state was also given reliable results which well matches with BS results. Approximately 4.5 eV bandgap energy value got for the DOS plot. DOS also suggest that there is no any intermediated state occurred here within the bandgap region(15). There is no d-state present for pure MgO DOS because there is no d-state present for a single Mg-atom. **Fig.2. (d)**Show the total density of states with all the states is deselected.

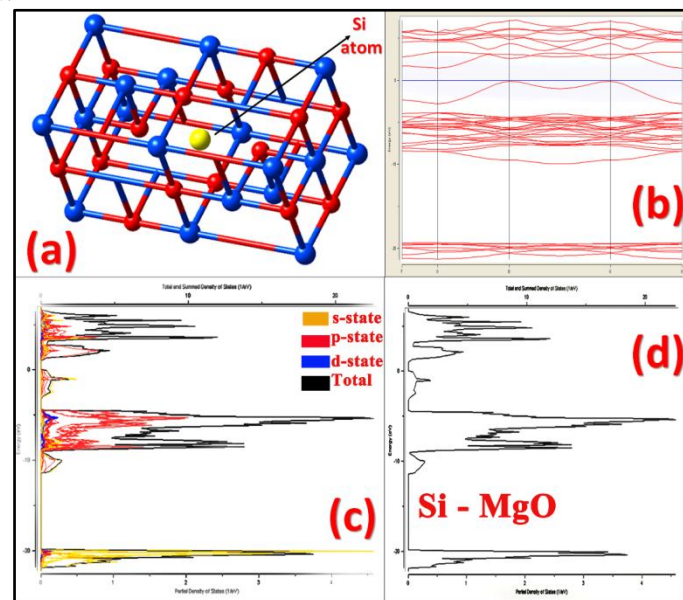


Fig. 3. (a) Show the optimized structure of 1_Si - MgO super-cell, (b) band structure (diagram) of 1_Si - MgO super-cell, (c) density of states with all the selected states and (d) Total density of states of 1_Si - MgO super-cell.

Fig. 3. (a) Show the optimized structure of the 1_Si – MgO super-cell the same was used for the simulation of this concentration. There is a drastic change in the band diagram has been showing here. As we have seen the direct-band of the pure MgO structure instantly changes to indirect band-gap material after the 1 Si atom replaced with an Mg atom. After the incorporation of a Si atom into the host semiconductor, the several changes occur in valance band of the pure MgO(16). The same phenomenon is observed in the DOS result of this system. Here we can easily find there is no. of ‘s’ and ‘p’ states occurred at the Fermi energy or zero energy. Also, there are no. of new states introduced in both conduction and valance band side of the Si-MgO structure. The newly occurred states could be helpful in the different technological and opto-electronic applications. **Fig. 3. (c, d)** shows the selected and deselected DOS of the 1_Si - MgO super-cell.

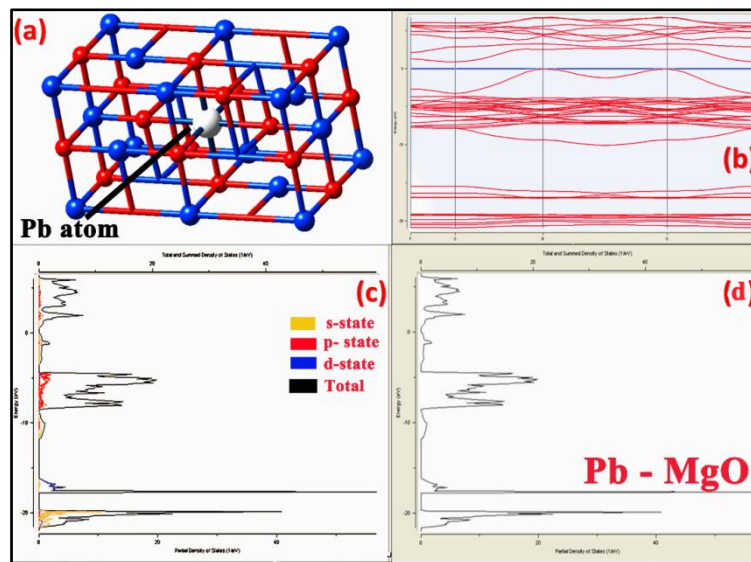


Fig. 4 (a). Show the optimized structure of 1_Pb - MgO super-cell, (b) band structure (diagram) of 1_Si - MgO super-cell, (c) density of states with all the selected states and (d) Total density of states of 1_Pb - MgO super-cell.

Fig. 4. (a) Show the optimized super-cell of the 1_Pb – MgO. The same was used for the simulation of this specific concentration (0.10%). There is a drastic change in the band diagram has been showing here. As we have seen the direct-band of the pure MgO structure instantly changes to indirect band-gap material after the 1 Pb atom replaced with an Mg atom. But, the bandgap value is consistently decreased here as compared to the pure MgO semiconductor. After the incorporation of a Pb atom into the host semiconductor, the several changes occur in valance band of the pure MgO. The same phenomenon is observed in the DOS result of this system. Here we can easily find there is no. of ‘s’ and ‘p’ states occurred at the Fermi energy or zero energy. Also, there are no. of new states introduced in both conduction and valance band side of the Pb-MgO structure. **Fig. 4. (c, d)** shows the selected and deselected DOS of the 1_Pb - MgO super-cell. The newly occurred states near to the Fermi energy will definitely prove the candidature of the Pb doped MgO semiconductor is very much helpful for the technological applications(17).

CONCLUSION:

In the paper, through DFT calculations, the electronic structure and the band gap energies of pure and doped MgO have been studied. The optimized super-cell were used for the calculation having space group of Fm-3m. The DFT result confirms that there is an increase in the band gap of MgO when doped with Si and also changed the nature of semiconductor from direct-band to indirect band semiconductor. For the pure MgO, we got the E_g of ~ 4.7 eV. Further, the same structure we assembled with the Pb atom and we get a different result as Si doping. Pb doping is helped not only to decrease in band gap value but also it changes direct-band to the indirect-bandgap semiconductor. The astonishing band engineering has a potential for photovoltaic, thermoelectric and optoelectronic applications.

REFERENCE

1. J. More-Chevalier, S. Cichon, J. Bulir, M. Poupon, P. Hubik, L. Fekete, J. Lancok, Electrical and optical properties of scandium nitride nanolayers on MgO (100) substrate. *Aip Advances***9**, (2019); published online EpubJan (10.1063/1.5056245).
2. H. Y. Lee, C. W. Lin, C. T. Lee, Aluminum-nanosphere-stacked MgNiO metal-semiconductor-metal ultraviolet photodetectors. *Journal of Alloys and Compounds***773**, 210-216 (2019); published online EpubJan (10.1016/j.jallcom.2018.09.256).
3. B. S. Tao, P. Barate, X. Devaux, P. Renucci, J. Frougier, A. Djeflal, S. H. Liang, B. Xu, M. Hehn, H. Jaffres, J. M. George, X. Marie, S. Mangin, X. F. Han, Z. G. Wang, Y. Lu, Atomic-scale understanding of high thermal stability of the Mo/CoFeB/MgO spin injector for spin-injection in remanence. *Nanoscale***10**, 10213-10220 (2018); published online EpubJun (10.1039/c8nr02250j).
4. W. G. Liao, L. Wang, L. Chen, W. Wei, Z. Zeng, X. W. Feng, L. Huang, W. C. Tan, X. Huang, K. W. Ang, C. X. Zhu, Efficient and reliable surface charge transfer doping of black phosphorus via atomic layer deposited MgO toward high performance complementary circuits. *Nanoscale***10**, 17007-17014 (2018); published online EpubSep (10.1039/c8nr04420a).
5. I. E. Castelli, S. G. Soriga, I. C. Man, Effects of the cooperative interaction on the diffusion of hydrogen on MgO(100). *Journal of Chemical Physics***149**, (2018); published online EpubJul (10.1063/1.5029329).
6. M. Ishikawa, M. Tsukahara, S. Honda, Y. Fujita, M. Yamada, Y. Saito, T. Kimura, H. Itoh, K. Hamaya, Crystal orientation effect on spin injection/detection efficiency in Si lateral spin-valve devices. *Journal of Physics D-Applied Physics***52**, (2019); published online EpubFeb (10.1088/1361-6463/aaf37c).
7. B. C. Sertel, N. A. Sonmez, M. D. Kaya, S. Ozcelik, Development of MgO:TiO₂ thin films for gas sensor applications. *Ceramics International***45**, 2917-2921 (2019); published online EpubFeb (10.1016/j.ceramint.2018.11.079).
8. E. Jimenez-Izal, H. C. Zhai, J. Y. Liu, A. N. Alexandrova, Nanoalloying MgO-Deposited Pt Clusters with Si To Control the Selectivity of Alkane Dehydrogenation. *Acs Catalysis***8**, 8346-8356 (2018); published online EpubSep (10.1021/acscatal.8b02443).
9. P. C. Lou, S. Kumar, Generation and detection of dissipationless spin current in a MgO/Si bilayer. *Journal of Physics-Condensed Matter***30**, (2018); published online EpubApr (10.1088/1361-648X/aab1e2).
10. A. M. El Sayed, Modification of the micro-structural and optical properties of nanoparticulate Pb-doped magnesia thin films. *Materials Research Express***5**, (2018); published online EpubNov (10.1088/2053-1591/aadc7b).
11. C. B. Yeager, S. Trolrier-McKinstry, Epitaxial Pb(Zr-x,Ti1-x)O-3 (0.30 <= x <= 0.63) films on (100)MgO substrates for energy harvesting applications. *Journal of Applied Physics***112**, (2012); published online EpubOct (10.1063/1.4754015).
12. N. P. Huse, A. S. Dive, K. P. Gattu, R. Sharma, An experimental and theoretical study on soft chemically grown CuS thin film for photosensor application. *Materials Science in Semiconductor Processing***67**, 62-68 (2017); published online Epub2017/08/15/ (<https://doi.org/10.1016/j.mssp.2017.05.010>).
13. G. M. M. Gubari, S. M. Ibrahim Mohammed, N. P. Huse, A. S. Dive, R. Sharma, An Experimental and Theoretical Study of Cu_{0.2}Zn_{0.8}S Thin Film Grown by Facile Chemical Bath Deposition As an Efficient Photosensor. *Journal of Electronic Materials***47**, 6128-6135 (2018); published online Epub2018/10/01 (10.1007/s11664-018-6491-3).
14. A. S. Dive, K. P. Gattu, N. P. Huse, D. R. Upadhayay, D. M. Phase, R. B. Sharma, Single step chemical growth of ZnMgS nanorod thin film and its DFT study. *Materials Science and Engineering: B***228**, 91-95 (2018); published online Epub2018/02/01/ (<https://doi.org/10.1016/j.mseb.2017.11.018>).
15. B. Cheng, H. W. Qin, L. Liu, J. H. Xie, J. F. Hu, Mechanism of polar catastrophe cancelling induced by charge compensation for epitaxy gamma-Fe₂O₃ film on MgO(001) substrate: A theoretical investigation. *Superlattices and Microstructures***120**, 377-381 (2018); published online EpubAug (10.1016/j.spmi.2018.05.065).
16. A. Miyamoto, H. Kikuchi, H. Onuma, H. Tsuboi, M. Koyama, N. Hatakeyama, A. Endou, H. Takaba, M. Kubo, C. A. Del Carpio, Electronic structure and electrical conductivity of MgO protecting layer in

-
- plasma-display panels: A tight-binding quantum chemical study. *Journal of the Society for Information Display***15**, 307-313 (2007)10.1889/1.2739800).
17. R. Topolnicki, R. Kucharczyk, Early stages of growth of Pb, Sn and Ge on Ru(0001): A comparative density functional theory study. *Thin Solid Films***665**, 123-130 (2018); published online EpubNov (10.1016/j.tsf.2018.08.040).



A DFT STUDY OF THE EFFECTS OF Cd DOPING ON ELECTRONIC STRUCTURE AND BANDGAP ENERGIES OF ZnO

S. Thorat^a, P. Khedkar^a, F. Khan^a, M. T. Chakma^a, A. S. Khune^a, V. Khnadelwal^a, D. Age^a, K. Rathod^a, S. Humbe^b, D. Tonpe^b, A. S. Dive^b, K. Gattu^b and Ramphal Sharma^{a, b*}

^aDepartment of Physics, Dr. Babasaheb Ambedkar Marathwada University, Aurangabad 431004, India.

^bThin Film and Nanotechnology Laboratory, Department of Physics, Dr. Babasaheb Ambedkar Marathwada University, Aurangabad 431004, India.

* Corresponding authors: -rps.phy@gmail.com

ABSTRACT :

Tailoring the energy gap of ZnO through the doping of Cd into the ZnO an intriguing material for the photovoltaic and optoelectronic application. Inappropriately, the Cd doping into the ZnO is unstable, because of the structural differences between the pure hexagonal ZnO and cubic Cd. Here, we report the density functional theory (DFT) study of wurtzite (WZ) ZnO doped with up to 0.20% of the Zn atoms were replaced by a Cd. The optimized ZnO showed a band gap energy of ~ 1.5eV while alloying with Cd dopants efficiently reduce the electronic band gap of ZnO and in turn, the absorption edge and optical energy gap are red-shifted. For the higher doping new bands are occurred near to the Fermi energy which helps to reduce the band gap energy. Therefore the ZnO alloyed with Cd is the potential alloy in the field opto-electronic or solar energy applications.

INTRODUCTION

ZnO is a stimulating and multifunctional semiconductor that plays a principal role in II-VI semiconductor family. The wide and direct band gap of ~ 3.2 eV, intrinsically transparent nature over the whole visible and ultraviolet range, abundant availability, low cost, high chemical and make ZnO particularly attractive for photovoltaic (PV) and solar cell applications. ZnO is often highly doped with atomic impurities, and there now exists considerable academic research efforts to control ZnO doping to both improve existing physical properties and add new material dimensionalities, including varying the optoelectronic, magnetic, magneto-optic, optoelectronic properties(1). The current ZnO application range includes many transparent electronic and photonic devices, such as solar cells, blue and ultraviolet light-emitting diodes, flat panel displays, among many others. ZnO based transparent conducting nanotechnology is moderately new science, it has innumerable applications in everyday life. Nanotechnology is the design characteristics production and application of structures, devices, and system by controlling shape and size at a nanometric scale(2). The quantum mechanical effects are important and so nanotechnology definition shifted from a particular technological goal to research and technologies that deal with the special properties of matter which occur below the given size threshold. The main intent of nanotechnology is to assemble self-organized nanosystem that is ultra small in size exhibit super sensitivity, extraordinary multi-functionality, and extremely low power utilization so scientists currently debate the future implications of nanotechnology(3). The study of the effects on band gaps when ZnO is doped with Cd is the main objective of our experiment which will help in various electronic properties. It will increase appreciably the conducting behavior of ZnO and amplify other properties. Hence the properties of ZnO doped with Cd are studied.

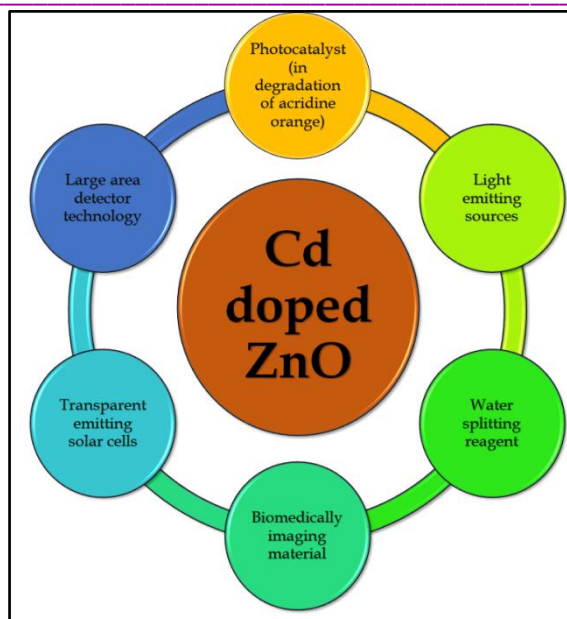


Fig. 1. Application of pure and doped ZnO.

We have to increase electronic states of semiconductor ZnO, so we choose Cd. For reducing the band gap of ZnO, the Cd is most suitable because one and only one Cd can decrease the band gap of ZnO up to ~ 3.2 eV. The Zn and Cd having covalent radii 122 and 144pm respectively. And Ionic radii of Zn is 88pm and Cd is 109pm(4). With few deformations, Cd can set in place of Zn in ZnO lattice structure as Cd having very large radii. ZnO: Cd is formed when we doped ZnO with Cd. ZnO: Cd is stable in air and at high temperature. The semiconductor like Cd-ZnO have great potential in various applications and hence many research projects have been made recently(5). The importance, advantages of the doped system shown in **Fig. 1 (a)**.

COMPUTATIONAL DETAILS

Here, the theoretical calculations in the framework of ab initio density functional theory have been performed. The entire DFT calculations have been performed using the Vienna ab initio simulation MedeA-VASP code, along with the MedeA software package. All the systems have been studied under generalized gradient approximation (GGA) with Perdew–Burke–Ernzerhof (PBE) exchange and correlation. Throughout the calculations, the size of the supercell has been considered to be 2 x 2 x 2 unit cell. The structural optimization is obtained until the Hellmann-Feynman force acting on each atom is less than 10⁻³ eV/Å. The DFT equation is solved via the projector augmented wave method using a plane wave basis set as implemented in Vienna ab initio Simulation Package (VASP) interface with MedeA technology platform. The Brillouin zone (BZ) of the supercells has been divided by 2 x 2 x 2 Monkhorst–Pack (MP) k-points.

RESULT AND DISCUSSION:

Using generalized gradient approximation (GGA) of Density functional theory (DFT) with the help of MedeA-VASP simulation package, we have studied the electronic structure and it agrees with the earlier reported. The internationally recognized and published standard crystallographic information file (CIF) data used for the optimization and simulation of ZnO and Cd-doped ZnO system, we have used the structure with a space group of P6₃mc shown in **Fig. 2. (a)**(6). The lattice parameters of the standard ZnO structure was a=3.289 Å and c= 5.307Å respectively and having stable hexagonal wurtzite structure. Initially, we have optimized the pure unit cell and calculated the band structure (BS) and density of state (DOS) for the same structure. Further, we have replaced the Zn atom with Cd and calculated the BS and DOS respectively(7). For the pure ZnO super-cell, we got the bandgap energy value of ~ 1.2 eV (bulk-counterparts) at the high symmetry gamma (g) point in the Brillouin zone respectively. Also, it shows the direct bandgap nature of the optimized super-cell(8). The density of the state was also given reliable results which well matches with BS

results. **Fig. 2(b)** shows the estimated band structure of the pure ZnO. From DOS ~ 1.5 eV bandgap energy value got for the DOS plot(9). There is no any intermediated state occurred here within the bandgap region also suggested by DOS showed in **Fig. 2 (c)**.

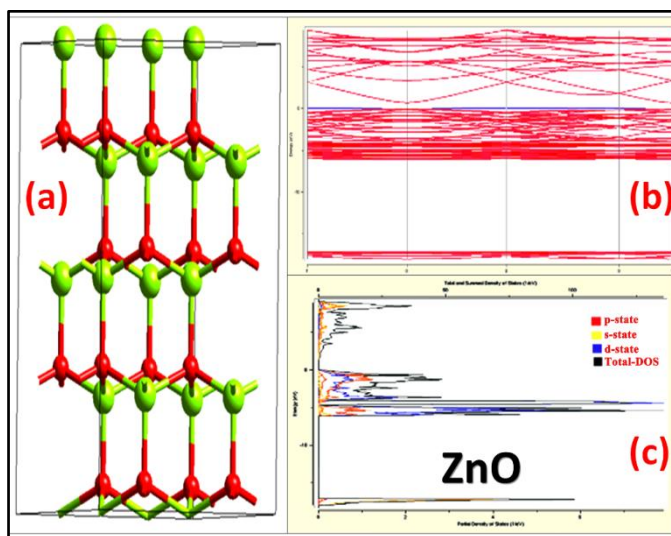


Fig. 2. (a) Show the optimized structure of pure ZnO super-cell, (b) band structure (diagram) of ZnO super-cell, (c) density of states with all the selected states.

Fig. 3. (a) Show the optimized super-cell of the 1_Cd – ZnO. The optimized Cd-ZnO further used for the simulation of this doping concentration as one atom of Cd (0.10%). The doping effect can easily differentiate here as bandgap value was decreased from ~ 1.5 eV to 0.7 eV. There is a bandgap difference in the experimental and theoretical results is a well-known problem because of nano and bulk materials bandgap difference(10). Some new band introduced at the Fermi energy level and some new intermediate states occurred. The newly introduced bands are fascinatingly helping to charge transfer and technological application such as optoelectronics and window layer for photovoltaics(11). The bandgap value is reliably diminished here as compared to the pure ZnO semiconductor. After the incorporation of an atom into the host semiconductor, the several changes occur in valance band and the conduction band of the pure ZnO(12). The same phenomenon is observed in the DOS result of this system. **Fig. 3. (c)** Shows the selected and deselected DOS of the 1_Cd - ZnO super-cell. Further, the 0.20% doping of Cd in ZnO system we get the interesting results.

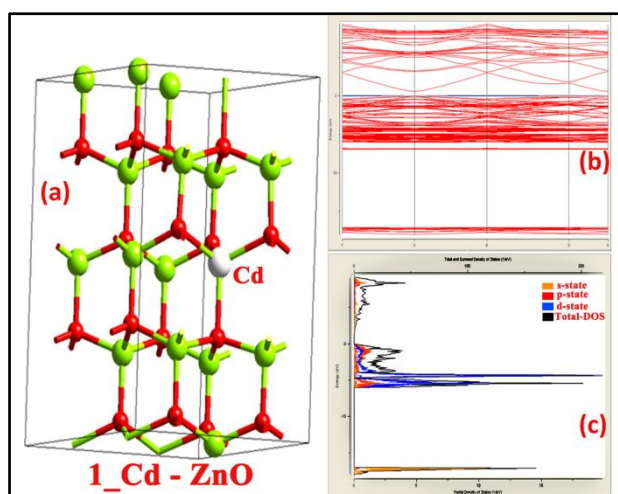


Fig. 3. (a) Show the optimized structure of 1_Cd - ZnO super-cell, (b) band structure (diagram) of 1_Cd - ZnO super-cell, (c) density of states with all the selected states.

Fig. 4. (a) Show the optimized super-cell of the 2_Cd – ZnO in which 2 Cd atoms substituted with Zn atoms in the initially optimized ZnO unit cell. The distinct deviation have arisen into the band structure and density of states of the simulated system. The occurrence of some new band at the Fermi energy level and some new states occurred at conduction band. Also, there are several new states occurred on DOS graph of 0.20% Cd-ZnO below the Fermi energy level. Newly occurred states are more in number as we compare to (~ 0.10%) results. Which clearly echoes that more doping concentration will have different technological applications(5). At 0.20% doping concentration number of bands from the conduction band are not crossing the Fermi energy level since we could say that higher doping concentration also keeps ZnO indirect band semiconductor. The newly introduced band's conduction band region are interesting and helps to charge transfer and technological application such as a photodetector, visible light sensors and window layer for photovoltaics. The bandgap value is reliably diminished here as compared to the pure ZnO semiconductor. After the incorporation of an atom into the host semiconductor, the several are changes occur in valance band and the conduction band of the pure ZnO(13). The same phenomenon is observed in the DOS result of this system. **Fig. 4. (c)** Shows the selected and deselected DOS of the 2_Cd - ZnO super-cell.

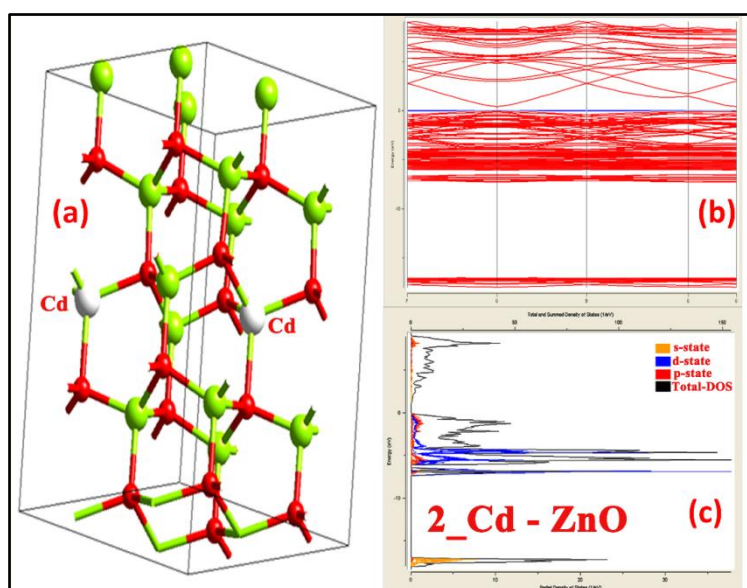


Fig. 4 (a). Show the optimized structure of 2_Cd - ZnO super-cell, (b) band structure (diagram) of 2_Cd - ZnO super-cell, (c) density of states with all the selected states and

CONCLUSION:

In the present manuscript, we have successfully performed the reported results based on the electronic structure and band gap properties investigation of pure and Cd-doped ZnO semiconductor. For this, we have used the standard CIF data file as input file space group of P6_3mc. We have studied the electronic structure and bandgap properties of the Cd-ZnO for the 0.10 and 0.20% respectively. For the optimized band structure and DOS shows approximately ~ 1.5 eV. For the 0.10% of Cd, we get a decrease in bandgap energy as well as a new introduction of new states in the conduction band region. For 0.20% of doping, there is a strong decrease in band gap energy and also shown newly occurrence of states. The results reported here will have several technological applications and will definitely attract the researcher community.

REFERENCES:

1. O. O. Apeh, U. K. Chime, S. Agbo, S. Ezugwu, R. Taziwa, E. Meyer, P. Sutta, M. Maaza, F. I. Ezema, Properties of nanostructured ZnO thin films synthesized using a modified aqueous chemical growth method. *Materials Research Express* **6**, (2019); published online EpubMay (10.1088/2053-1591/aadcd6).

2. P. Borylo, K. Matus, K. Lukaszkowicz, J. Kubacki, K. Balin, M. Basiaga, M. Szindler, J. Mikula, The influence of atomic layer deposition process temperature on ZnO thin film structure. *Applied Surface Science***474**, 177-186 (2019); published online EpubApr (10.1016/j.apsusc.2018.03.169).
3. N. Babitha, L. S. Priya, S. R. Christy, A. Manikandan, A. Dinesh, M. Durka, S. Arunadevi, Enhanced Antibacterial Activity and Photo-Catalytic Properties of ZnO Nanoparticles: Pedalium Murex Plant Extract-Assisted Synthesis. *Journal of Nanoscience and Nanotechnology***19**, 2888-2894 (2019); published online EpubMay (10.1166/jnn.2019.16023).
4. M. Debbichi, M. Souissi, A. Fouzri, G. Schmerber, M. Said, M. Alouani, Room temperature ferromagnetism in Cd-doped ZnO thin films through defect engineering. *Journal of Alloys and Compounds***598**, 120-125 (2014); published online EpubJun (10.1016/j.jallcom.2014.01.247).
5. M. Gandouzi, Z. R. Khan, A. S. Alshammari, Theoretical and experimental investigations of the structural and optoelectronic properties of Zn_{1-x}Cd_xO alloys. *Computational Materials Science***156**, 346-353 (2019); published online EpubJan (10.1016/j.commat.2018.09.056).
6. A. S. Dive, K. P. Gattu, N. P. Huse, D. R. Upadhyay, D. M. Phase, R. B. Sharma, Single step chemical growth of ZnMgS nanorod thin film and its DFT study. *Materials Science and Engineering: B***228**, 91-95 (2018); published online Epub2018/02/01/ (<https://doi.org/10.1016/j.mseb.2017.11.018>).
7. Q. Y. Hou, Y. Li, L. F. Qu, C. W. Zhao, The effect of Cd substitution doping on the bandgap and absorption spectrum of ZnO. *International Journal of Modern Physics B***30**, (2016); published online EpubDec (10.1142/s0217979216502155).
8. P. Palacios, I. Aguilera, P. Wahnon, Electronic structure and optical properties in ZnO:M(Co, Cd) Effect of band-gap variation. *Thin Solid Films***518**, 4568-4571 (2010); published online EpubJun (10.1016/j.tsf.2009.12.033).
9. G. M. M. Gubari, I. M. S. M., N. P. Huse, A. S. Dive, R. Sharma, Synthesis and photosensor study of as-grown CuZnO thin film by facile chemical bath deposition. *AIP Conference Proceedings***1953**, 100072 (2018)10.1063/1.5033008).
10. R. Chaurasiya, A. Dixit, Point defects induced magnetism in CdO monolayer: A theoretical study. *Journal of Magnetism and Magnetic Materials***469**, 279-288 (2019); published online EpubJan (10.1016/j.jmmm.2018.08.076).
11. A. S. Dive, N. P. Huse, K. P. Gattu, R. B. Birajdar, D. R. Upadhyay, R. Sharma, Theoretical and experimental investigations of intermediate bands in ZnS–Mg nanocrystalline thin film photosensor. *Journal of Materials Science: Materials in Electronics***28**, 15161-15167 (2017); published online Epub2017/10/01 (10.1007/s10854-017-7393-5).
12. B. U. Haq, R. Ahmed, S. Goumri-Said, Solar Energy Materials & Solar Cells. *Solar Energy Materials and Solar Cells***130**, 6-14 (2014); published online EpubNov (10.1016/j.solmat.2014.06.014).
13. B. S. Sengar, V. Garg, A. Kumar, V. Awasthi, S. Kumar, V. V. Atuchin, S. Mukherjee, Band alignment of Cd-free (Zn, Mg)O layer with Cu₂ZnSn(S,Se)₄ and its effect on the photovoltaic properties. *Optical Materials***84**, 748-756 (2018); published online EpubOct (10.1016/j.optmat.2018.08.017).



THE STUDY OF TRANSFERENCE NUMBER MEASUREMENTS OF poly(vinyl acetate)/polyindole COMPOSITE FILMS

D. J. Bhagat*

Nehru Mahavidyalaya, Nerparsopant, 445102, Maharashtra, India.

*Corresponding author: bhagatd@rediffmail.com

ABSTRACT :

In present research paper, the investigation of transference number measurements poly(vinyl acetate)/polyindole composite films are reported. The prepared composites are analyzed via DC conductivity and transference number measurements. The activation energy, electronic band gap energy and transference number measurement values are reported. The value of the ionic transference number is ranges over 98.98–99.17 %, reflects that charge transport in the composite film is mostly dominated by ions.

KEYWORDS: Poly(vinyl acetate)/polyindole; composite.

1. INTRODUCTION

The polymers are investigated in various generation such as, polymers (insulator), conducting polymers (semiconductor), copolymers, conducting polymer derivatives, conducting polymer composites, conducting polymer nanocomposites, etc. Moreover, these materials show different properties than basic polymers. The materials as well as synthesis methods could affect the properties. The new generation composite materials have enhanced electrical, optical, mechanical, physical properties as compared to basic conducting polymers. These composite materials have the potential application in various electronic devices. In recent years, polyindole got more research attraction as a conducting polymer as well as it shows the more attractive properties as compared to other. Polyindole and its composites have lots of potential application in electronic devices [1–11].

Some research were investigated the polyindole via different synthesis methods and studied its various properties. These are, Kuyuncu et al. determined the electrokinetic as well as electrorheological properties of poly(vinyl chloride)/polyindole (PVC/PIN) conducting composites [12]. Goel et al. fabricated polyindene as well as polyindole nanostructures [13]. Joshi et al. synthesized gold nano assemblies in polyindole matrix using two phase oxidative polymerization of indole using HAuCl_4 as the oxidizing agent, at the aqueous (0.5M HCl)/dichloromethane interface [14]. Zhijiang et al. investigated the characteristics of the polyindole film doped with a Li ionic salt for use as a cathode electrode [15].

The goal of the reported paper is to investigate the transference number measurements of develop poly(vinyl acetate)/polyindole composite films via chemical polymerization. Moreover, examination of the activation energy, electronic band gap energy and transference number measurements of prepared composite materials. The electronic band gap of developed composites can confirm the semiconducting nature. The determination of transference number measurements could be reflects the effect of ions and electrons on the conductivity of composite films.

2. EXPERIMENTAL

All procured and used chemicals were analytical grade (AR). Moreover, indole as monomer, ferric chloride (FeCl_3) used as oxidizing agent, methanol used as organic media (solvent) and all were purchased

from SD Fine Chemicals, India. The poly(vinyl acetate) (PVAc) used as polymer buy d from Himedia Chemicals, India.

The poly(vinyl acetate)/polyindole (PVAc/PIN) composite films were developed at room temperature by chemical oxidative polymerization method. The ferric chloride (FeCl_3) was utilized as dopant for oxidative polymerization. The detailed about the synthesis technique of poly(vinyl acetate)/polyindole (PVAc/PIN) composite films by dopant ferric chloride was reported in my previous reported paper [16].

The two probe technique as a function of temperature was used to carry out the DC conductivity measurements of the synthesized samples. The DIGIMATIC micrometer with a least count of 0.001 mm was utilized to determine the thickness of the films. As-synthesized films were coated to place electrodes on both sides with a graphite block. The DC polarization method was utilized to record transference number measurements.

3. RESULTS AND DISCUSSION

The dc conductivity results

The dc conductivity (σ_{dc}) of the poly(vinyl acetate)/polyindole (PVAc/PIN) composite films was estimated via the sample dimensions method. The highest value of dc conductivity of prepared films containing 30 wt% of oxidant calculated as 4.46×10^{-6} S/cm at 383 K. The activation energy necessary to conquer the potential barrier is estimated at 0.605 eV. The dc conductivity of composite films enhances with increase in concentration of dopant up to 30 wt%, and then decline with more increase in wt% of dopant concentration. Furthermore, the activation energy values are decline with an increase in dopant concentration up to 30 wt% and then raises with further raise in wt% of dopant is display in table 1 and also reported in previous article [17].

The dc conductivity values of PVAc/PIN composite films reflect a random nature investigated from figure and table. The least squares straight-line fitting is utilize to estimate the activation energy of all developed composite samples. The values of activation energy has been estimated via equation,

$$E_{dc} = -(\text{slope}) \cdot k_B T \quad (1)$$

Where, E_{dc} is the activation energy, T is the absolute temperature and k_B is Boltzmann's constant. The values of the dc conductivity (σ_{dc}) at temperature 308 K and 383 K, activation energy (E_{dc}) for the different wt% of the PVAc/PIN composite films are listed in table 1.

Table 1: The dc conductivity (σ_{dc}) at 308 K and 383 K, activation energy (E_{dc}).

Sample	$\sigma_{dc} \times 10^{-11}$ (S/cm) at 308 K	$\sigma_{dc} \times 10^{-6}$ (S/cm) at 383 K	Activation energy E_{dc} (eV)
10 wt%	1.01	0.602	0.624
20 wt%	4.19	1.96	0.617
30 wt%	9.93	4.46	0.605
40 wt%	1.85	0.987	0.620
50 wt%	0.576	0.38	0.625

Determination of electronic band gap

The electronic band gap of composites has been calculated through given relation [18],

$$E_g = -2.303 \times 2k_B \times (\text{slope}) \times 10^3 \quad (2)$$

Where, k_B is Boltzmann's constant, E_g is electronic band gap. The electronic band gap of samples are calculated in the range 2.78–2.87 eV. The obtained electronic band gap values reflect the semiconducting nature of PVAc/PIN composite films. The values of dc conductivity (σ_{dc}) at temperature 308 K and 383 K, electronic band gap (E_g) for different wt% of PVAc/PIN composite films are listed in table 2.

TRANSFERENCE NUMBER MEASUREMENTS

The determination of the total ionic transference number (t_{ion}) and electronic transference number (t_{ele}) contributions to the total conductivity was obtained from transference number measurements. The measurement of the transference number was performed at room temperature. A constant 5V dc potential applied across the film was used to investigate the time dependence of the current. The t_{ion} and t_{ele} numbers can be calculated from figure 1 using Equations (3) and (4). [19–24].

$$t_{ion} = \frac{I_i - I_f}{I_i} \quad (3)$$

$$t_{ele} = 100 - t_{ion} \quad (4)$$

Where, I_i is the primary value of current at starting point and I_f is final value of current on getting saturation. In the figure 1, the plot (current versus time) up to 300 seconds is presented because after it current becomes steady up to 6000 seconds that shown in inset of figure. Figure 1 shows a plot of the time dependence of the current that displays the characteristic behavior for ionic charge transport. After a certain time, the total current becomes nearly constant at a certain non-zero value. The residual current is primarily due to electrons and holes.

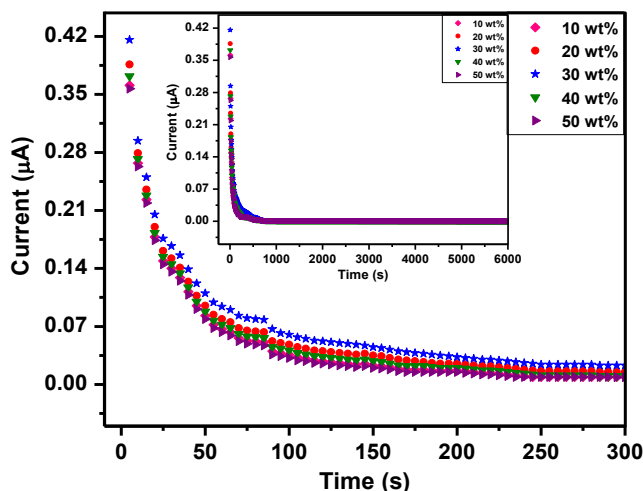


Figure 1: Plot of time dependence of current.

The value of the ionic transference number is found to be 98.98–99.17 %, implying that charge transport in the composite film is mostly dominated by ions. The values of ionic transference number measurements are given in table 2. These values reflect the domination of ionic conductivity. The values of electronic band gap (E_g) and ionic transference number (t_{ion}) for different wt% of PVAc/PIN composite films are listed in table 2.

Table 2: Electronic band gap (E_g) and ionic transference number (t_{ion}).

Sample	Electronic band gap (E_g) eV	Ionic transference number (t_{ion})
10 wt%	2.87	99.17
20 wt%	2.84	99.03
30 wt%	2.78	98.98
40 wt%	2.85	99.06
50 wt%	2.87	98.77

The estimated electronic band gap energy values represent the semiconducting nature of PVAc/PIN composite films. Moreover, the composite materials display the application potential in electronic devices from electronic band gap values.

4. CONCLUSION

The successful preparation of PVAc/PIN composite films is carried out via chemical polymerization method through the dopant ferric chloride. The electronic band gap energy is determined in the range 2.78–2.87 eV. Moreover, the activation energy values of composite films are found in the range 0.605–0.625 eV. The ionic transference number is evaluated ranges over 98.77–99.77 % that represents the domination of ionic conductivity over electronic conductivity.

ACKNOWLEDGEMENTS

Author is very much grateful to Principal, Arts Science and Commerce College, Chikhaldara for providing necessary facilities. Moreover, author is grateful to Principal, Nehru Mahavidyalaya (Arts, Commerce and Science) Nerparsopant, Yavatmal for support in research and publication.

5. REFERENCES

- 1) P. Kar, A. Choudhury, Adv. Polym. Technol. 32 (2013) 760–770.
- 2) M. T. Ramesan, J. Appl. Polym. Sci. 128 (2013) 1540–1546.
- 3) D. J. Bhagat, G. R. Dhokane, Mater. Lett. 136 (2014) 251–253.
- 4) J. Simitzis, D. Triantou, S. Soulis, J. Appl. Polym. Sci. 118 (2010) 1494–1506.
- 5) M. Yurtsever, E. Yurtsever, Polym. 43 (2002) 6019–6025.
- 6) D. J. Bhagat, G. R. Dhokane, Appl. Sur. Sci. 351 (2015) 1440–1445.
- 7) G. Nie, X. Han, J. Hou, S. Zhang, J. Electroanal. Chem. 604 (2007) 125–132.
- 8) A. Lengalova, V. Pavlinek, Q. L. Cheng, P. Saha, Int. J. Mod. Phys. B 21 (2007) 4883(1–9).
- 9) D. J. Bhagat, G. R. Dhokane, J. Inorg. Organomet. Polym. Mater. 27 (2017) 46–52.
- 10) G. Chakraborty, K. Gupta, A. K. Meikap, R. Babu, W. J. Blau, J. Appl. Phys. 109 (2011) 033707(1–9).
- 11) X. G. Li, H. Feng, M. R. Huang, G. L. Gu, M. G. Moloney, Anal. Chem. 84 (2012) 134–140.
- 12) K. Koyuncu, H. I. Unal, O. Y. Gumus, O. Erol, B. Sari, T. Ergin, Polym. Adv. Technol. (2011).
- 13) S. Goel, N. A. Mazumdar, A. Gupta, Appl. Surface Sci. 256 (2010) 4426–4433.
- 14) L. Joshi, R. Prakash, Mater. Lett. 66 (2012) 250–253.
- 15) C. Zhijiang, Y. Guang, Synth. Met. 160 (2010) 1902–1905.
- 16) D. J. Bhagat, G. R. Dhokane, J. Mater. Sci. Mater. Electron. 27(11) (2016) 11790–11797.
- 17) D. J. Bhagat, G. R. Dhokane, Electron. Mater. Lett. 11 (2015) 346–351.
- 18) D. J. Bhagat, G. R. Dhokane, AIP Conference Proc. 1728 (2016) 020171(4).
- 19) D. J. Bhagat, G. R. Dhokane, Chem. Phys. Lett. 619 (2015) 27–31.
- 20) E. Sheha, Solid State Ionics 180 (2009) 1575–1579.

- 21) S. S. Sekhon, S. Chandra, J. Mater. Sci. 34 (1999) 2899–2902.
- 22) M. Jaipal Reddy, C.H. Ramesh, J. Siva Kumar, U.V. Subba Rao, Int. J. Appl. Eng. Res. Dindigul. 2 (2011) 147–156.
- 23) A. F. Naomi, G. R. Kevin, D. R. Sadoway, Electrochim. Acta 46 (2001) 3351–3358.
- 24) S. S. Das, V. Srivastava, P. Singh, Indian J. Eng. Mater. Sci. 13 (2006) 455–461.



EVALUATION OF ANTIBACTERIAL ACTIVITY OF SOME TRADITIONALLY USED MEDICINAL PLANTS (AEGLE MARMELLOS, POMEGRANATE, BRYOPHYLLUM PINNATUM) AGAINST E. COLI.

Nivrutti W. Bagalkar* , Jayshree R Netkar* and Ankita R. Tathod
Department of Microbiology J.D.P.S. College Daryapur

ABSTRACT :

A present study was conducted to identify and characterize the E. Coli from contaminated water and check its antibiotic activity against Aegle Marmelos, Pomegranate, Bryophyllum pinnatum & the Mixture of (Aegle Marmelos, Pomegranate, Bryophyllum pinnatum leaves) from these plants. The leaves of these plants are collected and dried and crushed. Then prepared fine powder and applied for Whatman filter paper and observe the zone of inhibition against E. coli. The maximum growth of inhibition was seen under the pomegranate & mixture of (Aegle Marmelos, Pomegranate, Bryophyllum pinnatum).

INTRODUCTION

Multiple drug resistance in human pathogenic microorganisms has been developed due to indiscriminate use of commercial antimicrobial drugs commonly used in the treatment of infectious diseases, so for that plants provide a wealth of antimicrobial agents which can be used as an alternate source of antibiotics. Plants are used for the medicinal source natural products maintaining the human health. Plants are prospective source of antimicrobial agents in different countries^[1].

Antibiotics resistance become serious and wide spreads problem developing countries both in hospitals and commonly can use in each other. Scientific investigations of medicinal plants have been initiated in many countries because of their contributions to health care. The primary benefits of using plant-derived medicines are relatively safer than synthetic alternatives, offering profound therapeutic benefits and more affordable treatment^[2].

Plants produce a wide variety of secondary metabolites which are used either directly as precursors or as lead compounds in the pharmaceutical industry. It is expected that plant extracts showing target sites other than those used by antibiotics will be active against drug resistant microbial pathogens. However, very little information is available on such activity of medicinal plants and out of the 4,00,000 plant species on earth, only a small number has been systematically investigated for their antimicrobial activities^[3]. Gram negative bacterium such as *Escherichia coli* is present in human intestine and causes lower urinary tract infection, cystitis or septicaemia^[4].

In the present study use for the various type of medicinal plants. That have the potential to be used as antimicrobial agent against E. coli, to conduct antimicrobial activity assays against E. coli isolated from turbid water. The three plant mixture of (Aegle Marmelos, Pomegranate, Bryophyllum pinnatum leaves).

MATERIAL AND METHODS

Collection of bacteria we accrued bacteria from the contaminated water in the sterilized the container the inoculate on prepared nutrients agar plate for isolation after which we isolated the microorganisms. Then this microorganisms inoculated in MacConkey agar and incubate at 37°C for 24-48 hours after which we isolated the pure microorganisms.

Bacterial colony identification and external morphology study

The use of spread plate method the bacterial colony identified and external morphology becomes studied for nutrient agar media used. Consequently 100 ml of nutrient agar media was prepared for the four petri plate the nutrient agar media become autoclaved and then poured in four petri dishes which have been sterilized in auto claved. Then these serial dilution of $10^2, 10^4$, and 10^6 were selected and from that 0.1 ml of way of life turned into transferred from each serially diluted test tubes and spread at the petri plates. Then the petri dishes were stored within the incubator for 37°C for 24 hours for the incubation and boom of microorganisms. After 24 hrs. Of petri dishes were taken out Sub quant bacterial outside morphology have been studied.

Pure Culture Isolation of Bacteria

The well developed and selected colonies were recognized on the MacConkey agar plate have been marked after which those spread colonies have been chosen and though the inoculating need leand streaked separate lying the test tube having the nutrient agar slant for the growth of single colonies of bacterial culture of microorganisms. Take a test tube had been marked after the starting of those colonies from the petri plates have been left inside the incubator at 37°C for 24 hrs overnight for growth and incubation. After the incubation the pure culture single day special species of bacterial culture Slants evolved in take a test tube have been in addition picked and purified.

Microscopic Study

The pure culture of colonies that received in test tubes was put for the gram staining for the identification of colonies. The gram staining accomplished in laminar air flow. The slide is taken for the slide rack. The slide has been washed with ethanol. The inoculating needle loop full starting had been picked from each take a look at tube and made a smear on the slide then the taken in the staining room for three staining smear. The smear stain are following steps a) rest applied for the Crystal violet on each slide for the 30 sec. b) Distilled water wash. C) Iodine as a slide is used for the mordant for a 1min. Then 95% of alcohol washes and then washes distilled water. d) Safranin become applied on the slide and wash with distilled water. For (then the slide are dried. The entire gram staining techniques was done following the Christian gram technique ^[5].

Identification of bacterial isolates through biochemical test

The isolated from the contaminated water turned into recognize up to preliminary bases on morphological structures and biochemical tests as laid out Bergey's guide determinative Bacteriology ^[6] the biochemical tests are become finished with the aid of ^[7]. Which protected like gram staining, IMViC reaction catalase test, dehydrogenase test, citrate utilization test, oxidation fermentation test, nitrate reduction, gelatin hydrolysis test, urea hydrolysis test, Indole production test, triple sugar iron (TSI) carbohydrates fermentation test. For isolated bacterial identification as per Bergey's manual we performed test IMViC test show in Methyl red, voges-Proskauer (VP) and citrate. Then Gelatinase, catalase, nitrate, oxidase, H_2S ...

Collection of plants

The three medicinal plants in this study are shown in the table below. These are easily available in the environment. We collected the fresh plants leaves Bel, Patra, Pomegranate.

Sr.no	LocalName	Scientific name
1	Bel	Aegle Marmelos
2	Patra	Bryophyllum pinnatum
3	Pomegranate	Punica Granatum

TABLE 1: SELECTED PLANTS

Preparation of fine powder

Wet area three medicinal plants leaves Bel, Pomegranate, part of this leaves washed with distilled water to remove the unwanted material and air dried and dry the under sunlight the temperature of daylight is 42-43°C for 48 hrs after we scrub and grind this leaves. The new discovered the fine powder. Then the sterilized airoven and store in sterile container.

Preparation of sterile disk

Whatman's filter out paper became punched into 5mm disc from and they sterilized each sterile disc. Precaution has been taken to prevent the flow of the powder extract from the discs to the outer surface. The amassed powder extracts had been carried out in small quantities on disc.

Assay of antimicrobial activity using agar disc diffusion method

The sensitivity of different bacterial strains to the aqueous plant extracts was measured using a standard agar diffusion assay [8]. The 30 ml of nutrient agar became poured in to sterile petriplate, after solidification 100 µl of fresh culture of *E.coli* had been poured on the respective plates. After some time culture turned into discard from agar plate. Then take sterilized forceps and follow the disk carefully in center of agar plate. The plates had been incubated for 24-48 hour at 37°C. After incubation the diameter of inhibitory zone shaped around each discs were measured in cm and recorded.

RESULT AND DISCUSSION

The aim of the present study was first upon collection of *E.Coli* and compares the antimicrobial activity of Bel, Pomegranate, patra leaves. On the basis of cultural character, Morphological character (colony color, shape and size) and biochemical character isolated bacteria was identifying. Following character was compare with 'BERGEY'S. Isolated bacterial result was given in following tables.

Sr.No.	TABLE 2: MICROSCOPIC CHARACTER	RESULT
1)	Gram	Negative (-ve)
2)	Spore	Non- spore forming
3)	Motility	Motile

Sr.No.	Test	Result
1)	Indol	Positive (+ve)
2)	Methyl Red	Positive (+ve)
3)	Voges-proskauer (VP)	Negative (-ve)
4)	Citrate	Negative (-ve)
5)	Gelatinase	Negative(-ve)
6)	Nitrate	Positive(+ve)
7)	Catalase	Positive(+ve)
8)	Oxidase	Negative(-ve)
9)	H ₂ S	Negative(-ve)
10)	Glucose	Positive(+ve)
11)	Lactose	Positive(+ve)
12)	Sucrose	Positive (+ve)
13)	Galactose	Positive(+ve)

Table no. 3: Biochemical test

After analyzing the colony morphology on cultureing medium, colony morphology checked into in addition studied on the selective media. When the secondary identification on selective media, all samples was tested microscopically right here the shape size and motility checked and also the gram staining technique is followed. When observe on top of check currently we tend to conformed isolated bacterium culture was *E.Coli*.

Measurement of Antimicrobial Activity using Agar Well Diffusion Method

In present study selected medicin aplants that are Bel ,Pomegranate, patra had plants leaves are collected to test in antimicrobial activity at *E. Coli* from contaminated water sample by "Agar diffusion technique" And the Diameter area if inhibition become measured in mm. Antimicrobial activity of selected plants of *E. Coli*s given table no 4. Maximum zone of inhibition pomegranate plants leaves against *E. coli* (0.9 mm) and the lowest zone of inhibition is bel (0.2 mm) and average zone of inhibition in against patra (0.3 mm) and the zone of mixture is (0.7 mm). Various researchers have worked in exploring the antimicrobial potency of leaf extract against infectious bacteria^[9]. One of the effort that Bel, pomegranate, patra plants exhibition the antimicrobial activity against isolated *E. Coli* strain. Which suggested the clinically useful?

Sr.No	Medicinal plant	Zone Of inhibition
1)	Bel	0.2
2)	Pomegranate	0.9
3)	Patra	0.3
4)	Mixture of plant	0.7

Table no. 4: zone of inhibition

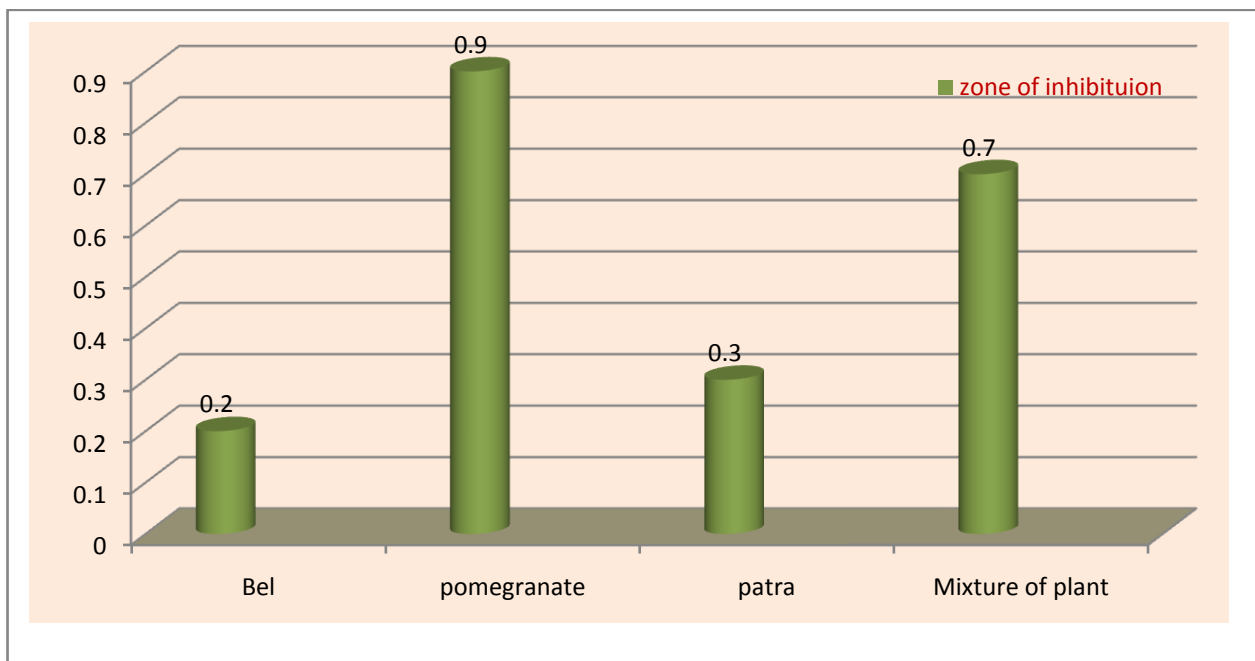


Fig.1: Graph of zone of inhibition against *E.Coli*

The present study was conducted to obtain preliminary information on the antimicrobial activity of three traditional medicinal plants of India. Plant extracts are potential sources of novel antimicrobial compounds especially against bacterial pathogens. Through this in vitro study, we could see that three plant extracts inhibited the growth of clinical isolates of *E. coli* but their effectiveness varied.

Over the past few decades, a number of publications have been reported on the antibacterial activities of extracts from medicinal plants^[10].

Pomegranate peel is used to treat infections present in human sexual organs as well as mastitis, acne, folliculitis, pile, allergic dermatitis, tympanitis, scalds, diarrhea, dysentery and as an antioxidant^[11]. The results obtained from the present study provide evidence that Bel, Pomegranate, patra plant exhibit antibacterial activities against isolated *E. Coli* strain, which suggests that they may be clinically useful. Out of this plant pomegranate plant show more zone of inhibition as compared to other plant.

CONCLUSION

The current study has identified *E. coli* bacteria from turbid water and checks its antimicrobial activity against Aegle Marmelos, Pomegranate, Bryophyllum pinnatum. It was investigated that pomegranate plant showed maximum zone of inhibition against *E. coli*. Hence here we concluded that for controlling *E. coli* infection use Pomegranate leaves.

ACKNOWLEDGEMENT

The authors are sincerely thankful to principal of J.D.P.S. College Daryapur for providing lab, the authors are also thankful to all my Classmates for his moral support and suggestions in the preparation of the paper. The authors are grateful to the Editor-in-Chief for their encouragement and support.

REFERENCE

- ¹ Alviano DS, Alviano CS *Curr Pharm Biotechnol.* 2009 Jan; 10(1):106-21.
- ² Ahmed. I. and A.Z. Beg. (2001). *J Ethopharmacol.* 74 : 113 – 12.
- ³ Anjana. S., R. Verma and P. Ramteke. (2009). *W. App. Sci. J.* 7(3) : 332 – 339.
- ⁴ Benhassaini. H and enabderrahmane. K and Chi. K (2003). Contribution to the assessment of the antiseptic activity of essential oils and oleoresin of Pistacia tial Atlas on some microbial sources: *Candida albicans* (ATC 20027), *Candida albicans* (ATCC 20032) and *Saccharomyces cerevisiae*: *ethnopharmacology*, February (30): 38-46.
- ⁵ Collee, J.G., Miles, R.S. and Watt, B. 1996. Test for the identification of bacteria. In: Collee, J.G., Faser, A.G., Marmion, B.P., Simmons, A. (Eds). Mackie and McCartney practical medical microbiology, 14th edn. Churchill Livingstone, London. Pp. 13 -145.
- ⁶ Gilman J.C. second ed. Oxford and IBH Publishing Company; New Delhi, India: 1957. A Manual of Soil Fungi.
- ⁷ Holt JG, Krieg NR, Sneath PHA, Staley JT. and Williams ST. 1994. *Bergey's Manual of Determinative Bacteriology*, 9th ed. Williams and Wilkins, Baltimore, Maryland.
- ⁸ Bauer AW, Kirby WMM, Sherris JC, Turck M: Antibiotic susceptibility testing by a standardized single disk method. *American Journal of Clinical Pathology.* 1996, 45: 493-496.
- ⁹ Suree N and Pana L. (2005) *Sci. Tech. J.* 5(3): 527-538.
- ¹⁰ Fankam AG, Kuate JR, Kuete V. Antibacterial activities of *Beilschmiedia obscura* and six other Cameroonian medicinal plants against multi-drug resistant Gram-negative phenotypes. *BMC Complement Altern Med* 2014; 14(241):1472-6882.
- ¹¹ Singh, R. P., Chidambara, M. K. N. and Jayaprakasha, G. K. (2002). Studies on the antioxidant activity of pomegranate (*Punicagranatum*) peel and seed extracts using invitro models. *Journal of Agricultural and Food Chemistry*, vol. 50, no. 1, :81–86, 32.